Heinz-Georg Flesch

Interface Controlled Microstructure and Morphology of Thin Layers for Organic Electronics

DOCTORAL THESIS

For obtaining the academic degree of
Doktor der technischen Wissenschaften

Doctoral Programme of Technical Sciences
Technical Physics

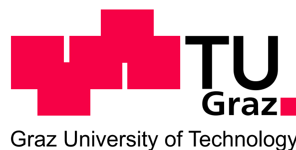

Graz University of Technology

Supervisor:

Ao. Univ.-Prof. Dipl.-Ing. Dr.techn. Roland Resel

Institute of Solid State Physics

Graz, September 2010

Deutsche Fassung:
Beschluss der Curricula-Kommission für Bachelor-, Master- und Diplomstudien vom 10.11.2008
Genehmigung des Senates am 1.12.2008

EIDESSTATTLICHE ERKLÄRUNG

Ich erkläre an Eides statt, dass ich die vorliegende Arbeit selbstständig verfasst, andere als die angegebenen Quellen/Hilfsmittel nicht benutzt, und die den benutzten Quellen wörtlich und inhaltlich entnommene Stellen als solche kenntlich gemacht habe.

Graz, am …………………………… ………………………………………………..
(Unterschrift)

Englische Fassung:

STATUTORY DECLARATION

I declare that I have authored this thesis independently, that I have not used other than the declared sources / resources, and that I have explicitly marked all material which has been quoted either literally or by content from the used sources.

…………………………… ………………………………………………..
date (signature)

to Julie

Acknowledgment

This work is the result of many fruitful cooperations within the network of my supervisor Roland Resel. I want to thank him for guiding my work and opening me the opportunity to visit numerous conferences and scientific events, encouraging me to launch scientific projects and finding the positive aspects in every measurement!

Within the Institute of Solid State Physics there are some special people - living their lives partially in momentum space. I want to thank them for our discussions and supporting ideas to figure out how k-space can be transformed to real space for people thinking without Fourier Transform. Over the time these people have been Tatjana Djuric, Thomas Haber, KArl RudOLF Marguc, Markus Koini, Armin Moser, Alfred Neuhold, Jiri Novak, Bernhard Wedl, and Oliver Werzer.

From the Institute of Solid State Physics I want to acknowledge Egbert Zojer and his group, especially Simon Ausserlechner, Andrej Golubkov, Marco Marchl and Peter Pacher for discussions and cooperations. Adolf Winkler offered me the possibility to learn about atomic force microscopy. In general the Institute and the people there offered me the possibility to work in a friendly and scientifically encouraging environment - providing me always with enough samples. I thank especially Birgit Kunert and Harald Kerschbaumer for being always busy in the background.

I want to acknowledge the people of the NMP Weiz, especially Georg Jakopic who introduced me to the miracles of ellipsometry.

From Bratislava I want to thank the people around J. Kovac for for the excellent cooperation.

Chris McNeill introduced me to the field of all polymer solar cells and is acknowledged for that.
Most of my time I spent on self-assembled monolayers which have been provided by the people around Dago deLeeuw. I want to thank him for cooperation and his co-workers as there are Simon G. J. Mathijssen, Edsger C. P. Smits, Fatemeh Gholamrezaie, Sergei A. Ponomarenko, and Harry J. Wondergem (always providing an alternative view on things in k-space!). The people from Leoben as there are Gregor Hlawacek, Quan Shen, Christian Teichert, Peter Puschnig, and Claudia Ambrosch-Draxl are acknowledged for their cooperation on these SAMs.
Thanks to Oleg Konovalov for fruitful discussions at the ESRF in Grenoble and to Federico Zontone and Jiri Novak for support during the beamtimes at ID10b. Further thanks go to Ulrich Pietsch and his group in Siegen for discussions and joint experiments at the synchrotron.
For funding I want to acknowledge the Austrian Research Promotion Agency within the research project ISOTEC.
For passing hard times of little progress you need some motivating voice in your mind: *When the Going Gets Tough, the Tough Gets Going.* This motivation works only when your friends and family give you the support you need during these tough times. I want to thank these friends, my family and all those not yet mentioned for their support and bearing my moods.
I want to thank Julia for supporting me mentally through the time of my studies.

Preface

This PhD-thesis covers large parts of my work done since spring 2007 at the Institute of Solid State Physics at the Graz University of Technology. My work has been focused on the characterization of thin films for organic electronics mainly by means of x-rays but also by ellipsometry and atomic force microscopy.
The beginning of the thesis is dedicated to a short introduction into self-assembled monolayers in general (chapter 2) which is followed by a chapter on a special crystalline self-assembled monolayer system based on quinquethiophene (chapter 3). The following part is dedicated to self-assembling thin films and layer thickness of these layers (chapter 4).
Parts of my work have already been published in scientific journals. Dealing with thin parylene-C layers (chapter 5) and an all polymer solar cell aproach based on thiophenes (chapter 6). These parts are reproduced in this thesis as already published. Some additional basic information on ellipsometry is given in chapter 5.
Issues and selected additional information on the quinquethiophene based self-assembled monolayer are given in the Appendix.

Abstract

This work is focused on the characterization of thin films on isotropic surfaces for organic electronics. It summarizes the use of various x-ray scattering techniques (ex-situ and in-situ temperature dependent determination of structure and morphology) but also complementary techniques like spectroscopic ellipsometry and atomic force microscopy for thin film characterization. The main part is dedicated to self-assembled monolayers based on quinquethiophene. Experimental and theoretical investigations on the 2-dimensional crystal structure and morphology as well as on the phase behavior under the influence of temperature are presented. The layers are heated up to the breakdown of the crystallographic order and further to the complete desorption of the molecules from the substrate. Another part of the work covers the attempt of controlling the layer thickness of a solution processed self-assembling thin film built of a 7:3 ratio mixture of TSC and its sulfonic acid counterpart TSA is discussed. Layer thickness and the roughness of the surface are controlled by the amount of water added to the solution during layer formation. The issues of reproducibility are addressed in that context. The combinational approach of spectroscopic ellipsometry and x-ray reflectivity in case of parylene-C layers uses the x-ray results as input for ellipsometry. The two very similar techniques - both not straight forward in their data evaluation - provide enhanced information on thin films if properly and carefully combined. In the thin film regime the dependence of the refractive index on the layer thickness is determined. The crystallization of a polymer mixture of the thiophene based materials P3HT and F8TBT due to temperature treatment in an all polymer solar

cell device has been followed in-situ. Crystallite size of P3HT and the amorphous F8TBT are evaluated in context of the electrical characterization. This leads to the insight of an optimal annealing temperature and crystallite size for largest efficiency - the main issue in solar cell development.

Kurzfassung

Im Rahmen dieser Dissertation wurden dünne Schichten auf isotropen Substraten, die Anwendung in der organischen Elektronik finden, charakterisiert. Der Fokus liegt im Bereich unterschiedlicher Röntgentechniken (in-situ und ex-situ Charakterisierung der Morphologie und Struktur der Schichten in Abhängigkeit von Temperatur). Diese wurden mit komplementären Methoden, wie zum Beispiel spektroskopischer Ellipsometrie und Rasterkraftmikroskopie, ergänzt. Der Hauptteil der Arbeit widmet sich experimentellen und theoretischen Untersuchungen an so genannten selbstorganisierenden Monoschichten. Die untersuchten Monolagen auf Basis von Quinquethiophen sind das erste solche System auf Siliziumoxid, welches wohlgeordnete 2-dimensionale Kristalle ausbildet. Die Untersuchung der Kristallstruktur und Morphologie sowie das Phasenverhalten dieser Monolagen unter Einwirkung von Temperatur (über das Aufbrechen der Kristallstruktur bis hin zur Desorption der Moleküle vom Substrat) werden in dieser Arbeit abgehandelt. In einem weiteren Teil der Arbeit wurde ein System von selbstorganisierenden dünnen Filmen untersucht, welches in organischen Dünnfilmtransistoren zum Einsatz kommen soll. Die funktionalisierten Moleküle TSC und die entsprechende Säure TSA wurden im Verhältnis 7:3 in trockenem Toluol gelöst. Über den Wassergehalt in der Lösung können Schichtdicke und Rauheit der Filme kontrolliert werden. Insbesondere die Schwierigkeiten der Reproduzierbarkeit solcher dünnen Schichten werden diskutiert. Die Kombination von spektroskopischer Ellipsometrie mit Röntgenreflektivität wurde an dünnen Schichten von Parylene-C angewendet und zeigt auf, welche Vorteile die gemeinsame Anwendung zweier sehr ähnlicher

experimenteller Techniken mit sich bringt. Die Korrelation zwischen Schichtdicke und optischen Konstanten bei sehr dünnen Schichten kann dadurch geklärt werden. Die Vermischung der beiden auf Thiophenen basierenden Polymeren P3HT und F8TBT wurde unter dem Einfluss von Temperatur untersucht. P3HT zeigt variable kristalline Anteile, F8TBT ist vollständig amorph. Die Korrelation zwischen Kristallitgröße und elektrischen Eigenschaften unter dem Einfluss der Temperatur wurde an diesem für Polymer-Solarzellen optimierten System untersucht.

Contents

1. Motivation **1**

2. Self-assembled monolayers **3**

2.1. Frequent systems 4
2.2. Layer formation in solution 5
2.3. SAMs as surface modification 10
2.3.1. Homogeneously spaced chemical properties 11
2.3.2. Patterned SAMs 11

3. Structure of a Quinquethiophene SAM **13**

3.1. Motivation 13
3.2. Molecular design - Layer formation 16
3.3. X-ray investigations 20
3.3.1. X-ray reflectivity 21
3.3.2. Grazing incidence x-ray diffraction 23
3.4. The 2D crystal structure parameters 26
3.4.1. The unit cell 26
3.4.2. The packing of the molecules - density functional theory . . 33
3.5. Temperature annealing 36
3.5.1. Structure 39
3.5.2. Layer thickness 43

3.6. Crystal domains 46
3.6.1. Transverse shear microscopy - basic principles 46
3.6.2. TSM on 5T-SAMs 47
3.7. Conclusions on Quinquethiophene SAMs 50

4. Surface modification by inter-layers 53
4.1. The material 53
4.2. Layer thickness and morphology 55

5. A combined x-ray, ellipsometry and atomic force microscopy study on thin parylene-C films 61
5.1. Introduction 61
5.2. Experimental Methods 64
5.2.1. Sample preparation 64
5.2.2. Specular x-ray reflectivity 64
5.2.3. Ellipsometry 65
5.2.4. Atomic force microscopy 66
5.3. Results and Discussion 66
5.3.1. Film thickness variation 66
5.3.2. Precise film thickness 67
5.3.3. Optical constants 69
5.3.4. Surface roughness 69
5.4. Conclusions 72
5.5. Material 73
5.6. Spectroscopic Ellipsometry 75
5.6.1. Polarized light 75
5.6.2. Experimental setup 77
5.6.3. Data evaluation - Constructing the most physical model . . 81
5.6.4. Roughness 83

6. Charge transport properties and microstructure of polythiophene / polyfluorene blends 85
6.1. Introduction 85
6.2. Materials and methods 89
6.2.1. Materials, sample preparation and device fabrication 89
6.2.2. Time-of-flight details 90
6.2.3. x-ray diffraction details 90
6.3. Results 91
6.3.1. Time-of-flight measurements 91
6.3.2. x-ray diffraction results 94
6.4. Discussion 96
6.5. Conclusions 102
6.6. Acknowledgements 102
6.7. supplementary information 103

A. Supplementary investigations on quinquethiophene self-assembled monolayers 107
A.1. Passivated molecules 107
A.2. Stability of self-assembled monolayers 112
A.2.1. Long term stability of a 5T-SAM 112
A.2.2. Degradation of a 5T-SAM under the x-ray beam 112
A.3. Intensive AFM and TSM investigations 114
A.3.1. A submonolayer 116
A.3.2. A closed monolayer 117

B. Curriculum vitæ 123

C. Scientific activities 127
C.1. Publications 127
C.2. Talks 129

1. Motivation

Organic electronics have attracted much attention in the last decade which has also been credited by the Nobel society which awarded the Nobel prize for chemistry in 2000 jointly to Alan J. Heeger, Alan G. MacDiarmid, and Hideki Shirakawa. It is their work on iodine doped polyacetylene[1] from the 1970s that is fundamental for the development of the field of conductive polymers and hence organic electronics. Organic electronics has grown into an interdisciplinary field for physicists, chemists, device and display engineers, and material scientists.
It is not the challenge in the field of organic electronics to compete with the electronic charge transport mobility and device performance of the silicon industry. Organic electronics is looking for applications that cannot be covered by silicon based technology. For example transparent photovoltaic cells that can be printed on glass windows, the printing of integrated circuits to flexible substrates or applications like the recently announced e-book reader from Plastic Logic. For silicon the target is downsizing of structures; organic electronics somehow heads for large scales rather than miniaturization: Printing electronic circuits, light emitting devices or solar cells to large panels. Doing large scale production using low cost technology. Currently there is progress in going to the market with organic electronics technology but still a lot of work is happening on a more fundamental level. Purification of the organic materials and defined doping is a big issue in the field. Since the materials are synthesized in many steps it is crucial to purify the final

[1] H. Shirakawa, E.J. Louis, A.G. MacDiarmid, C.K. Chiang, A.J. Heeger, Synthesis of electrically conducting organic polymers: halogen derivatives of polyacetylene, (CH)x, J. Chem. Soc., Chem. Commun. (1977) 578-580.

product, the pi-conjugated material. The synthesis of new conjugated polymers and oligomers has developed into a playground for organic chemists on the search for enhanced intrinsic material properties.
The route from the purified molecule to the working device has to be taken via numerous parameters. Structural parameters of the material have to be known as for example the crystallographic order or interface as well as surface roughness of layers, which are subject of this work. The interface controls to a large extend the performance of a organic thin film device. The optimization of a system can be achieved in post-layer formation processes like temperature annealing. The influence of temperature on crystallite size, layer thickness, roughness and crystalline order can be compared to device parameters recorded temperature dependent. X-ray techniques offer the possibility to investigate systems from the submonolayer state to layers of a few micrometer, amorphous as well as crystalline, hetero-structured or from a single material. Hence this work spans the range from submonolayers of crystalline molecules to a blend morphology of amorphous and crystalline polymers of a approximately $200 \mu m$ thickness.

2. Self-assembled monolayers

The phrase *self-assembled monolayer* (SAM) covers the process of layer formation from two crucial aspects. First the self assembly, which is favorable in order to achieve highly reproducible films and second the monolayer which has very defined structural and electronic properties. In literature [1, 2, 3] self-assembly is given as follows: *Self-assembly, in a general sense, might be defined as the spontaneous formation of complex hierarchical structures from pre-designed building blocks, typically involving multiple energy scales and multiple degrees of freedom*[1]. The advantages of SAMs are:

* simple preparation from predefined building blocks
* reproducibility once the system is investigated and known
* tuning of layer properties by the variation of the building block
* more complex structures using the SAMs as building blocks
* possibilities using lateral nanometer regime structures
* ...

[1] F. Schreiber, Structure and growth of self-assembling monolayers, Progress in Surface Science. 65 151-257.

2.1. Frequent systems

Most SAMs are processed in solution but also the SAM formation from the vapor phase [4, 5] is possible. The chemical system of a SAM consists of one reactive end which has a high affinity to the substrate, some backbone unit and an endgroup where some function may be added. There are several fundamental issues concerning SAMs. What is the structure, is the SAM short or long range ordered, what is the driving mechanism for the self-assembly, what are the effects of temperature, what are the conditions for the formation of the layers,... These questions can only be answered step by step and the community is working intensively on assembling the puzzle. This chapter gives a small overview on possible systems and and basic concepts of self-assembly and monolayer formation by self-assembly in solution.
There has been a focus in research on two major systems of SAMs:

* thiols on $Au(111)$ [6, 7]
* silane-based systems on SiO_2 [8, 9, 10]

Thiol monolayers on gold surfaces have become a model system of a self-assembled monolayer due to the rather easy preparation of the substrate. Gold surfaces can easily be cleaned and are inert under ambient conditions. Furthermore there is no need to use single crystals because thin films of evaporated gold usually grow with the low energy (111)-plane. The thiol-monolayers form superlattices on the crystal surface and can be specified using their superstructure, 2D unit cell, molecular tilt, and thiol chain length. Additionally there may be added some sulfur or fluorine or any other element or functional group in order to tune the layer properties and function [11, 12, 13].
This and the following chapter are focusing on silane-based monolayer systems on SiO_2 [10, 14]. The crucial point for the substrate is the presence of OH-groups which can react with the anchoring groups of the molecule forming the SAM. This must not necessarily be SiO_2, it has been shown that also a photoresist

SU-8 [15] can provide the proper surface for the formation of silane-based SAMs. The most commonly used category is alkyltrichlorosilane where probably octadecyltrichlorosilane (OTS) [8, 16] is the most famous molecule. There is however always the possibility of 3D agglomeration and uncontrolled growth of the layer if there are three reactive anchoring sites like for trichlorosilane-based systems. A docking section consisting of a single reactive end *i. e.* a monosilane anchoring group avoids this problem.

The different chemistry of binding makes the latter class more sensitive to temperature, ph, and water content in the solution during the self-assembly [1]. One main difference to the thiol system is the lack of long range order - crystalline structure is usually missing. The molecules however are strongly bond to the substrate.

In the next chapter an outstanding development - a system presenting nicely crystalline monolayers based on a monochlorosilyl docking group will be introduced [17, 18]. This crystalline order is the exception to the rule. The advantage of the strong covalent substrate to layer binding is a robustness to temperature treatment. The crucial point of water content in the solution will be figured out in a later chapter of this work on a trichlorosilane-based system which shows all drawbacks of three anchoring sites and the issues of 3D - agglomeration.

2.2. Layer formation in solution

In a simple scheme the formation or fabrication of a SAM from solution consists of four basic steps as shown in figure 2.1. First the molecules have to be dissolved in the appropriate solvent. Appropriate in that case stands for solubility of the molecule in the solvent and providing an atmosphere for the anchoring groups to become or stay active for a certain period. Then the substrate has to be submerged into the solution. Before, there may be several steps of processing to make the substrate reactive or clean but this may vary with the type of anchoring group attached to the molecule. In the case of silane groups this may include O_2-plasma

etching to provide OH-groups [19]. Then the next point is time! The layer has to form in the solution and this may take several minutes up to days - again strongly depending on the reactivity of the anchoring group and substrate. Additional treatment from outside (heating, solvent flow, etc....) may be applied but is not necessary in general. The final step is simply picking the substrate from the solvent. This may be done in some special atmosphere (nitrogen or argon glovebox) and be followed by other steps like temperature annealing, rinsing with a solvent, drying with a stream of gas, etc,... Again this procedure depends strongly on the specific system. The individual parameters for each specific system have to be optimized, no general rule can be applied.

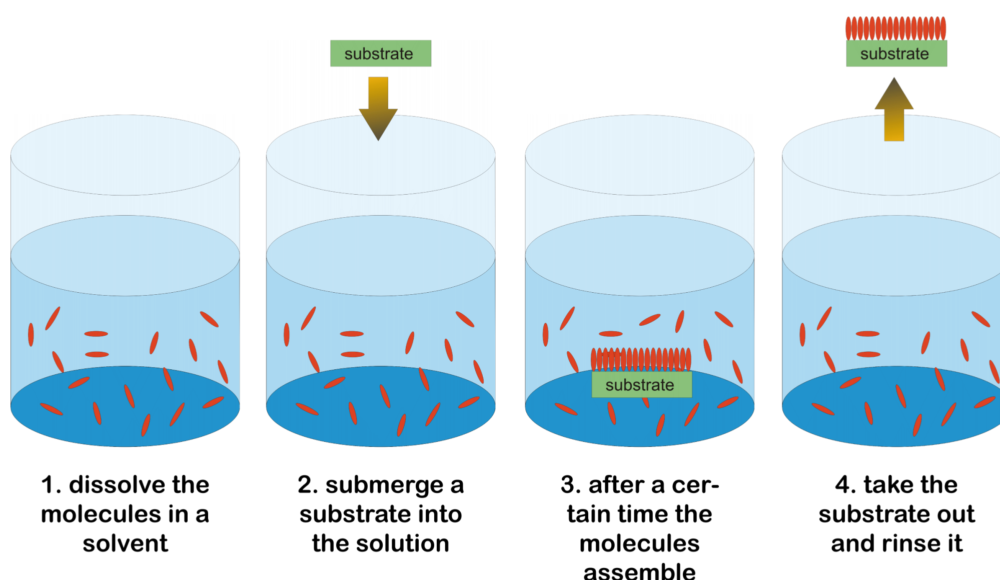

Figure 2.1.: Scheme of solution processing of a self assembled monolayer.

It is of fundamental interest to understand the part of the self-assembly process where actually the monolayer is formed. The main issues in this field are [1, 10]:

* What are the driving forces for self-assembly?
* What defines the kinetics during the layer formation?

* Does the substrate - molecule interaction define the kinetics of the layer formation?
* Does the molecule - molecule interaction define the kinetics of the layer formation?
* Does the monolayer grow homogeneously or island like?
* Is the ordering driven by the anchoring chemistry or by the chain properties?
* What degree of flexibility is necessary within the molecule?
* Is the growth driven by the collective of molecules or by single molecules?
* Does the process stop after full monolayer coverage?
* How can the layer formation be controlled externally?

As already mentioned most SAMs are grown from solution. The growth from the gas phase however is favorable in a sense of experimental control and characterization [1, 10]. Environmental properties are under better control when using vacuum chambers to produce SAMs from the gas phase. Additionally the in-situ investigation methods in vacuum systems are numerous as there are STM[2], AFM[3], LEED[4], GIXD[5], etc. for structural investigations and TDS[6] for thermal stability and investigations on kinetics.
The preparation from solution is claimed to be the technique that is less fundamental but more technology driven because of the ease of preparation. Less sophisticated equipment is needed for solution processing. Investigations on solution grown monolayers can be done after growth when transferring them to a

[2]scanning tunneling microscopy
[3]atomic force microscopy
[4]low energy electron spectroscopy
[5]grazing incidence x-ray diffraction
[6]thermal desorption spectroscopy

vacuum systems; but the growth and growth kinetics are hardly accessible for solution processes. They can be investigated using submonolayer films. The problem in investigating submonolayer films is that for ex-situ measurements the submonolayer can behave quite different to the full monolayer. The rinsing procedure or even taking the substrate out of the solution may cause a drying out of the layer and hence lead to a change in the structure of the submonolayer that is actually investigated ex-situ compared to the full monolayer or the submonolayer actually growing in the solution. Therefore it is important to improve the in-situ investigation techniques to make properties like submonolayer structure and thickness as well as kinetics tangible.
The external control parameters are first of all the temperature for both types of preparation and second the concentration of molecules in the solution or the partial pressure in case of vapor preparation technique. The second one can in general be called impinging rate, valid for both techniques.
Several studies on OTS layers show that the water content in the solution defines the growth kinetics and final result of the layer formation [20]. Under dry conditions (where the only water stems from a thin aqueous layer on the substrate surface) the growth takes much longer but the final result is an extremely smooth monolayer. If the solution contains water itself the OTS aggregates already in the solution and the layers grow fast - with the drawback of large surface roughness or 3D-agglomeration. Hence kinetics can be driven by the water content in the solvent and solution, respectively. It is this water content that is difficult to control and makes comparison between different experiments difficult.
OTS has been found to be an interesting model system anyway. Depending on the growth conditions three types of growth are reported in literature [21, 22, 23, 24, 25, 26]:

* Island like growth at low temperature.

* Homogeneous growth at high temperature.

* Mixture of both types at intermediate temperatures.

There is even a reversible transition from one state to the other reported for submonolayers of OTS by temperature treatment [27].
Island like growth means that the layer forms in islands which consist already of well ordered molecules whereas homogeneous growth is the formation of a laterally unordered layer that starts to order with higher coverage and time. Both types of growth are illustrated in figure 2.2. The scheme illustrates that once a full coverage of the substrate is reached both types are difficult to distinguish but in the submonolayer the investigations should be done in-situ. Ex-situ a dried film of island-like type might look like a layer of homogeneous growth, vice versa it is unlikely.

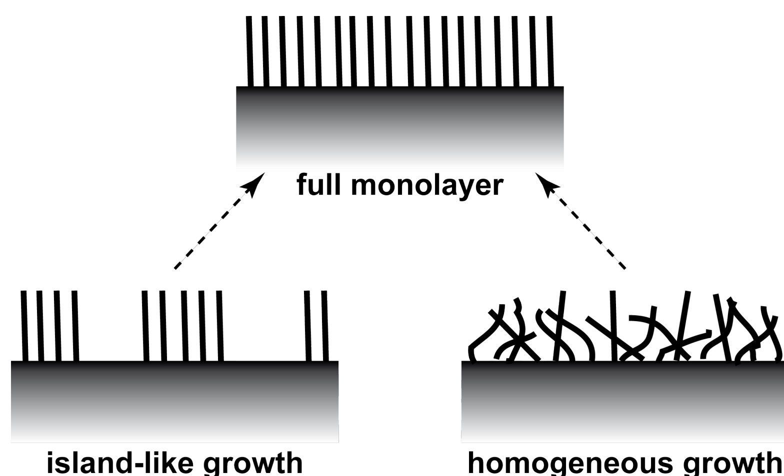

Figure 2.2.: Illustration of both possible types of growth. Island-like growth left and homogeneous growth right. Both types leading to a fully covered ordered monolayer.

One drawback for solution processed SAMs is the low cleanliness of the substrate. In vacuum chambers the substrates are cleaned by various methods until the pure surface is revealed. In solution processing there is always some surrounding atmosphere polluting the surface. Worst case this might be ambient air; a better way

of production is done in Argon or Nitrogen gloveboxes. Nevertheless how clean one works there will always be some contributions from the surrounding which are difficult to control entirely.
One crucial point is the order of the system (of long range or short range type). So far there has only been one system been reported that shows long range ordering. This ordering has been intensively investigated in this work by scattering techniques. If the system is lacking of scattering elements or long range order infrared spectroscopy, ellipsometry or x-ray reflectivity are appropriate tools for self-assembled monolayer characterization.

2.3. SAMs as surface modification

Frequently the SAM itself is used to change the chemical (wetting properties, surface energy,...) or physical (roughness, lubrication,...) properties of a surface. It might also be used to introduce a patterned surface or some mechanical property (surface islands or stripes). Therefore SAMs have attracted much attention in the field of surface engineering. Also the modification of the charge layer properties by SAMs [28, 29, 30] with an oriented dipole or a space charge layer is reported. The Schottky barrier can be tuned by such oriented dipole layers. The reproducibility of the SAM formation is the key feature for surface modification. Summarinzing the possible intentions of surface modification by SAMs there is a possible change in molecular ordering (packing) [31], shifting of the threshold voltage by introduction of fixed dipoles or a space charge layer by the SAM [28, 29, 30], or decreasing the trap density at the interface.
A study on the structure and electrical properties of pentacene and pentacene based TFTs in context with OTS layers shows the tremendous effects of a SAM at the gate dielectric of a TFT [31]. The fabrication of OTS layers is well studied [20]. Depending on temperature, humidity and surface roughness an ordered and an unordered state of OTS can be fabricated. There is an effect on the growth

behavior of the pentacene followed by a variation in the device performance. On the ordered OTS layers the surface induced thin film grows with a higher quality (*i. e.* larger crystallites, small mosaicity) than on the unordered layers. Consequently the pentacene films show higher mosaicity on the unordered OTS layers. *I. e.* the crystallites are less ordered. The crystallinity of Pentacene is directly correlated to the mobility of a TFT and hence devices using an ordered OTS layer show better electrical performance together with higher crystallinity.

2.3.1. Homogeneously spaced chemical properties

Sometimes it is of interest to spread a chemical functionality over a surface and separate this function somehow. By SAMs it is not possible to put the function however to a certain predefined point. The distribution of the functionality is homogeneous but can be located with some defined separation from each other. For example if a rather bulky molecule is used for a first SAM layer this will leave small spaces in between the bulky heads of the first type of molecule where a second type of smaller molecules can fit into this pores in a second SAM formation process step [32]. It is also possible to mix a functional head with a passivated head group molecule - both having the same affinity to the substrate which would lead to a homogeneous distribution of the functionality over the surface [33]. The use of a cone shaped molecule with a special function on top provides a rather defined pattern of function spread over the surface [34]. This functions can be used e. g. for immobilization of biomolecules.

2.3.2. Patterned SAMs

It is also of special interest to produce nano-patterned surfaces. The SAM in that case is used as the as a homogeneous structure that can be patterned by various techniques - depending on the molecular structure [35, 36]. E. g. a photo-reactive head can be patterned by UV irradiation. By this technique a mask structure can

be transfered to the SAM surface resulting in any 2D pattern of function as for example stripes [37].

3. Structure of a Quinquethiophene SAM

3.1. Motivation

There is much work done in the field of organic electronics in direction of organic thin film transistors (OTFTs). A special type of such an OTFT built from a self-assembled monolayer (a so-called SAMFET) has already been proposed in the 1970s [38] since the charge carrier transport happens within the first monolayer [39]. The organic semiconductor forms spontaneously on the gate dielectric in such a bottom-up constructed device. The approaches that were taken lacked of reasonably high mobilities on large scale channels due to hampered charge carrier mobility. The issues are defects and the low lateral π-π overlapping within the self-assembled monolayer [40, 41] which has been proven to be crucial for example in pentacene monolayers [42] or ordered oligothiophenes [43].

2008 an approach based on α-substituted quinquethiophene has overcome these issues [17]. The SAMFETs have been built with a yield of one. This result encouraged the fabrication of integrated circuits like bit-generators or ring oscillator which nicely worked as shown in figure 3.1. Circuits up to 200 transistors have been realized successfully.

Similar results of the same system based on a organic dielectric have been published recently [15]. The schematic structure of such a device is shown in figure 3.2. The same integrated circuits that had been realized on the Si-oxide gate di-

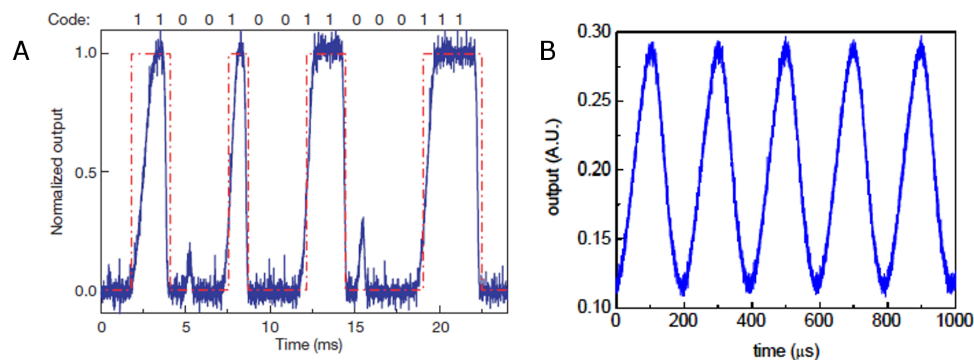

Figure 3.1.: 15-bit code generator (A) working at a supply voltage of -40V based on SAMFETs. The code is indicated on top and by the red line. A ring oscillator output working on a frequency of 5kHz at a supply voltage of -10V (B). Both images taken from [17].

electric have successfully been realized on the SU-8 photoresist as shown in [17]. The approach on the organic dielectric presents a crucial step towards integrated circuits of SAMFETs on flexible substrates.

The issue of scaling of the charge carrier mobility in SAMFETs with channel length has been studied intensively on that system in a separate publication [18]. It has been found out experimentally and confirmed theoretically that the exponential decrease of the charge carrier mobility is directly connected to low coverage, that means the submonolayer state of the SAM. For complete coverage, *i.e.* full monolayers the SAMFETs behave like devices based on a bulk organic semiconductor.

The increase of mobility (linear mobility equals saturated mobility) with increasing channel length (figure 3.3 A) is attributed to the contact resistance and has been followed for a larger number of devices shown in part B of the figure (taken from [17]). Mean values and deviations are given in table 3.1.

The scaling of the mobility with channel length is followed in figure 3.3 C taken from [18].

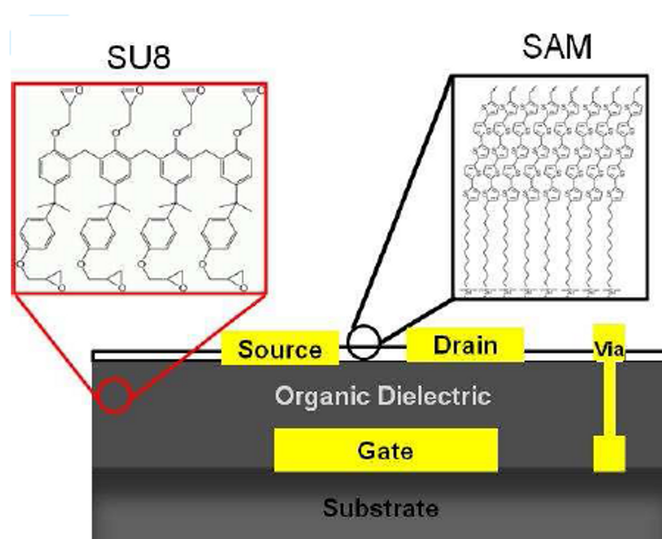

Figure 3.2.: Scheme of the device layout based on a silicon wafer and gold contact line from bottom. On top of that the dielectric SU-8 is applied on which the top contacts and SAM is deposited. The gold via on the right is needed for the integration of circuits. Image taken from [15].

Table 3.1.: Linear mobility for several devices with a varying channel length. The distribution has been fitted by a Gaussian distribution and mean value and width are given in the table (data taken from [17]).

channel length $[\mu m]$	mean $[cm^2V^{-1}s^{-1}]$	width $[cm^2V^{-1}s^{-1}]$
0.75 - 2	0.011	0.005
2.5 - 5	0.019	0.007
7.5 - 20	0.025	0.01
30 - 40	0.04	0.005

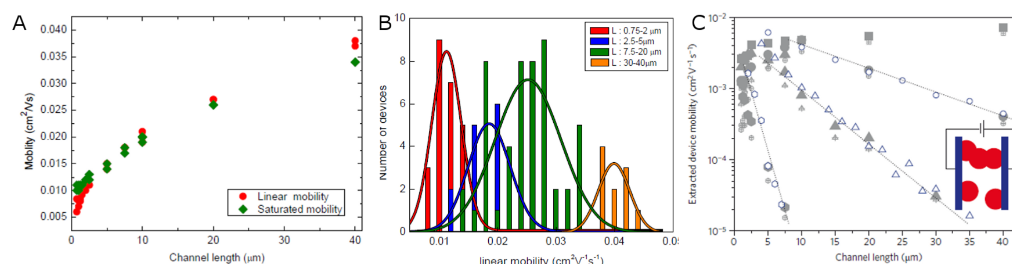

Figure 3.3.: Linear and saturated mobility versus the channel length (A). Distribution of linear mobility for a number of devices and various channel lengths (B). Histograms are fitted by a Gaussian distribution. The scaling of the linear mobility (crossed symbols) and saturated mobility (filled symbols) with layer coverage (C). The coverages by AFM determination are 0.05 ± 0.05 (hexagons), 0.31 ± 0.08 (triangles), 0.5 ± 0.1 (dots), and 1 (squares). Open symbols present results from corresponding theoretical calculations. Images A and B taken from [17], C taken from [18].

3.2. Molecular design - Layer formation

The active molecule chloro [11-(5""-ethyl-2,2':5',2":5",2"':5"',2"" - quinquethien-5-yl) undecyl] dimethylsilane (figure 3.4) is built from three essential functional parts, i.e. an anchoring group that binds the molecule to the substrate, a dielectric spacer group and a semiconducting section built of quinquethiophene. A monochlorosilyl docking end showed appropriate reactivity on Si-OH surfaces. The important point is the use of a single functional end to prevent uncontrolled agglomeration of the molecules [10]. If the two anchoring groups react with each other the molecules can no longer contribute to the layer formation. The chlorine reacts with water of the solvent and forms an OH-group + HCl. The OH-group can then bind to the Si-OH surface [44, 45]. Figure 3.5 shows a schematic view of the layer formation. The active molecule is not purified from its passivated counterpart and is used in a 50% mixture with passivated molecules which do not contribute to the layer formation

on first sight. Experiments using a 9:1 ratio of active:passivated molecules however reveal problematic layer formation *i. e.* a large amount of precipitation and 3D agglomeration.

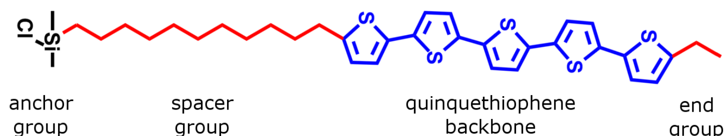

Figure 3.4.: Composition of the active Quinquethiophene molecule.

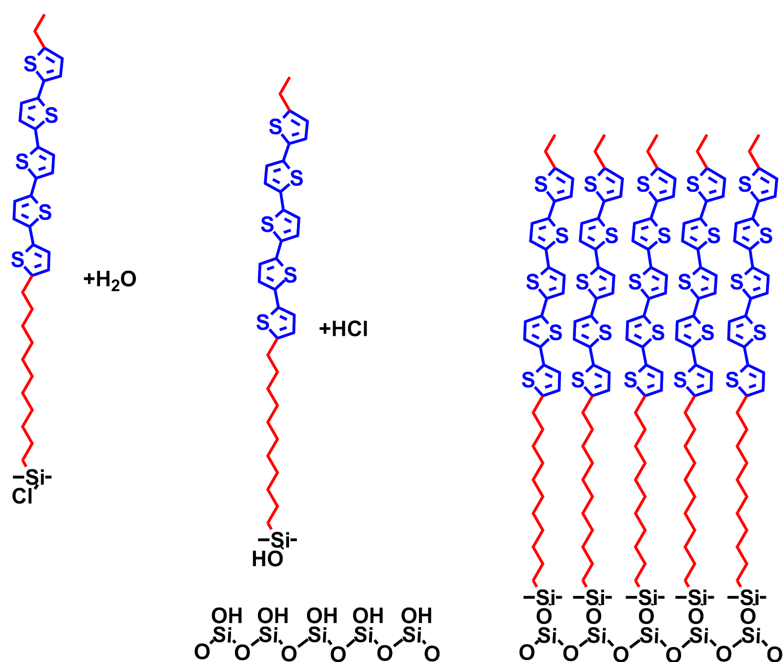

Figure 3.5.: Scheme of the layer formation and the chemistry of binding to the substrate.

The intention has been to combine the dielectric and the semiconducting sections of an organic field effect transistor (OFET) into one molecule. Therefore a long aliphatic spacer group, an undecane alkyl chain has been used with intention of

providing the dielectric layer. The flexible spacer length (C6 in stead of C11 has been tried) however showed only small influence on the mobility in devices.

The semiconducting quinquethiophene turned out to be the optimal tradeoff between mobility on the one hand and solubility on the other hand. Molecules using quaterthiophene showed an order of magnitude lower mobility and sexithiophene molecules lacked of solubility. The free end of the thiophene is capped by a C2 chain. Details on the molecular design and on layer fabrication are given in the supplementary information of Ref. [17].

For the formation of the self-assembled monolayer itself it is necessary to submerge a suitable substrate (OH-groups at the surface) into a solution for a certain time; at least 24 hours to achieve a closed monolayer. Figure 3.6 shows two possible types of alternative film growth as it cannot be excluded so far. On the left side of the picture some molecules are upside-down in the stack of thiophene units. The alkyl chains indicated here fully upright standing will due to their flexibility not stand up like this but bend around on the surface. The other type of unwanted formation are not covalently bond molecules which are one or more thiophene units off the optimal stack. This reduces the overlapping of the charge carrier transporting π orbitals reducing the mobility of the charge carriers [46]. Both types of layer formation have not been proven or excluded by experiments but they are supposed to be found to some extend within the layers. The contribution of passivated molecules is not yet clear, but the problematic layer formation using the 9:1 ratio of active to passive molecules indicates that they play a non negligible role.

The formation from the submonolayer to the closed monolayer can be followed for example by AFM topography imaging (figure 3.7). It is nicely seen in the AFM topography images that a closed monolayer is formed after approximately 24 hours in solution and further time in solution does not change the topography of the layer. From that it can however not be clarified whether some molecules are built in standing upside down with their spacer chains up. This point is still

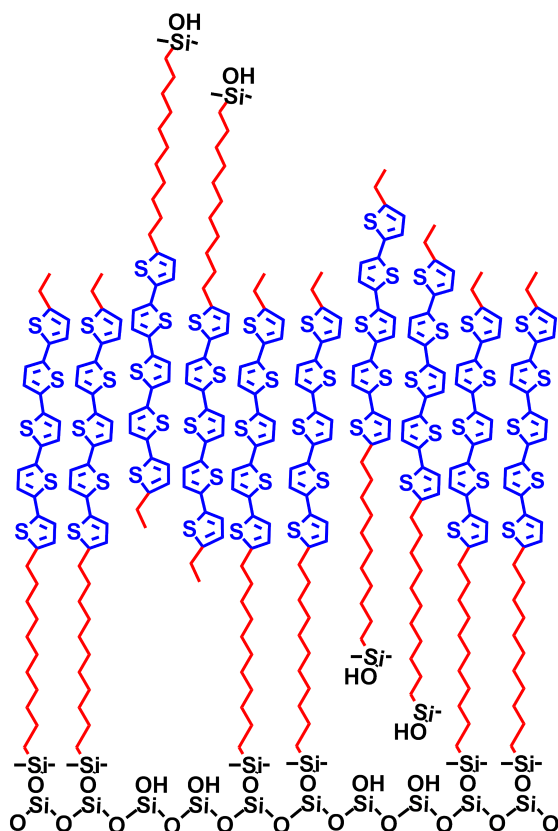

Figure 3.6.: Two types of unwanted but possible layer formation. Left molecules are upside-down in the SAM with their thiophene backbones at the right position or slightly shifted. On the right some molecules are indicated not to be attached to the substrate and also not at the right height with the thiophene units

not clear but it is very likely to be the case for some parts of the layer. After taking the samples out of the solution they are usually annealed at 400K which is required for the device fabrication. Without the annealing step the mobility has turned out to be one order of magnitude lower than after the annealing step. The effect of annealing will be discussed in detail in a following section.

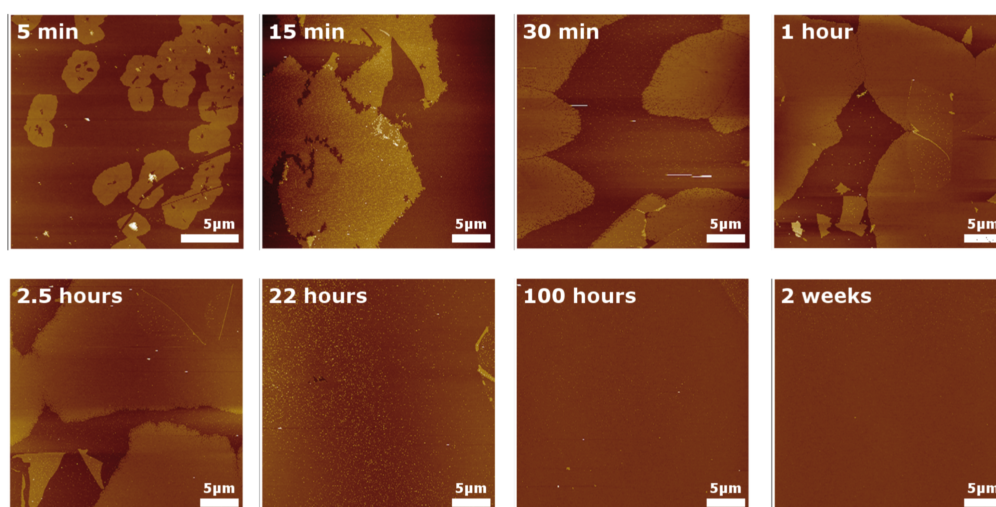

Figure 3.7.: Layer formation monitored by AFM. Topographical images from the early submonolayer to a closed monolayer.

3.3. X-ray investigations

X-ray reflectivity (XRR) experiments on the monolayers have been performed on a laboratory system, namely a Bruker D8 diffractometer using copper radiation from a sealed tube. Two different setups of x-ray optics have been used - both giving the same experimental results. The difference has been on the primary side optics using on the one hand slit optics with 0.05mm slit and on the other hand a parallelizing göbel mirror in combination with a 0.1mm slit. The secondary side has been the same for all experiments using an automatic absorber in front of

0.1mm slits for the secondary side slit and receiving slit. For room temperature experiments no protective environment has been used. Temperature annealing experiments have been performed on a DHS1100 from Anton Paar Ltd using a PEEK dome and He atmosphere for sample protection. XRR evaluation has been done using the software package WINGIXa using Parratt's recursive algorithm [47] and including roughness according to the Approach of Nevot and Croce [48]. Some XRR measurements have been performed on different setups as for example the beamline ID10b of the ESRF in Grenoble, France and on a Panalytical Multi-Purpose Diffractometer (MPD) test setup provided by Panalytical in Almelo, The Netherlands. Results and discussion on that are given in the appendix and differences are rather addressed to the time between the measurements than to the experimental setups.
Grazing incidence x-ray diffraction experiments have been performed at two similar beamlines at two different synchrotron radiation facilities, G2-line of the Cornell High Energy Source (Chess) [49, 50] and ID10b at the European Synchrotron Radiation Facility (ESRF) [51]. At both beamlines the angle of incidence is adjusted by the tilt of the sample versus the horizontal beam. At the G2-line a He filled mylar dome has been used to protect the samples from degradation. The beamline ID10b has been used in horizontal geometry using as stage and sample protecting environment a DHS900 from Anton Paar Ltd with its PEEK dome. As protecting gas He has been used. Detection of the signal has in both cases been done using a gas filled position sensitive wire detector (PSD) provided by the beamline installation. Data visualization and evaluation has largely been done using PyGid, an x-ray analysis software developed by Armin Moser at the Institute of Solid State Physics, TU Graz.

3.3.1. X-ray reflectivity

Investigations on the homogeneity and layer thickness of the SAM have been performed by x-ray reflectivity (XRR). It has not been possible to do XRR mea-

surements on submonolayer samples due to the lateral inhomogeneity in that case (island like growth). For all closed monolayers a two layer model has been used to reproduce the experimental data. One layer for the alkyl spacer region and a top layer representing the quinquethiophene backbone. The box model is shown in figure 3.8 together with a representative XRR measurement that has been evaluated and fitted using WINGIXa.

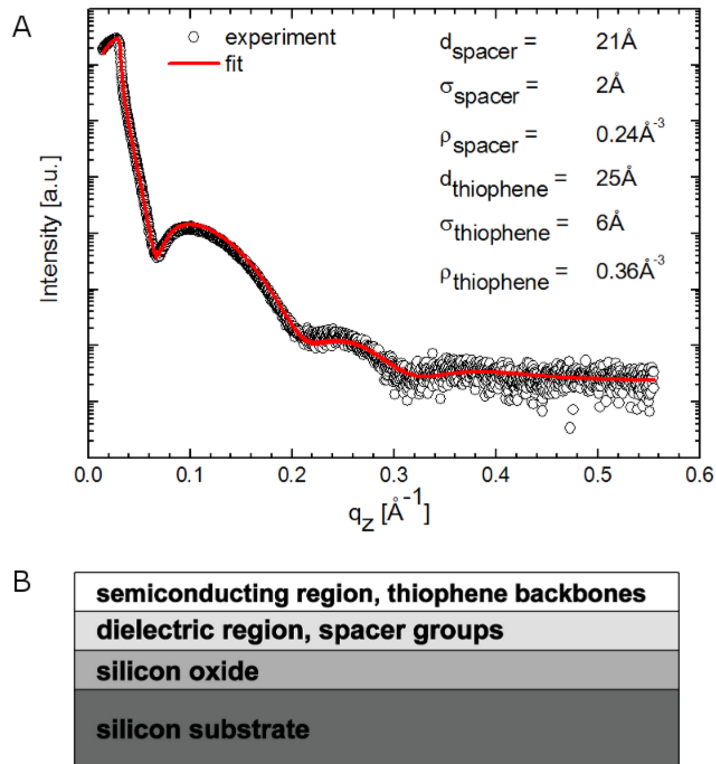

Figure 3.8.: Theoretical model for the simulation of the x-ray reflectivity data using a two layer model for the self-assembled monolayer on top of the substrate (B) and a measured XRR curve together with its simulation (A).

Experimentally the thickness of the layers is higher than expected from calculations and also thicker than in investigations of holes and submonolayers by AFM.

Table 3.2.: Theoretically expected and observed values from the x-ray reflectivity measurements. d denotes the layer thickness, ρ the mean electron density of a layer and σ the root mean square roughness observed in the experiment. The subscript attributes the quantity to the layer.

	expected	observed
$d_{thiophene}[\AA]$	21	21-27
$\rho_{thiophene}[\AA^{-3}]$	0.48	0.33 - 0.41
$\sigma_{thiophene}[\AA]$	-	4 - 7
$d_{alkylspacer}[\AA]$	15	15-21
$\rho_{alkylspacer}[\AA^{-3}]$	0.34	0.17 - 0.28
$\sigma_{alkylspacer}[\AA]$	-	2 - 4
$\rho_{siliconoxide}[\AA^{-3}]$	0.68	0.66

Additionally the electron density is too low (see table 3.2). The reason for that is no yet fully understood but at the moment an explanation could be that a thicker layer with lower electron density is made of the same amount of material as the thinner layer with higher density. There might be some systematic error within the XRR measurements or data evaluation. Also the presence of some water layer on top of the SAM or on the substrate cannot be excluded by the present data. The samples have been transported and stored under ambient conditions!

3.3.2. Grazing incidence x-ray diffraction

Grazing incidence in-plane diffraction experiments have been performed to investigate the crystalline structure of the quinquethiophene units in their lateral order [52]. It has been found that the layers are made of long-range ordered crystalline domains. For a monolayer one would expect Bragg rods from the experiments.

Bragg rods are found for the monolayer because the lateral large number of repeating units confines 2 dimensions in reciprocal space and provides a narrow signal in q_p and the lack of repeating units in z-direction in real space gives an extended signal in q_z in the experiment. A scheme of the correspondence of dimensions for the system of a monolayer is given in figure 3.9.

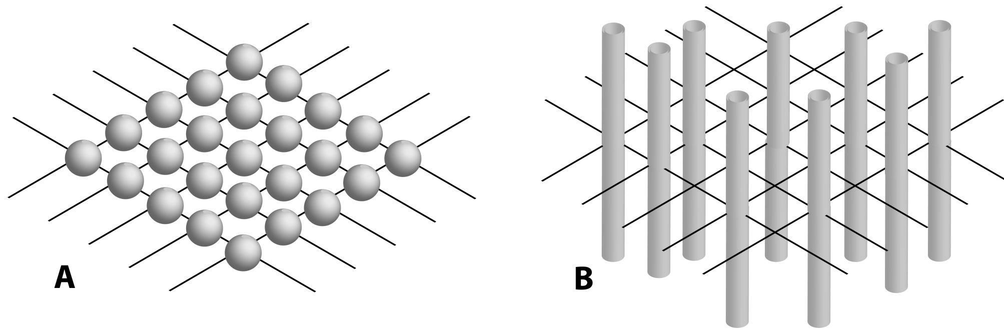

Figure 3.9.: A monolayer shown in real space (A) and the corresponding transformation to reciprocal space (B) (not all Bragg rods are shown in B).

Two examples of representative measurements are shown in figure 3.11. The data have been recorded at ID10 at the ESRF. Two types of reciprocal space maps have been found in the experiments - type 1 shows a typical Bragg rod appearance (figure 3.11 A) with a steady decrease [53] of intensity along q_z above the sample horizon (i.e. the Yoneda reflection [54]). The other type is shown in figure 3.11 B presenting increased intensity at higher q_z. This can be interpreted by 3D layer formation (which we can exclude from AFM and XRR measurements) or by a phase of tilted molecules [55]. In the case of tilted molecules the maxima of the structure factor (defining the distances within the crystal) intersects the molecular form factor above the sample horizon at higher q_z. The molecular form factor is usually highest perpendicular to the long molecular axis and hence it is for tilted molecules not perpendicular to the structure factor. The scheme in figure 3.10

where the direction of the maximum molecular form factor is represented by the green arrow and the positions of the largest structure factor is shown by the black lines should illuminate this picture.

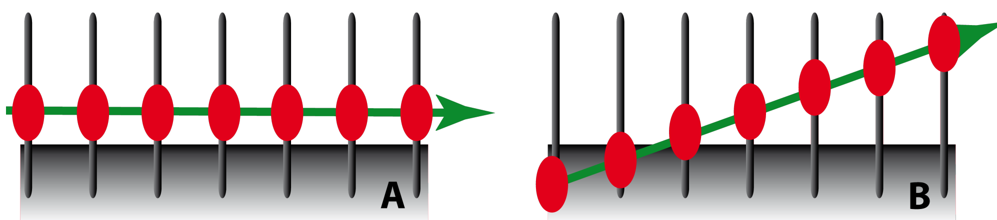

Figure 3.10.: Schematic view of the appearance of intensity maxima for monolayers. A shows the the situation for upright standing molecules and B the corresponding picture for tilted molecules. Black lines are the positions of the Bragg rods by the structure factor, the green arrow is the molecular form factor and the red ellipses give the intersections of structure factor and molecular form factor where peaks can be expected. The black horizontal line is the sample horizon above which the diffracted beam can be observed.

The difference of the two samples is that the first type has been measured after the substrate has been taken out of the solution and the other one has been annealed for 1 hour at 400K before the x-ray scattering experiments; hence the two types are called not-annealed or pristine phase and annealed phase in the further discussion. Figure 3.11 C-E show the integrated intensities of the reciprocal space maps of A and B. The line profiles are integrated over the width of the rod in direction of q_p and plotted with the intensity scale for the pristine phase on the left and the phase of tilted molecules on the right side. The area of integration and the absorbers during the experiment have been the same and hence it is obvious that the scattering signal from the tilted molecules is lower than from the upright standing molecules. This can be understood in a sense of non uniform tilt. Not all of the molecules are tilted exactly with the same angle and in correspondence to the change in the tilt angle the unit cell dimensions change slightly. A larger tilt of the molecule forces a larger unit cell. Hence not a fully straight rod perpendicular

to q_p is found but a distribution of angles and distances leading to the arc-like shape of the Bragg rods in case of the annealed films.

As the phase of upright standing molecules is a more defined structure (all molecules 100% upright) this arc-like feature is not found in reciprocal space maps of not annealed samples. Nevertheless the length of the molecular thiophene backbone ($L = 21\AA$) corresponds to the FWHM in q_z of the rods by $2\pi/L = FWHM_{q_z}$ [55]. The determination of of the unit cell parameters and the explicit calculation of the molecular tilt and tilt direction is described in the next section.

3.4. The 2D crystal structure parameters

The knowledge about the crystalline structure of other α-substituted oligothiophenes leads to the attempt of indexing the Bragg rods in the reciprocal space maps with highest intensity reflections of a herringbone (compare figure 3.11). This assumption leads to a unit cell which explicit shape is calculated by the position of the Bragg rods in direction of q_p and q_z. Similar calculations have been shown for monolayers of fatty acids [56, 57, 58]. The packing of the molecules within the unit cell cannot be determined from the experimental data solely, but density functional theory provides information on how the molecules align within the experimentally determined unit cell.

3.4.1. The unit cell

The initial interest after the experiments is the determination of the unit cell. A good starting point concerning the structural investigation is an oblique unit cell which is assumed to be distorted from the rectangular unit cell by an angle α. According to figure 3.12 the unit cell parameters in real and reciprocal space are assigned as follows.

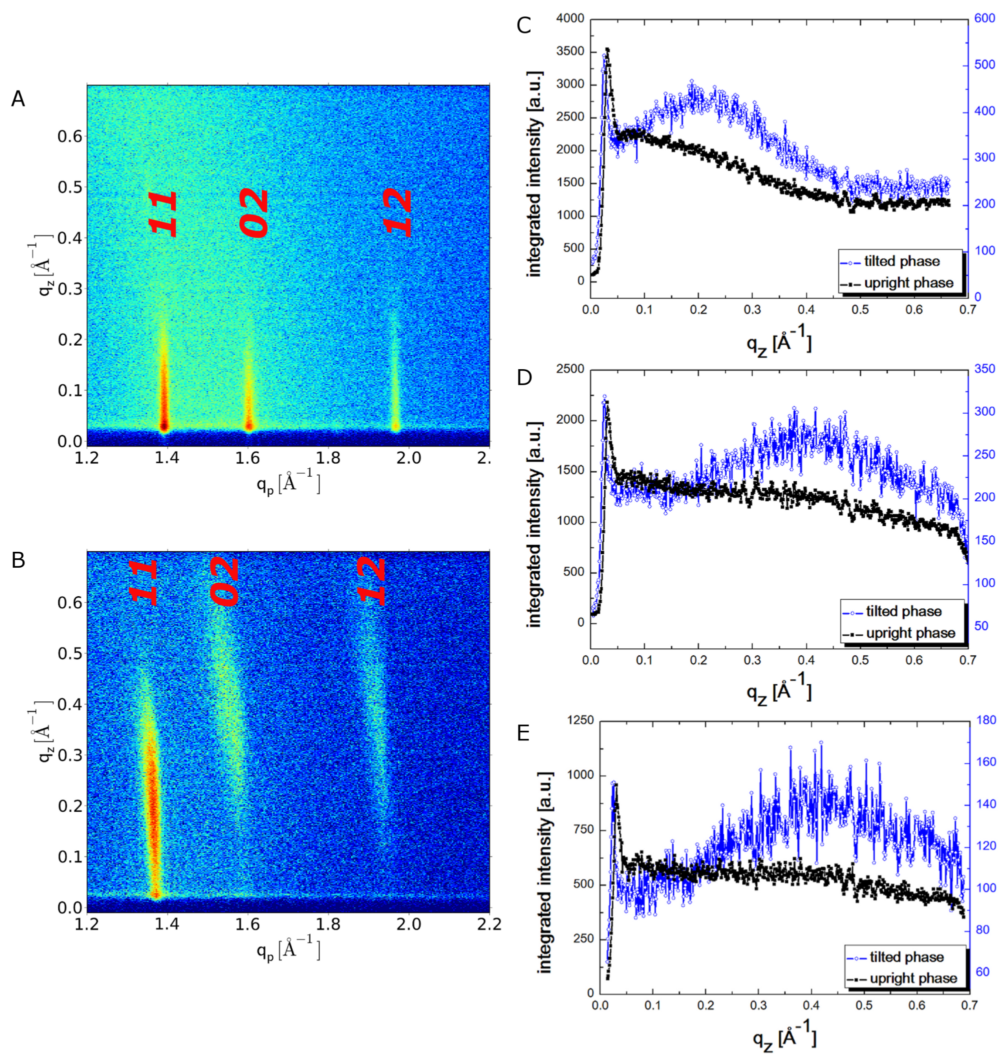

Figure 3.11.: Reciprocal space maps of the as prepared state (A) and the annealed state (B) of the 5T-SAMs. C-E show intensities over q_p for the 11-rod (C), the 02-rod (D), and the 12-rod (E) of the reciprocal space maps (A, B).

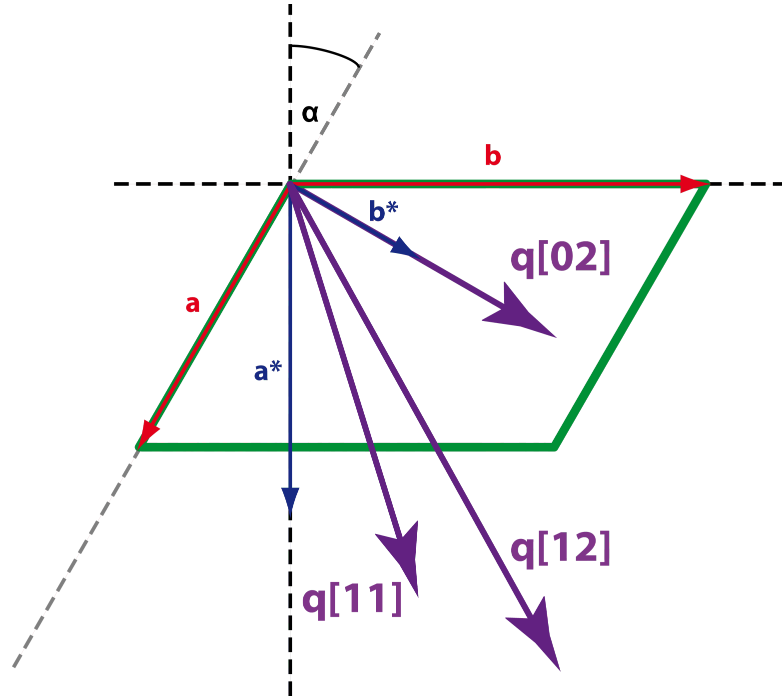

Figure 3.12.: Schematic view of the 2-dimensional oblique unit cell (a, b) showing the distortion from the rectangle α and the directions of the scattering vectors (purple arrows).

$$\mathbf{a} = \begin{pmatrix} -a\sin\alpha \\ -a\cos\alpha \\ 0 \end{pmatrix} \tag{3.1}$$

$$\mathbf{b} = \begin{pmatrix} b \\ 0 \\ 0 \end{pmatrix} \tag{3.2}$$

$$\mathbf{a*} = \frac{2\pi}{ab\cos\alpha}\begin{pmatrix}0\\-b\\0\end{pmatrix} \tag{3.3}$$

$$\mathbf{b*} = \frac{2\pi}{ab\cos\alpha}\begin{pmatrix}a\cos\alpha\\a\sin\alpha\\0\end{pmatrix} \tag{3.4}$$

The required scattering vectors are shown in figure 3.12 by the purple arrows and the equations are given by:

$$\mathbf{q[11]} = \mathbf{a*} + \mathbf{b*} \tag{3.5}$$

$$\mathbf{q[02]} = 2\mathbf{b*} \tag{3.6}$$

$$\mathbf{q[12]} = \mathbf{a*} + 2\mathbf{b*} \tag{3.7}$$

From these sets of equations the unknown parameters a, b, and α of the 2-dimensional unit cell can be expressed.

$$a = \pi\frac{4q_p^2[12] - 4q_p^2[11] - 3q_p^2[02]}{\cos\alpha\sin\alpha\; q_p[02]\;\{2q_p^2[12] - q_p^2[02] - 4q_p^2[11]\}} \tag{3.8}$$

$$b = \frac{4\pi}{\cos\alpha\; q_p[02]} \tag{3.9}$$

$$\sin\alpha = \frac{\{4q_p^2[12] - 4q_p^2[11] - 3q_p^2[02]\}}{q_p[02]\;\{2q_p^2[12] - q_p^2[02] - 4q_p^2[11]\}} \times\sqrt{\frac{\{4q_p^2[11] - q_p^2[02]\}}{8\;\{1+\frac{4q_p^2[12]-4q_p^2[11]-3q_p^2[02]}{\{2q_p^2[12]-q_p^2[02]-4q_p^2[11]\}}\}}} \tag{3.10}$$

Using the q_p values of the experimental data together with the indexation as herringbone packing for input one can calculate shape and dimension of the unit cell.

In numerous experiments the deviation from the rectangular unit cell has been found to be $\alpha = (0 \pm 2)^\circ$.
This framework is valid for Bragg rods with highest intensity at the horizon and steady decay in direction q_z as well as for rods which show maximum intensity at q_z quite above the horizon. In order to determine the differences between these two types of structures further calculations including the position of increased intensity in direction of q_z are performed. The general equation

$$\tan\theta\, G_{hk}\ \cos\beta_{hk} \ = \ q_z^{hk} \tag{3.11}$$

can be evaluated in the context of the SAMs [55]. G_{hk} represents a reciprocal lattice vector. This evaluation gives for the direction of the tilt of the molecules (Ω angle between the projection of the long molecular axis to the ab-plane and the b-axis) and for the tilt from the upright standing position of the molecule (Θ) the equations as given here:

$$\sin\Omega \ = \ \frac{q_z[02]G_{11}\ \cos\delta - q_z[11]G_{02}}{q_z[02] * G_{11}\ \sin\delta} \tag{3.12}$$

$$\tan\theta \ = \ \frac{q_z[02]}{G_{02}\ \cos\Omega} \tag{3.13}$$

The position of the angles is shown in figure 3.13. In numerous experiments the direction of the tilt has been in the direction of the b-axis corresponding to $\Omega = (0 \pm 3)^\circ$, whereas the error is negligible.
Table 3.3 gives the averaged values found in experiments for the unit cell parameters of various samples. The uncertainty in the parameters is a sign that there is no unique solution for the SAMs as expected for crystals. There is always a small variation which is attributed to a rather soft packing within the 2-dimensional layer. Another factor is the formation in the solution and a preparation under atmospheric conditions where the substrate can always differ slightly. As the packing

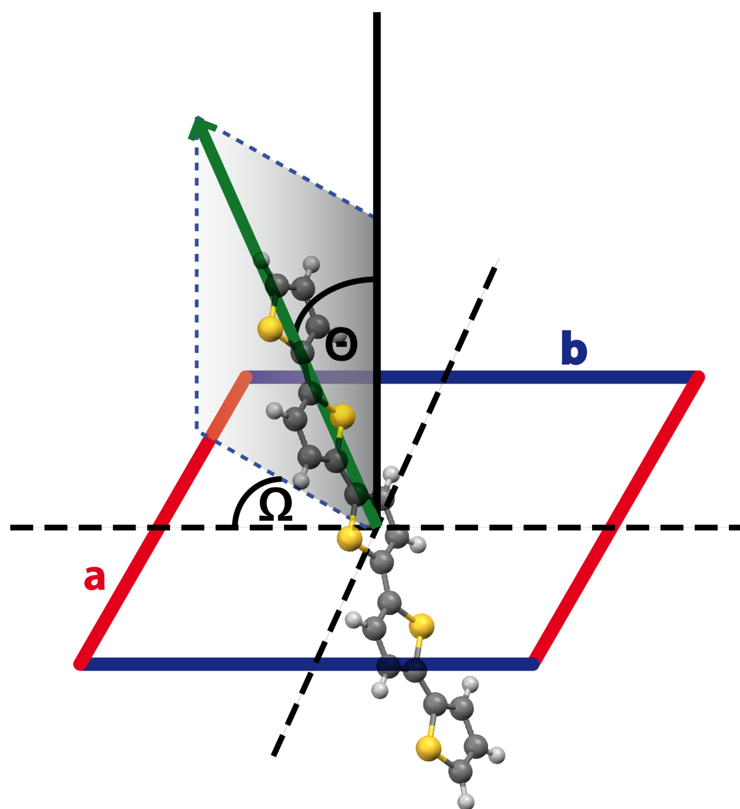

Figure 3.13.: Schematic view of the tilt of the molecule (Ω) inside the cell and the tilt direction (β)of the molecules.

Table 3.3.: Unit cell parameters obtained for the two phases. Values give an average over all samples. Unit cell axis a and b, distortion from the rectangular cell α, tilt angle of the molecule θ, direction of the molecular tilt Ω, and the volume per molecule V_M.

phase	a [$\mathring{A}$] $\Delta = \pm 0.15$	b [$\mathring{A}$] $\Delta = \pm 0.15$	distortion α [deg.] $\Delta = \pm 2$	tilt angle θ [deg.]	tilt dir. Ω [deg.]	volume V_m [$\mathring{A}^3$]
pristine	5.61	7.85	0	0	–	456 ± 7
annealed at 400K	5.60	8.1	0	13 ± 2	0 ± 3	462 ± 11

of the molecules is not absolutely dense a comparison to other α-substituted oligothiophenes indicates that the solution fits well into the list of results found for these materials in the bulk according to the literature [59, 60] (figure 3.14). In thin film solutions the packing is usually slightly lower which is also found in the case of the SAMs. The inset shows the solution known from literature (pink triangle) and the black star represents the average of samples of the phase of annealed layers which is slightly above the linear correlation between the volume per molecule and the number of thiophene units for α-substituted oligothiophenes. As the volume per molecule for the SAM fits nicely to the other oligothiophenes it is proven that the spacer groups can be neglected in the considerations of the crystal structure. There is no long range order in the alkyl chains [61].

The point marked with the green sphere indicates the average value for samples annealed at temperatures between 400K and 500K. The data have been taken after cooling the samples to room temperature.

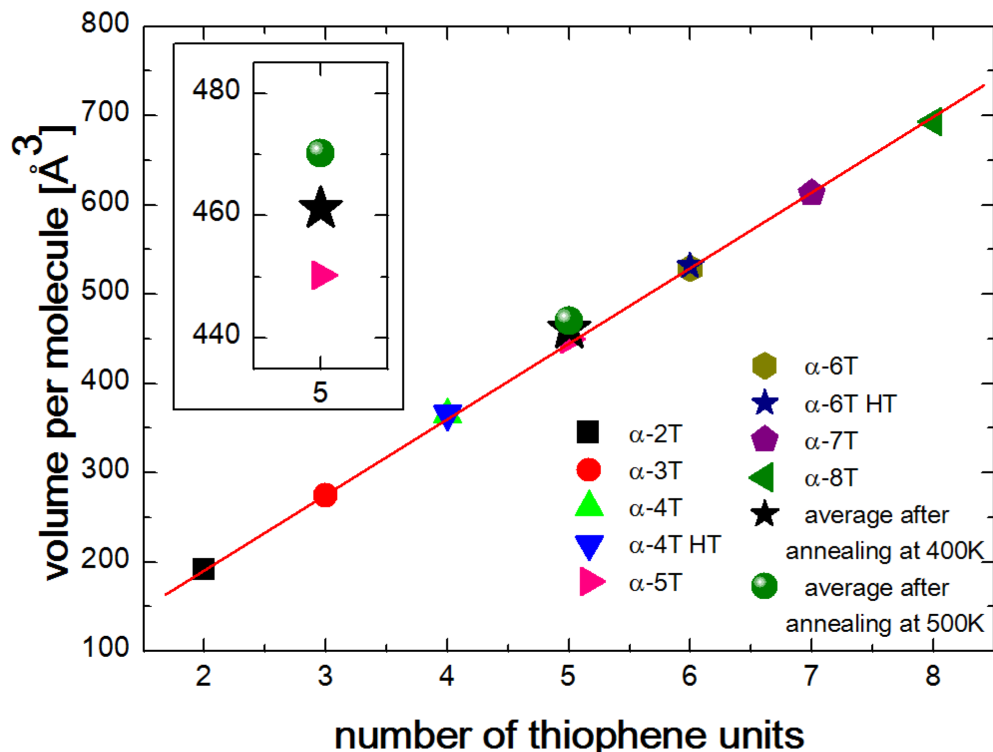

Figure 3.14.: Comparison of the volume per molecule found for the SAMs to the values known in literature for α-substituted oligothiophenes. The red line is a linear fit to the values given in literature. The inset focuses on the quinquethiophene.

3.4.2. The packing of the molecules - density functional theory

Ab-initio calculations have been performed using the a general gradient approximation within the framework of density functional theory (DFT) to determine the packing of the molecules inside the unit cell [62, 63]. As the unit cell is not unique a series of equally fabricated samples is used as input for the calculation. For the pristine phase this is $a = 5.625Å$, $b = 7.84Å$, $\Theta = 0°$ and for the phase of tilted molecules $a = 5.60Å$, $b = 8.106Å$, $\Theta = 14°$. Additionally the unit cell parameters $\alpha = 0°$ and $\Omega = 0°$ are used as input.

The monolayer is modeled by a stack of layers with a vacuum layer in between,

so called free-standing layers. The vacuum layer is chosen large enough that the separated thiophene layers do not feel any interaction with each other. The alkyl spacer groups are neglected in the DFT calculations as well as in the determination of the unit cell. There are two possibilities how the molecules can be packed into the unit cell as shown in figure 3.15 where the centered molecule is rotated 180 degrees along its long molecular axis. Both types result in the same herringbone angle but for type 2 the energetic minimum is deeper (figure 3.17) and therefore this packing is used in all further calculations.

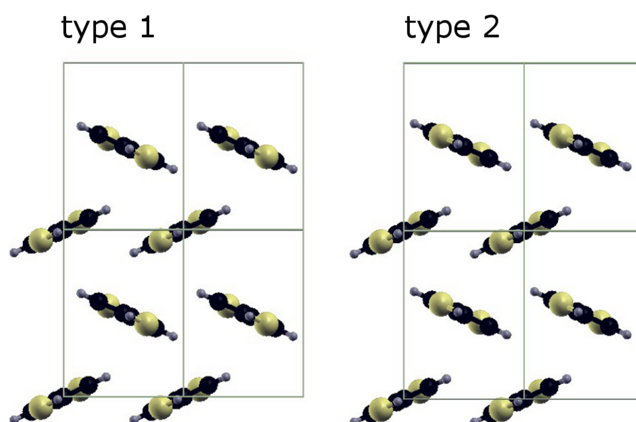

Figure 3.15.: View along the c-axis showing the two possible ways of putting the centered molecule into the unit cell of the fully upright standing molecules. The herringbone angle is the same for both types.

Figure 3.16 shows a single unit cell and the position of the herringbone angle β between the aromatic plane of the quinquethiophene and the b-axis as calculated in the framework of DFT within the unit cell.

DFT calculations provide a distribution of energy where the minimum in the energy marks the optimized herringbone angle. the optimized angle for the upright standing molecules is $\beta = 63°$ and for the phase of tilted molecules an angle of

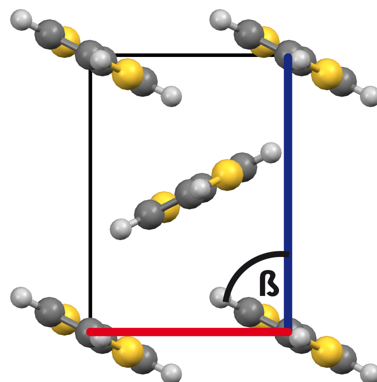

Figure 3.16.: Unit cell of type 2 with the position of the herringbone angle β between the aromatic plane of the molecule and the b-axis of the unit cell.

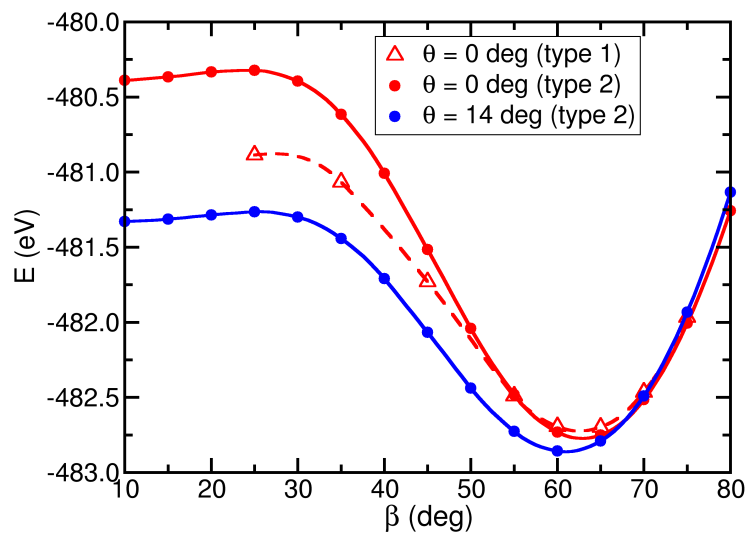

Figure 3.17.: The energy distribution for the variation of the herringbone angle for the different types of packing (type 1 and 2) of the pristine phase and for type 2 of the phase of tilted molecules.

$\beta = 60°$.
Figure 3.18 shows the band structure for both types of phases found for the SAM. From electrical measurements and device performance one would expect a broader HOMO (higher mobility in devices) for the tilted molecules but calculations show the behavior vice versa. The HOMO of the SAM with upright standing molecules is by a factor of two larger than the one of the structure with tilted molecules. This might be an indication that the limiting factor in the phase of upright standing molecules is not the crystal structure but something else. Nevertheless it is possible that the endgroup has a larger influence on the real system than expected and should therefore not be neglected in theoretical considerations.
DFT calculations suggest for both experimental unit cells a tilt angle of zero - fully upright standing molecules (figure 3.19). The curve for the upright standing molecules is much more narrow indicating that a tilting of the molecules is less favorable which corresponds to the smaller unit cell that does not provide much space for molecules to tilt. The curve for the tilted molecules however shows a very flat minimum for a tilt angle of zero. The energy variation is minimal for a large range of tilt angles ($\Theta = (0 \pm 5)°$) for that phase. Again the endgroups or spacer chains might have an impact on the real energy distribution in the SAM that cannot be considered in the DFT calculations.

3.5. Temperature annealing

As the effect of the annealing process step has turned out to have a tremendous effect on the structure of the SAM further investigations under influence of temperature are performed. The investigated parameters are:

* phase behavior under influence of temperature
* thermal stability of the crystal structure
* thermal stability of the layer

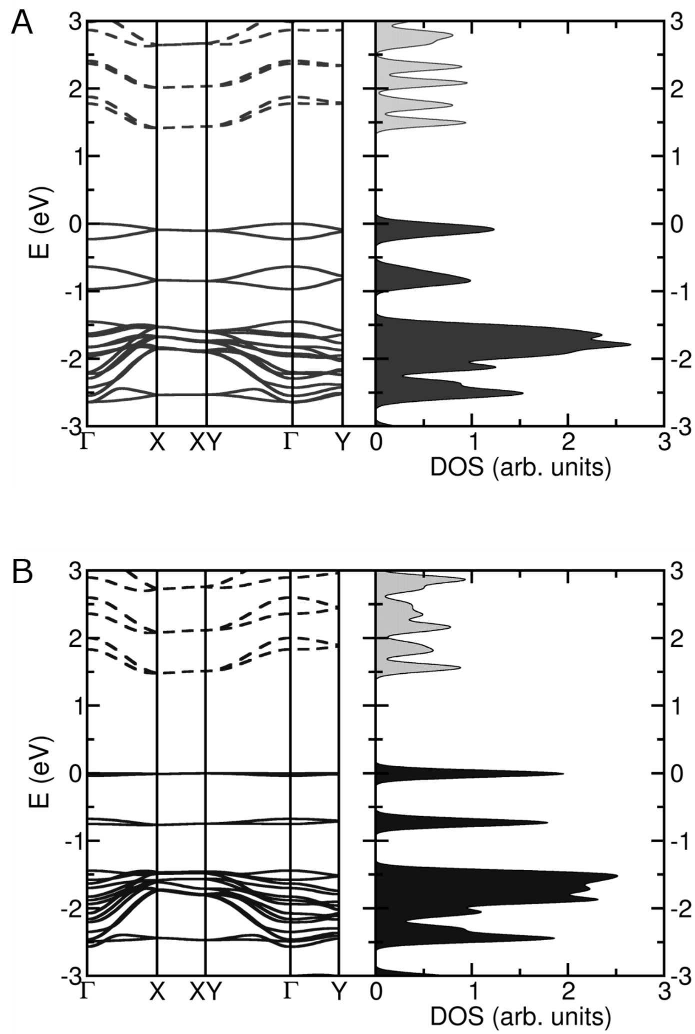

Figure 3.18.: Band structure and density of states for the upright standing molecules (A) and the tilted molecules as calculated from DFT.

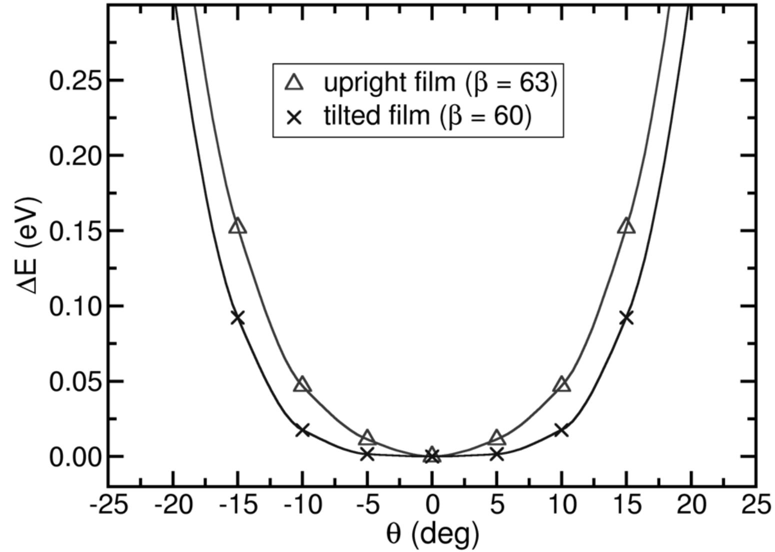

Figure 3.19.: A calculation of the relative change in energy of the two optimized structures as a function of the tilt angle of the molecules.

The experiments are performed in-situ because ex-situ investigations cannot provide the full information. Nevertheless in-situ temperature studies with x-rays have two problems. One is the time factor. The measurements take some time and if there is any deviation from the general measuring routine the time between measurements may vary. Additionally the time scale of changes is hardly feasible. The other issue is degradation of organic films under the x-ray beam in general and especially if additional energy is given to the system by heating of the sample. This issue and how it can be reduced or overcome is discussed in the appendix A.

Two important temperatures are already clear. Room temperature (298K) on the one hand where the preparation is done and 400K which is the annealing temperature during the device fabrication process. One interesting temperature is the melting temperature of quinquethiophene of 526K given in the literature [64].

3.5.1. Structure

Reciprocal space maps of the annealing procedures have been recorded and reduced to integrated line scans as already done for the presentation of figure 3.11. The temperature evolution can then easily be followed like for example in figure 3.20. Subplot A and B present the 11 rod of the SAM whereas C and D have been taken from the 02 rod. The line cuts show clearly that at elevated temperatures the molecules are always standing upright as the maximum intensity in plot A and C is always found at the sample horizon showing a steady decay along q_z. On the other hand at room temperature (B, D) there is a peak found above the Yoneda reflection which is clear evidence of tilted molecules as already discussed earlier. Additionally the intensities of the reflections are decreasing with higher temperature. At 520K there are still Bragg rods found but above the long range order of the crystal is lost. Once the crystal structure is lost it cannot be recovered by cooling the sample or keeping it at some kind of 'healing' temperature (400K, 450K, or 500K have been tried) in order to provide the possibility for the molecules to rearrange.

The temperature of 520K corresponds to the melting temperature given in literature [64] for quinquethiophene crystals of 526K which is slightly larger than in the monolayer state of the SAM under investigation. The sample has already been annealed at 400K in advance (otherwise the initial state shown by the black line in B and D should have upright standing molecules). A try to anneal the sample again at 400K shows that the structure that is obtained is identical to the structure obtained after the initial annealing step previous one. This states that the annealing process is reproducible in concerns of crystal structure as the maximum intensity in q_z does not shift as shown here (red line: B and D) and does not shift in q_p as well (not shown here).

The fact that the tilt angle is always zero at elevated temperatures is supported by figure 3.21 showing the tilt angle versus the temperature. The sample has repeatedly been heated and cooled (following the one and double sided arrows)

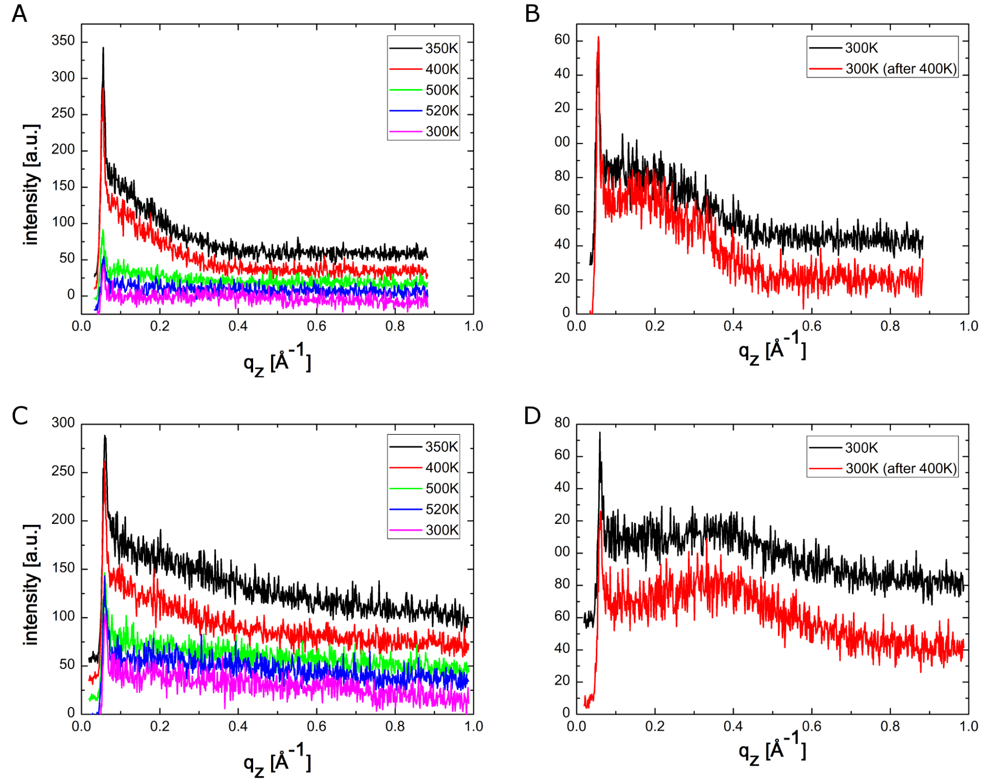

Figure 3.20.: Intensities integrated along q_p versus q_z during temperature treatment for the 11 rod (A, B) and for the 02 rod (C, D). The sample has been annealed prior to the experiment at 400K. All curves have been offset in intensity for clarity.

and at room temperature there is an increase in the tilt angle. The direction of the tilt is always towards the b-axis of the unit cell, *i. e.* there is no change of the structure at higher temperatures like a new phase evolving. The tilt after annealing at 400K seems to be reproducible. The room temperature structure of the SAM is a function of the temperature history.

The expansion of the unit cell is isotropic as shown by figure 3.22. Both unit cell parameters expand approximately the same amount (equally scaled axis). The volume expansion is also shown in part A including the reversible part of the

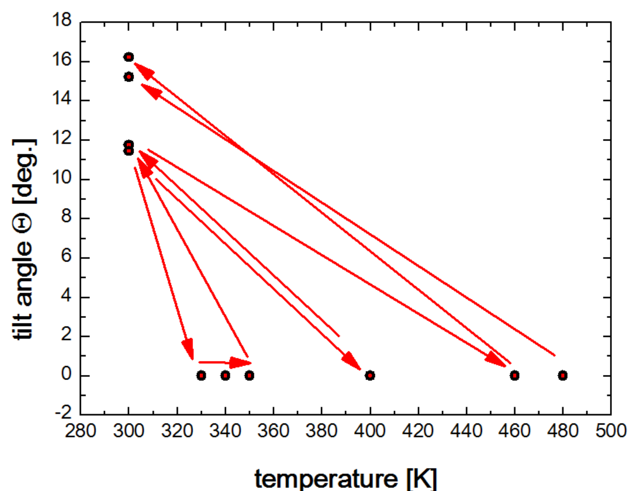

Figure 3.21.: Evolution of the tilt angle of the molecules with increased temperature of a sample that has been annealed prior to the experiment at 400K.

cooling process. The cooling is not fully reversible which is attributed to desorption of molecules leaving free space that can be filled by the remaining molecules. After cooling to 400K the sample has been heated above the melting temperature, hence no cooling to room temperature can be presented in this figure.

Of additional interest is the evolution of the internal structure of the quinquethiophene due to temperature annealing. Experimentally this is not accessible but again DFT calculations are employed to determine the packing of the molecules inside the unit cell. Energetic minimizations (figure 3.23) have been performed for each temperature and unit cell given in table 3.4. The differences in the herringbone angle are small, even between the films of upright standing molecules and the tilted counterpart but there is a trend of opposite evolution found. For larger unit cells of the room temperature phase of tilted molecules the herringbone angle increases with increasing size of the unit cell. The herringbone angle at elevated temperatures (and hence upright standing molecules) develops vice versa. It decreases with increasing lattice constant a which corresponds to a higher tem-

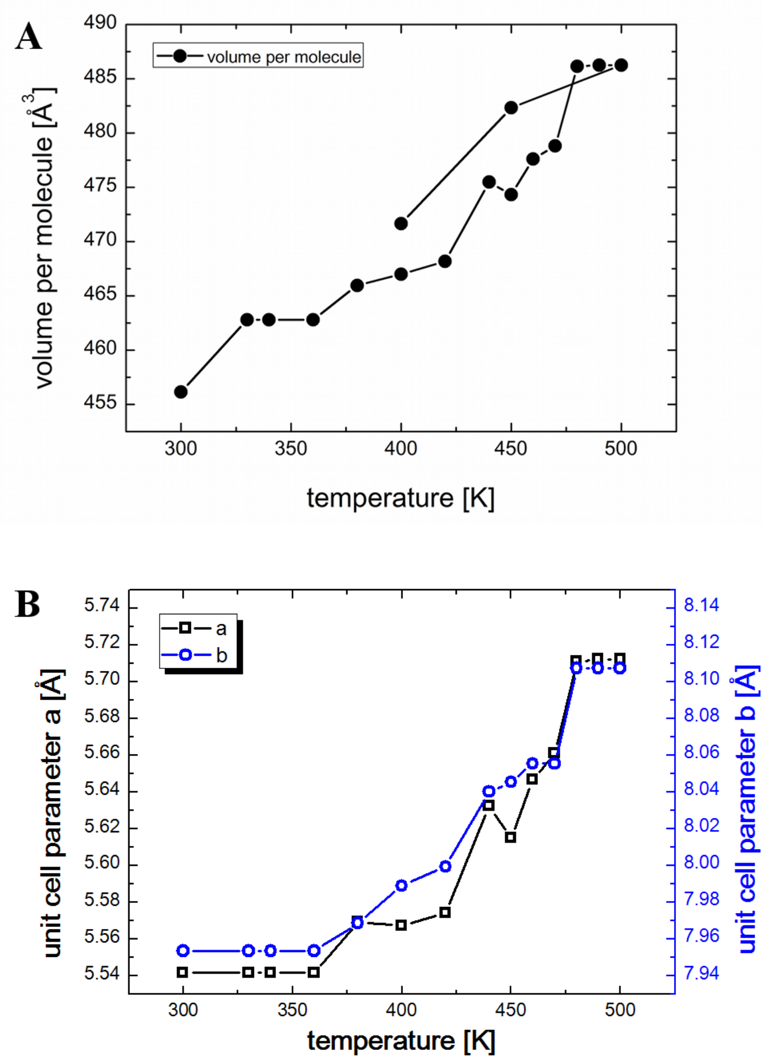

Figure 3.22.: Evolution of the volume per molecule for the unit cell during heating an cooling down again (A). The evolution of of the unit cell parameters a and b for the same sample during heating (B).

perature.

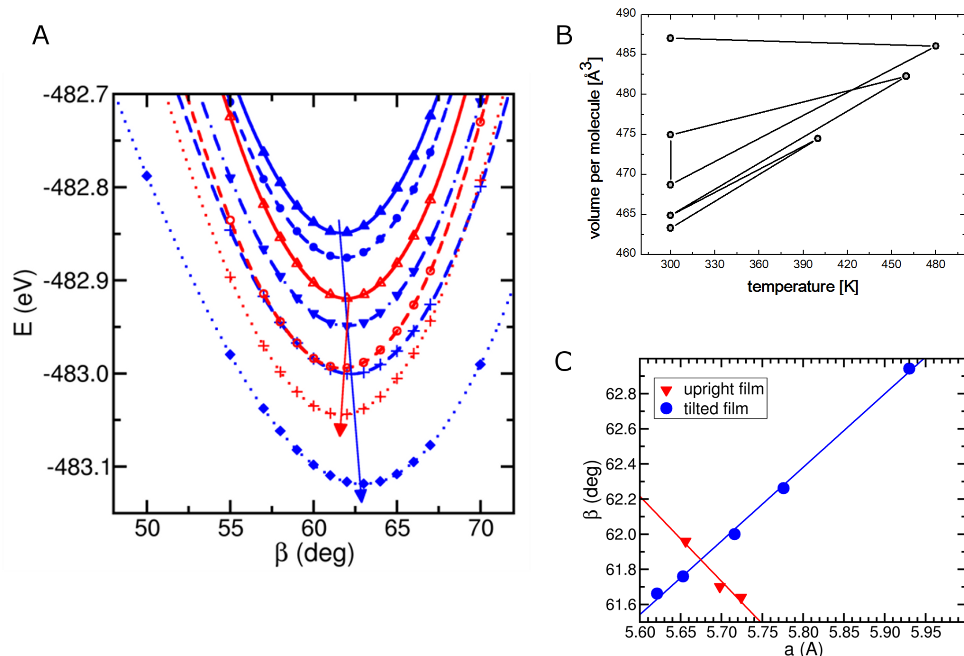

Figure 3.23.: Red corresponds to upright standing molecules, blue to tilted molecules. The energetic minimization curves of the DFT calculations are shown in part A. The volume per molecule calculated from the unit cell parameters is shown as a function of temperature in B. The opposite trends of the herringbone angle upon annealing as a function of increasing unit cell axis a (C) as also indicated by the arrows in part A of the figure.

3.5.2. Layer thickness

Beyond 520K there is no further information by grazing incidence x-ray diffraction since there is no structure left. Information in that temperature region is gained by x-ray reflectivity (figure 3.24). The thickness of the SAM is found to decrease only slightly up to a temperature of 620K. In that region the model applied at room

Table 3.4.: Unit cell parameters determined in the temperature dependent in-situ x-ray scattering experiments used for the DFT calculations for determination of the temperature dependent herringbone angle.

temperature [K]	$a[\mathring{A}]$	$b[\mathring{A}]$	tilt angle Θ [deg.]
300	5.6213	7.99	10.7526
400	5.65631	7.98882	0
300	5.65292	8.00917	12.06204
460	5.6983	8.06056	0
300	5.7755	8.05026	13.37497
300	5.7155	8.08128	14.88144
480	5.724	8.0869	0
300	5.92997	8.10816	15.27383

temperature interpreting the SAM by a two layer stack with clearly separated electron densities is valid. At 620K there is a knee in the thickness evolution (figure 3.24) where the thickness starts to drop dramatically. The decrease flattens out at a layer thickness of approximately $16\mathring{A}$ around 760K. At 880K the SAM desorps completely from the substrate and the XRR curve measured afterwards equals the measurements of pure substrates.

In the region between 620K and 880K the SAM is modeled by a single layer using a mean electron density between the two densities used initially for the two layer model. This is understood as an unordered state of the molecules on the substrate. It is assumed that at these temperatures already some molecules desorb, especially those that are not covalently bond to the substrate [14]. It can be speculated that when the space filling of the non covalently bond molecules is missing the remaining molecules have enough space to somehow fall over - this can however not be proven

by x-rays.

At 520K, the temperature where the crystal structure is lost no change in the XRR is measured.

Additionally the sample has been cooled from 760K to room temperature once to determine whether there is some further decrease of the layer thickness perhaps due to the beam intensity in combination with temperature but no change in layer thickness could be found while cooling the sample. Hence, changes in layer thickness can rather be addressed to the influence of temperature than to the time scale.

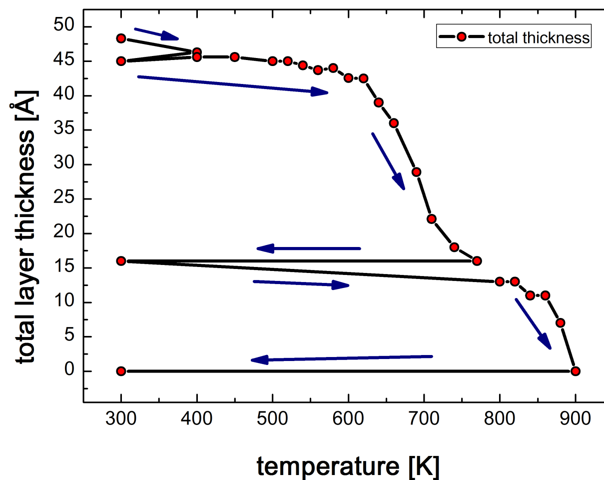

Figure 3.24.: The total layer thickness from XRR in-situ monitored during the heating process The arrows mark the evolution in time.

Figure 3.25 shows the measured XRR data at critical temperatures and the corresponding simulation data. In the upper curves there is a slight shift of the minima towards higher q_z visible that indicates the small decrease in layer thickness upon 620K. The roughness evolution does not show any significant features. It varies only around the initial value and can therefore be neglected.

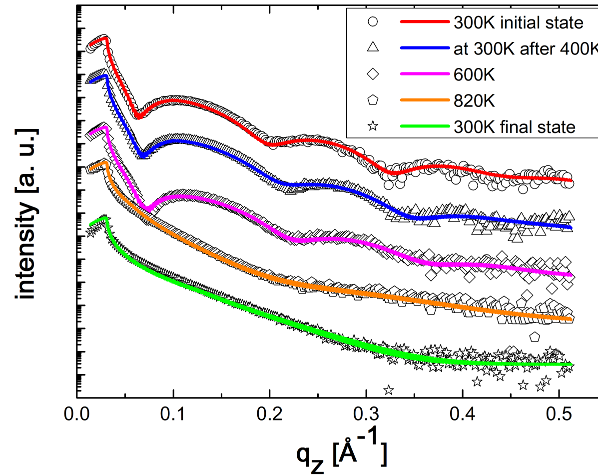

Figure 3.25.: X-ray reflectivity measurements (symbols) and their corresponding simulation (lines) of in-situ heating of a SAM at critical temperatures (curves shifted for clarity).

3.6. Crystal domains

Investigations using atomic force microscopy have already been presented. Data from Kelvin probe force microscopy has been published on this type of system revealing the pathways of the charge carriers within the channel of a SAMFET [17, 18] . Additional imaging techniques (e.g. TEM) have also been used - but in this section a transverse shear microscopy (TSM) study is presented. The measurements have been done in the scanning probe microscopy group of Christian Teichert at the University of Leoben.

3.6.1. Transverse shear microscopy - basic principles

There are several modes and techniques which can be applied using an AFM as for example topographical imaging in non-contact mode, tapping mode, or contact

mode. Phase imaging obtains information on the different elastic behavior of areas on the surface or friction force microscopy (FFM) determining the differences in friction of the tip on the surface which is sensitive to isotropic areas of different chemical composition. A rather unknown method is transverse shear microscopy (TSM) which gains information on anisotropy of a surface as for example domains of different molecular orientation [65, 66].
Trace and retrace information of the scan is subtracted and divided by 2 as shown in the scheme of figure 3.26. It is important that the cantilever is scanning along its long axis and not perpendicular to it like in FFM. The tip is scratching along the surface and bend at a certain angle for a specific crystal orientation. The working principle has been shown on pentacene thin films. One important factor for TSM is the force that is used for recording the data. Using the wrong force can i) destroy the sample or ii) show no domains where domains are present.

3.6.2. TSM on 5T-SAMs

Theoretically a smooth image without features is expected for a TSM scan of the pristine phase of fully upright standing molecules. Experimentally this can be found in the submonolayer topographical image of a pristine phase sample in figure 3.27 part E where no variation in the signal could be found by TSM.
For the phase of tilted molecules a distribution of domains is expected. Figure 3.27 shows a nice example of topography and TSM image of the same spot on a sample of tilted molecules. Part A is a topographical image that already shows some indication of boundaries between smooth areas. There are rims of about $0.5nm$ height visible. Part B shows is the corresponding TSM image where the domains are clearly visible. The domains show the same shape as the islands in the submonolayer state pointing out the island like layer formation.
Part D shows the same image as part B but as a guide for the eye black lines have been added to show clear grain boundaries (thick lines) and grain boundaries which have been seen on other images (using different forces) of the same spot

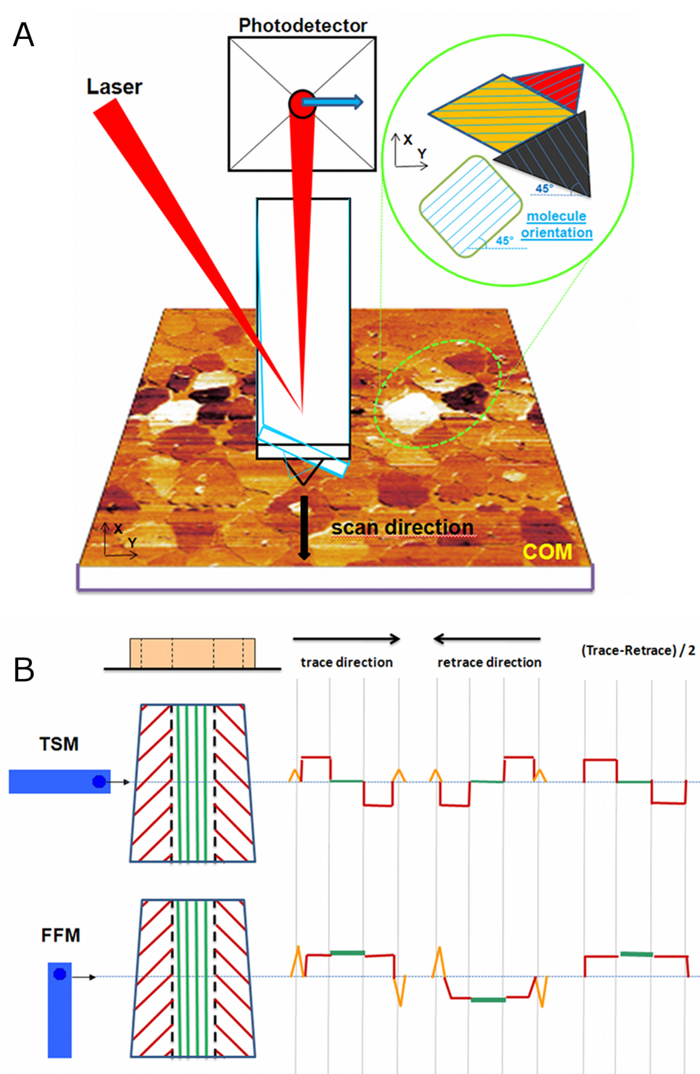

Figure 3.26.: A scheme of TSM showing the tilting of the cantilever when the molecular orientation changes while scanning along the cantilevers direction (A) as it has been shown in [65] for pentacene. The difference between TSM and FFM is the scan direction along the cantilever axis and perpendicular to it. The green and red lines (B) indicate areas of differently molecular orientation. In the FFM no changing signal can be detected as the chemical composition is equal, TSM detects the differently oriented areas.

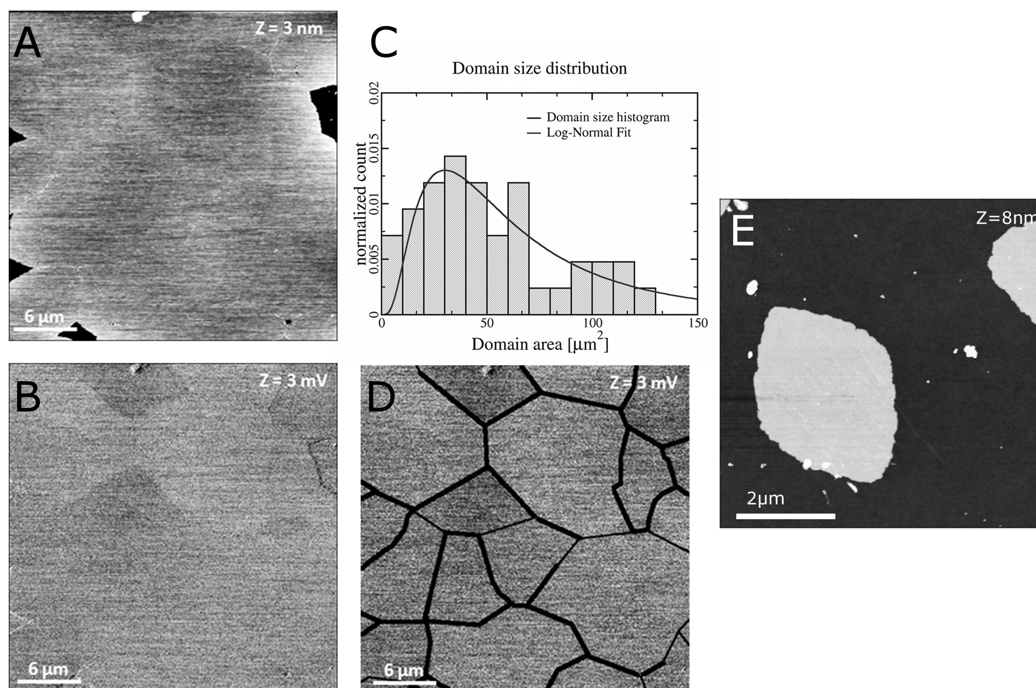

Figure 3.27.: Topography (A) and distribution of the domains (B, D) of one specific spot of a SAM with tilted molecules. Image D shows black lines for grain boundaries as a guide for the eye. Image C shows a histogram of the assigned domain sizes. E presents a topographic image of a pristine submonolayer island showing the same shape as the domains in the TSM images.

(thin lines).

The evaluation of the approximated domain sizes gives a size distribution as shown in figure 3.27 in part C. The size of the domains is on average $30\mu m^2$. The domain size seems to be independent from the annealing process because samples which have been annealed the same way (400K) sometimes may also show smaller domain sizes of around $10\mu m^2$. Hence the domain size is most likely determined during the layer formation process and temperatures during layer formation but not by post-layer-formation steps of temperature treatment as might be suggested. It is

suggested that the substrate and the surface purity defines the domain size of the quinquethiophene SAMs. Usually the domain size and device performance can be enhanced by proper temperature treatment - for the SAMFETs only the latter (an enhancement in the device performance) is noted.

3.7. Conclusions on Quinquethiophene SAMs

The submonolayers and monolayers of quinquethiophene self-assmbled molecules have been investigated concerning their structure and morphology. The approach of building a SAMFET has already been proven and published for this first system of long-range ordered SAMs on silicon dioxide. The studies presented here show the characterization of the layers themselves by x-ray techniques (grazing incidence in-plane x-ray diffraction, x-ray reflectivity) and microscopical techniques (atomic force microscopy, transverse shear force microscopy) and calculations based on these experimental results.

The annealing step at 400K in the device fabrication process has been found to switch the SAM from a pristine phase to a new one. The pristine phase consists of fully upright standing molecules whereas due to temperature treatment a layer of tilted molecules is found. The tilt of $\theta = (13 \pm 2)^\circ$ (average over all samples) is uniform towards the b-axis of the unit cell. The unit cell that has been calculated is only slightly larger than the one given in the literature for quinquethiophene which is attributed to the non-closed packing of the monolayer compared to bulk crystals. The packing of the molecules inside the unit cell is of herringbone type with a herringbone angle of $\beta = 63^\circ$ for the upright standing molecules and for the phase of tilted molecules an angle of $\beta = 60^\circ$ is found.

Further temperature treatment above 400K leads to an almost reversible expansion of the unit cell (approximately 10% irreversible contribution). At elevated temperatures only the phase of upright standing molecules is found. The tilt of the molecules after the heat treatment measured at room temperature is increasing

after higher temperature treatment. At 520K the crystallographic order is lost, which corresponds to 526K given for the bulk material of quinquethiophene. The layer thickness remains rather stable (only a small decrease is found due to heating) up to 620K. Above that temperature a large decrease in the layer thickness is found that ends up in complete layer desorption around 880K.
The SAMs are found to be stable under the x-ray beam on a laboratory system using a sealed tube as well as under the synchrotron beam. However the introduction of temperature during the x-ray irradiation yields a degradation of the monolayer. This topic and the stability of the monolayer and comparability of setups is treated in the appendix of this work. Molecules of passivated SAM molecules have been dissolved and drop cast on silicon oxide and show a similar structure as the SAMs. Further TSM, AFM and FFM investigations are also presented in the appendix.

4. Surface modification by inter-layers

The control of the device performance in organic thin film transistors can be achieved by thin inter-layers between the organic semiconductor and the gate dielectric [67, 68, 28]. This chapter shows the characterization of such a layer by x-ray reflectivity and atomic force microscopy. The evaluation of the changes in the device are still pending and done by a collaborating group.

4.1. The material

One approach for surface and device modification is the fabrication of self-assembled monolayers on the silicon oxide used as gate dielectric. A similar attempt to modify the surface and hence the interface properties has been shown by means of thin self-assembling films using a 7:3 ratio of 4- (2- (trichlorosilyl) ethyl) benzene-1-sulfonyl chloride (TSC) and its sulfonic acid counterpart (TSA) (referred to as T-SC/SA, compare figure 4.1) dissolved in dry toluene [69, 70, 71]. Due to the XRR thickness measurements the formation of a monolayer can be excluded.
The trichlorosilane anchoring group prevents the formation of a SAM and therefore the control of the layer thickness is a crucial factor if the device performance should be controlled by the interface or the thickness of the surface modification inter-layer.
The main steps in the device fabrication or more important the formation of the

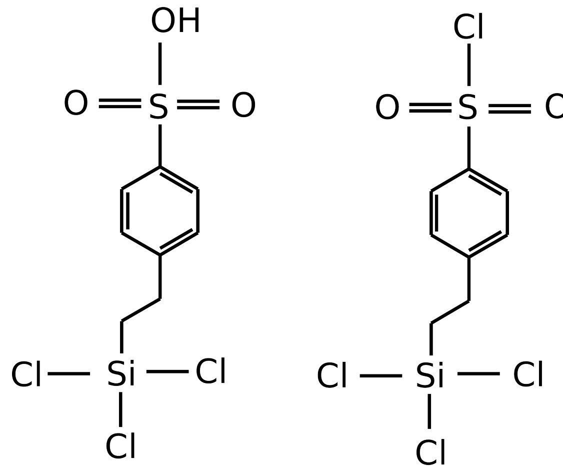

Figure 4.1.: The non bonded molecules of T-SA (left) and T-SC (right).

T-SC/SA layers are:

* dry cleaning under CO_2 gas stream
* O_2 - plasma etching of the silicon oxide surface to provide a hydrophilic surface offering a lot of hydroxyl groups for anchoring the silanes
* dry cleaning under CO_2 gas stream
* ultrasonic bath of the substrate in ultra pure water for 2 minutes
* transfer to argon atmosphere (glovebox)
* submersion of the substrate into a $0.05 vol\%$ solution of T-SC/SA for 16 hours
* transfer into pure toluene including a ultra sonic bath
* rinsing with toluene
* drying under CO_2 gas stream
* 30 minutes annealing under rough vacuum at 373K to enhance the cross-linking

4.2. Layer thickness and morphology

After this preparation the organic semiconductor (rr-P3HT, Pentacene,...) can be applied and bottom gate top-contact devices have been build. It has been found that the thickness of the inter-layer plays a crucial role and should be controllable. In this chapter a study on the control of the layer thickness and the most important influence on the layer thickness is provided. The threshold voltage in the device can be controlled by the inter-layer thickness which is important for sensor applications and in the step towards integrated circuits.
The attempt to generalize the findings of this study however failed. The thickness of the T-SC/SA layer strongly depends on two parameters.

* The type silicon oxide surface (the batch of wafers).
* The water content in the toluene.

The silicon oxide surface of different batches of thermally oxidized silicon wafers are not the same - even not after cleaning and O_2 - plasma etching. This has been found out during these investigations. Even though the two batches should have nominally been equal it has not been possible to reproduce the results from one batch on substrates of the other batch. This is however not promising for this type of layers.
The water content in the toluene however can rather easily be controlled. The use of dry toluene (controlled quality) is the basis. To define the amount of water in the solution the conditions in the argon glove box have to be stable. The water is added in form of water saturated toluene.
From XRR measurements it has been found that the thickness increases linearly with the amount of water added to $10ml$ of the solution as shown in figure 4.2 A. Figure 4.2 B shows the XRR measurements of series 2 and their corresponding fits. The minimum that is visible in the XRR curves shifts clearly to the left as the amount of water saturated toluene increases which corresponds to the thickening

Table 4.1.: Layer thickness of the modeled top layer d and rms surface roughness σ of the top layer of series 2 from 4.2.

amount of water sat. toluene	$10\mu l$	$20\mu l$	$30\mu l$	$40\mu l$
layer thickness d $[nm]$	0.7	1.04	1.34	2.1
rms roughness σ $[nm]$	0.4	0.5	0.5	0.5

of the self-assembling thin film. Fitted values are given in table 4.1. The fits have been done using a 2 layer model with a layer fixed thickness of $0.7nm$ and $0.2nm$ root mean square roughness directly at the substrate - interpreted as the first bonded molecules and a top layer that varies in thickness according to the amount of water saturated toluene. The mean electron density of this layer has been determined to be $\rho = 0.34\mathring{A}^{-3}$. The thin film on top has been calculated using a mean electron density of $\rho = 0.43\mathring{A}^{-3}$

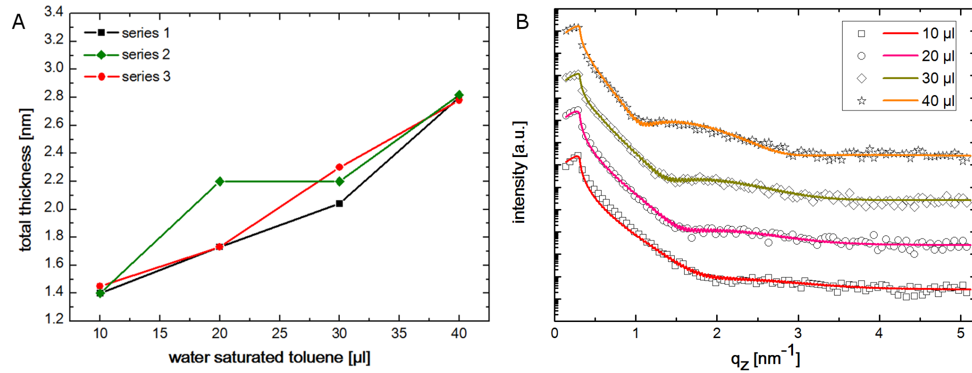

Figure 4.2.: Total layer thickness versus the content of water saturated toluene in the solution for threes sample series using the same substrates (A). XRR measurements (symbols) and corresponding calculated curves (lines) for series 2 (B). Curves are shifted for clarity.

The attempt to generalize this rule from one batch of silicon substrates to another

one however failed as figure 4.3 shows. The thickness found on substrates of the second batch is always larger than for the first batch. Nevertheless the tendency that a larger amount of water saturated toluene yields a thicker film of T-SC/SA is still present. An exception is noted at low amounts of water ($10\mu l$ of water saturated toluene added to $10ml$ of the solution) where the values are equal for both batches. This small amount of water seems to have little influence on the layer formation.
If there is interest to control the layer thickness for a device fabrication process the slope of the linear dependency has to be measured for each batch of substrates. Within one batch there is the possibility to rely on the linear dependence in the regime up to $40\mu l$ of water saturated toluene in the solution.

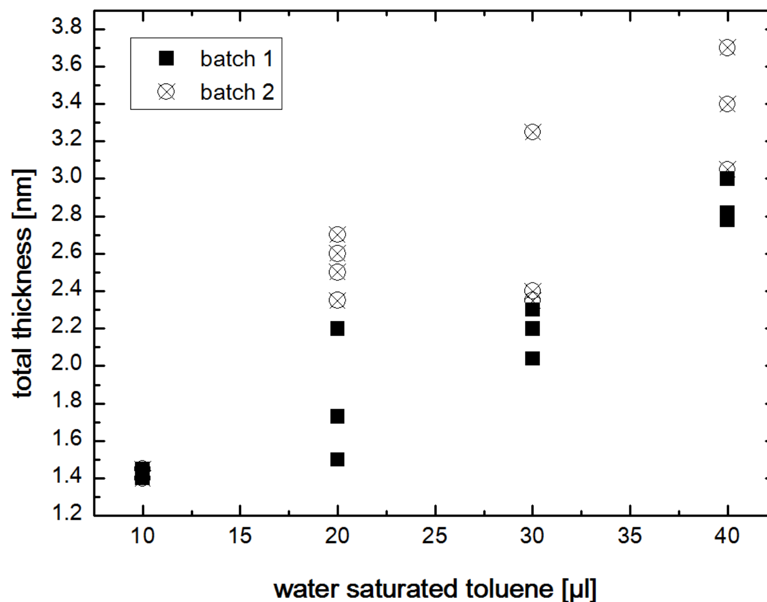

Figure 4.3.: The total layer thickness versus the content of water saturated toluene in $10ml$ solution for two different batches of silicon oxide substrates. The layers prepared on batch number two tend to larger thickness. Batch one full symbols, batch two open symbols.

Recent studies showed a linear correlation between layer thickness and surface

roughness. This has not been followed extensively in earlier studies but as seen in figure 4.4 the surface roughness increases with layer thickness. This has been reported earlier for layers of OTS [20] for example as already mentioned in chapter 2. Larger layer thickness corresponds to a larger amount of water and hence increased surface rougness. The error bars in the figure are based on the data evaluation using an alternative x-ray reflectivity fitting tool, GenX [72]. The genetic algorithm used in this package is more sensitive so roughness parameters and could hence provide these values.

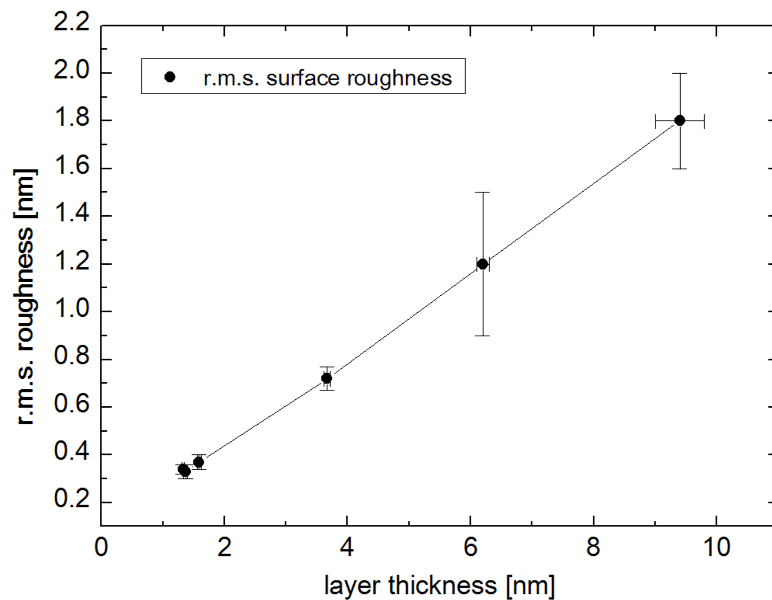

Figure 4.4.: The total layer thickness versus the content of water saturated toluene in the solution for 2 different batches of silicon oxide substrates. The layers prepared on batch number 2 tend to larger thickness.

The impact of the layer thickness on the device performance is still under investigation. The effect is found mostly in a shift of the threshold voltage. As benchmark material for organic electronics pentacene has been used as organic semiconductor. The morphology of the pentacene is not changed due to the inter-layer of T-SC/SA as shown by AFM (figure 4.5). The morphology found for pentacene

on the different thicknesses of the inter-layer looks like the terrace morphology usually found for pentacene on silicon oxide in the literature [73].
The morphology of the T-SC/SA seems to be slightly thickness dependent and hence changes in the electronic properties can rather be assigned to changes of the interface morphology or to the special properties of the inter-layer than to the pentacene packing. The covalently bonded T-SC/SA layer is expected to form a space charge layer [28, 30] that increases the threshold voltage in the OTFT with larger layer thickness. The tendency however has been seen but not yet been proven by the co-workers.
As can be seen in the left row of the AFM images in figure 4.5 there is some precipitation on the surface due to the preparation from solution. This is not desirable in devices and should be a point of improvement.

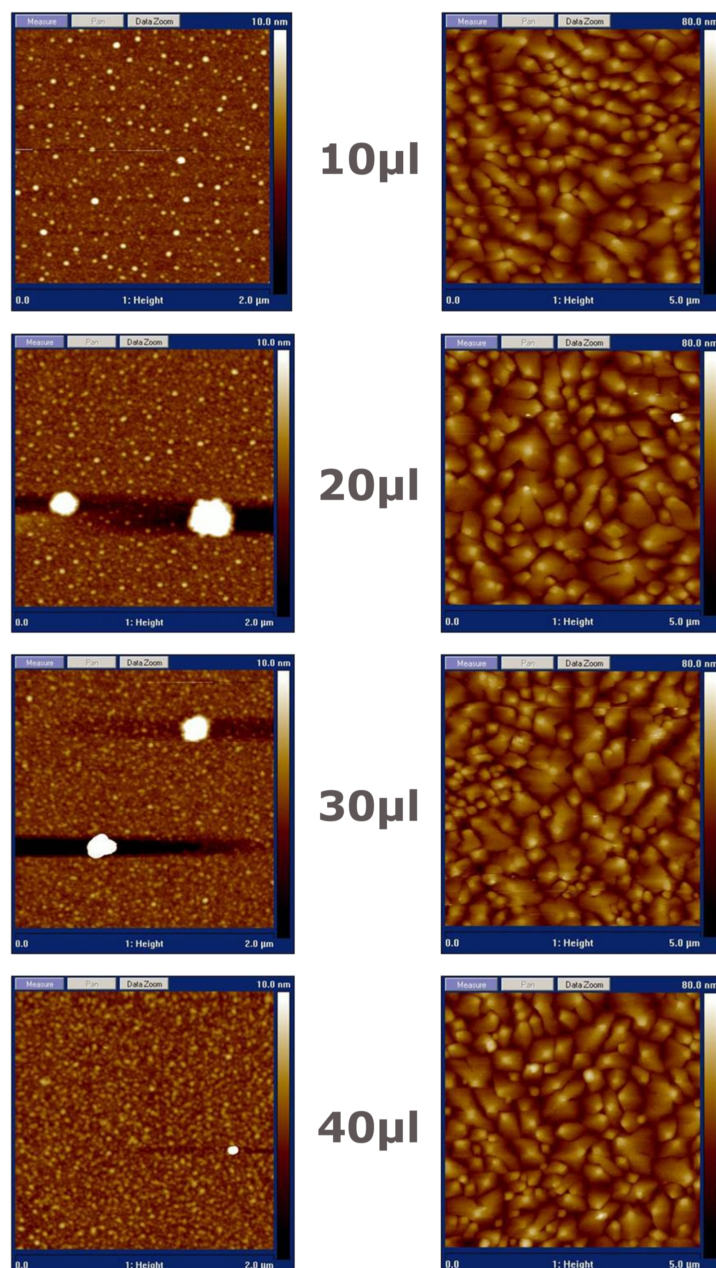

Figure 4.5.: AFM morphology images of T-SC/SA layers (left) and the corresponding images of the pentacene deposited on the same layers (right) for different amounts of water saturated toluene added to 10*ml* dry toluene containing the molecules.

5. A combined x-ray, ellipsometry and atomic force microscopy study on thin parylene-C films

This chapter shows a study on the advantages of a combinational approach to thin film characterization by several methods. The advantages of combining x-ray reflectivity and ellipsometry are described in detail. The material used for this study is not the central point. The focus in this section is clearly on the techniques. Atomic force microscopy is often a stand-alone technique for roughness and topology characterization but the combination with XRR results gives a more powerful tool for the investigation of any thin film system. The study has been published as proceeding [74] of the XTOP 2008 conference held in Linz, Austria. A copy of the paper head presenting all contributing people and the abstract is given in figure 6.1

5.1. Introduction

In organic electronics high performance devices are build from several layers of different materials. To enhance the devices performance and improve the fabrication process structural and morphological characterisation of layers and interfaces is required. For opto-electronic devices the important information is the film thickness, refractive index and the resulting dielectric constant for both optical and

Phys. Status Solidi A **206**, No. 8, 1727–1730 (2009) / **DOI** 10.1002/pssa.200881616

A combined X-ray, ellipsometry and atomic force microscopy study on thin parylene-C films

Heinz-Georg Flesch[*,1], Oliver Werzer[1], Martin Weis[2], Ján Jakabovič[3], Jaroslav Kováč[3,4], Daniel Haško[4], Georg Jakopič[5], Harry J. Wondergem[6], and Roland Resel[1]

[1] Institute of Solid State Physics, Graz University of Technology, Petersgasse 16, 8010 Graz, Austria
[2] Department of Physics, Slovak University of Technology, Ilkovičova 3, 812 19 Bratislava, Slovakia
[3] Department of Microelectronics, Slovak University of Technology, Ilkovičova 3, 812 19 Bratislava, Slovakia
[4] International Laser Center, Ilkovičova 3, 812 19 Bratislava, Slovakia
[5] Institute of Nanostructured Materials and Photonics, Joanneum Research, Franz-Pichler-Strasse 30, 8160 Weiz, Austria
[6] Philips Research Laboratories, High Tech Campus 4, 5656 AE Eindhoven, The Netherlands

Received 17 September 2008, revised 23 March 2009, accepted 7 April 2009
Published online 23 June 2009

PACS 61.05.cm, 68.35.bm, 68.35.Ct, 68.37.Ps, 68.47.Mn

[*] Corresponding author: e-mail heinz-georg.flesch@tugraz.at, Phone: +43-316-873-8477, Fax: +43-316-873-8466

Parylene-C thin films in a thickness range from 7 to 35 nm are deposited on silicon oxide and investigated for their structural and morphological properties by different methods. It is shown that spectroscopic ellipsometry (SE) is a powerful tool to obtain spatially resolved information on the homogeneity of thin films revealing relative changes in layer thickness and in the refractive index. However, the results can be considerably improved in combination with X-ray reflectivity (XRR) which provides highly accurate results on layer thickness. The layer thickness from XRR is used as a fixed input value for the evaluation of the ellipsometry data which reveals a layer thickness dependence of the refractive index in the thin film regime. The interface roughness is determined from XRR as well as the surface rms roughness which can be compared to the roughness found by atomic force microscopy (AFM) which varies between 0.5 and 2.0 nm. Both results for the roughness show excellent agreement. Additionally, a correlation of the roughness and the deposition rate is found.

© 2009 WILEY-VCH Verlag GmbH & Co. KGaA, Weinheim

Figure 5.1.: Copy of the head of the publication.

electrical film properties. Also the organic thin film interface has strong influence on the device charge transport properties.

Several methods are available for thin film analysis, but they are rarely applied with their full power because they are commonly used as stand-alone techniques. An approach of single layer characterisation (which can in principle also be applied to multilayer structures) is shown in this work by combining x-ray reflectivity (XRR), spectroscopic ellipsometry (SE), fixed angle single wavelength ellipsometry and atomic force microscopy (AFM).

From spectroscopic ellipsometry it is possible to determine the layer thickness or at least variations in the film thickness and the refractive index and hence the dielectric function of a thin film in the UV-VIS-IR region. However both layer thickness and refractive index tend to correlate heavily especially in the thin film regime [75]. As both parameters of interest are not measured directly but fitted, the results are not unambigous for unknown layers or materials.

Reduction of the free fitting parameters during the evaluation of ellipsometry data can be achieved by determining the layer thickness in advance and using it as an input parameter. X-ray reflectivity is used as one of the most accurate techniques for thin film thickness determination. Besides the layer thickness additional information on the electron density profile perpendicular to the surface as well as the surface and interface roughness can be extracted from XRR measurements. The XRR evaluation of the surface topology can then be compared to atomic force microscopy height images which tops of the characterisation of the thin film.

The complementary application of the methods on a well known and defined material as parylene-C is used as an example for a single thin film system. The thin films of parylene-C can be deposited very reproducible and are therefore ideal candidates for the presentation of a combined approach to thin film characterisation. Applications of parylene-C layers in electronic devices as dielectric layers [76] or as coating materials [77] can be found elsewhere and are not topic of this contribution.

Table 5.1.: Nominal layer thickness and deposition rate as monitored by the quartz micro balance at the sample preparation.

Sample	nominal thickness [nm]	Deposition rate [nm/s]
1	9.9	0.011
2	20.1	0.041
3	47.3	0.030
4	47.8	0.084

5.2. Experimental Methods

All measurements have been performed at room temperature and atmospheric pressure.

5.2.1. Sample preparation

The polypara-chloroxylylene (parylene-C) films have been prepared using chemical vapour deposition (CVD) starting from the comercially available dimer dipara-chloroxylylene. After sublimation the dimer has been decomposed at $650°C$ and deposited at room temperature as the stable polymer on the substrate. The growth has been monitored by a quartz micro balance which provides a nominal layer thickness and a deposition rate as shown in table 5.1.
As substrate silicon wafers with a thermally grown oxide layer of 110nm have been used after cleaning with acetone and etching in an oxygen plasma.

5.2.2. Specular x-ray reflectivity

The x-ray reflectivity (XRR) measurements have been performed on a Bruker D8 Discover diffractometer set up in Bragg-Brentano configuration with a copper

sealed tube as source of radiation. Primary and secondary side Soller slits are used as well as a secondary side graphite monochromator. The primary side slit was set to 0.05mm and the secondary and receiving slits were set to 0.1mm for all measurements. There is an automatic absorber used in front of the secondary slit to protect the scintillation counter.
The experimental XRR data have been simulated using the software package WinGIXA which provides the possibility to fit the layer thickness and electron density profile using Parratt's recursive formalism [47] and the surface as well as interface roughness of the samples with the Nevot and Croce approach [48]. The geometrical parameters of the experimental setup and the parameters of the substrate have been simulated separately in advance and were kept fixed during the simulation of the parylene-C films.

5.2.3. Ellipsometry

Ellipsometry has been performed on two different experimental setups. First a single wavelength and fixed angle setup has been used. A Sentech SE400 ellipsometer has been used at constant incident angle of 70° and at a wavelength of $\lambda = 632.8$ nm. These measurements provided information on the homogeneity of the layer thickness over the sample area. A more detailed analysis using spectrosopic ellipsometry (SE) has been performed on a J. A. Woolam VASE ellipsometer with auto retarder and rotating analyzer setup at incident anlges between 65° and 75° . The data evaluation has been carried out using the manufacturers software package WVASE32. The measurements were performed in the spectral range from 300nm to 1300nm wavelength.
For fitting of the real part of the refractive index $n(\lambda)$ of the organic top layer a Cauchy model [78] has been assumed; the imaginary part has been found to be negligible.

$$n(\lambda) = A + \frac{B}{\lambda^2} + \frac{C}{\lambda^4} \tag{5.1}$$

λ is the wavelength of radiation in micrometers and A, B and C are the Cauchy coefficients whereas coefficient C has been found reasonable to neglect for parylene-C as has been reported previously by Callahan et al [79]. For the substrate and the silicon oxide literature data has been used as listed in the software database and showed nice matching with the measured data.

5.2.4. Atomic force microscopy

The surface topography has been investigated by high resolution atomic force microscopy (AFM) using a AFM microscope Solver 947-PRO manufactured by NT-MDT company operated in tapping mode. The surface rms-roughness could be extracted from the height images of $10\mu m$ x $10\mu m$.

5.3. Results and Discussion

Four selected samples with different layer thicknesses have been picked out as representative set for investigations in the thin film regime below 40nm.

5.3.1. Film thickness variation

The thin films have been investigated after preparation by ellipsometry on various spots across the sample (see figure 5.2). The absolute value of the layer thickness could not be determined as the refractive index was not known in the required accuracy.
Therefore all samples have been investigated using a literature value of n=1.639 at the specific wavelength as published previously by Khabari et al. [80] that allows a qualitative comparison. This method proves the homogeneity of the film and shows that the film thickness on the sample has some gradient which results from the preparation process but over the investigated area of $20mm^2$ the film thickness variation is small (< 0.1nm).

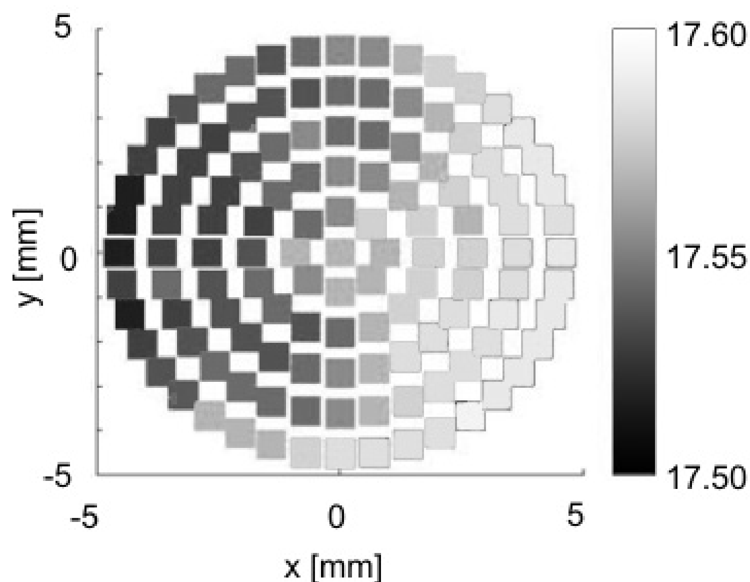

Figure 5.2.: Ellipsometry measurements on different spots on sample 2. The fitting procedure was performed using a refractive index of 1.639 according to Khabari et al. [80] to investigate the film thickness distribution.

5.3.2. Precise film thickness

For the determination of more precise values of the parylene-C film thickness XRR measurements were performed. In XRR the layer thickness can be determined from the interference pattern which is known as Kiessig fringes [81]. The spacing of the minima and maxima in the interference pattern is a direct measure for the film thickness [82] which can be evaluated without further information about the material properties, thus it is one of the most accurate methods for evaluating thin film thicknesses.

The measurements are shown in figure 5.3 and show very pronounced maxima and minima. The fast oscillating signal ($\Delta q_z = 0.01 \AA^{-1}$) is caused by the silicon oxide;

the wide oscillations ($\Delta q_z = 0.06\mathring{A}^{-1}$ for sample 3 e. g.) come from interference within the organic top layer of major interest. Their pronounced presence indicates small roughness and high homogeneity of the layers as already shown by the fixed angle single wavelength ellipsometry measurements. The thickness of the silicon oxide was found to be 110nm. For the film thicknesses of the organic material the values shown in table 5.2 could be extracted.

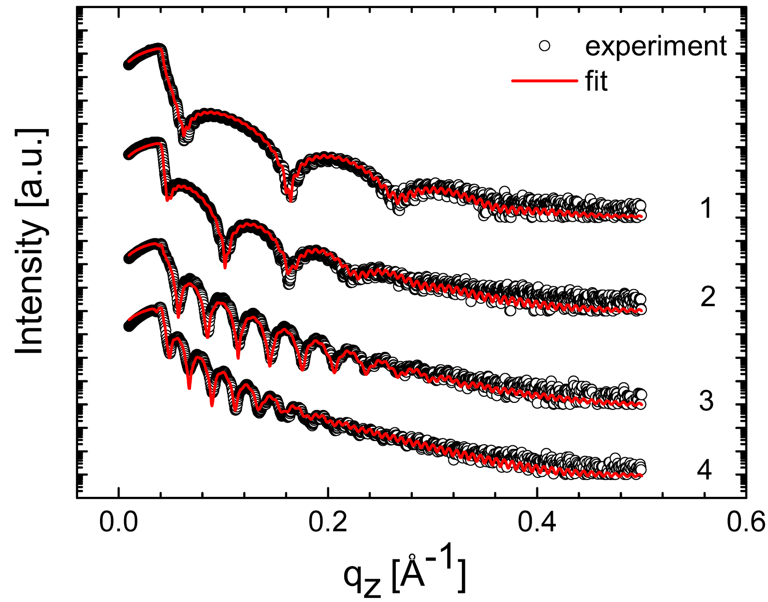

Figure 5.3.: Specular x-ray reflectivity measurements and corresponding fits of parylene-C films with different film thickness (range from 7.9nm to 35nm). The curves are shifted for clarity.

5.3.3. Optical constants

The comparison of the layer thicknesses determined by fixed angle single wavelength ellipsometry shows a clear misfit between the ellipsometry data and the XRR measurements. The tendency however of the layer thicknesses from these two methods shows good agreement as there seems to be only some offset between the XRR layer thickness and the ellipsometry data in figure 5.4. An evaluation of the ellipsometry data without detailed knowledge about the material can be misleading as the refractive index tends to correlate strongly with the layer thickness, especially in the thin film regime [75].

One way out of this problem is a calibration of the ellipsometer using any other method for the determination of the film thickness. The nominal thickness given by the quartz micro balance during the sample preparation would be misleading as well as it needs a calibration as well. Therefore the very precise method of XRR is used. Keeping the layer thickness fixed at the XRR values allows the fitting of the refractive index by the Cauchy relation. The values are found in table 5.2 and figure 5.5 where additionally the literature values are given [79]. There seems to be a tendency for decreasing A and increasing B with decreasing film thickness. The literature data have been found in thicker films and are therefore not exactly matching the values found here in the thin film regime.

5.3.4. Surface roughness

The surface roughness of the samples has been determined using an AFM. The evaluation of the XRR data also provides this information and the results are shown in figure 5.6. The roughnesses determined by XRR are all larger than those determined by AFM but both show the same tendency however. The reason for the misfit seems to be of systematic nature and can be related to the experimental setup of the AFM. AFM underestimates the roughness because of a rather large tip size compared to the small roughness oscillations of the surface. This yields

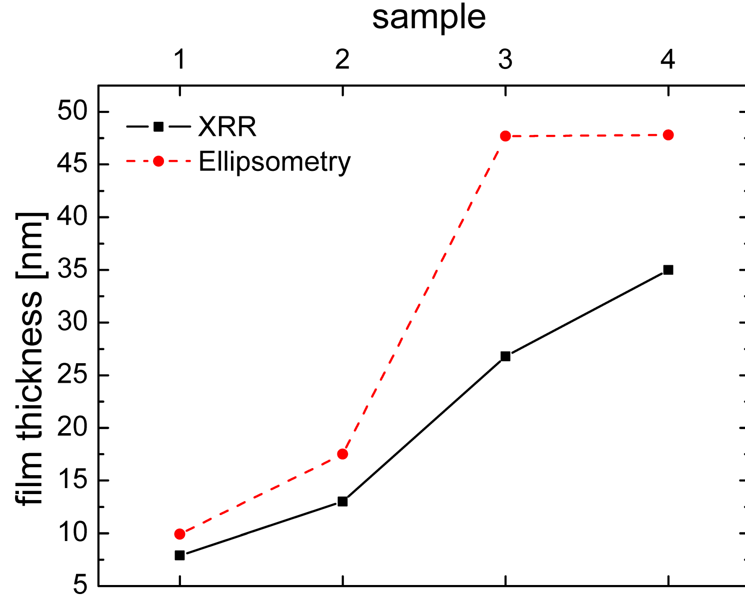

Figure 5.4.: Thickness of different parylene-C thin films as determined by specular x-ray reflectivity and fixed angle single wavelength ellipsometry using a refractive index of 1.639 according to Khabari et al. [80] .

Table 5.2.: Layer thickness determined by x-ray reflectivity and Cauchy parameters (A, B) determined by fitting the ellipsometry data using fixed layer thicknesses extracted from x-ray reflectivity.

Sample	d_{XRR} [nm]	A	B [nm^2]
1	7.9	1.5633	0.0263
2	12.5	1.5856	0.0226
3	26.8	1.6051	0.0184
4	35.0	1.6022	0.0180

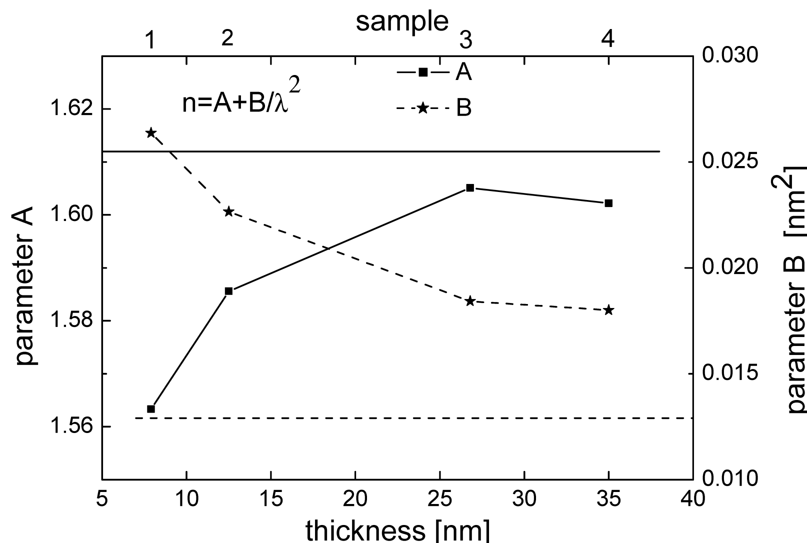

Figure 5.5.: Parameters for the Cauchy relation determined by spectroscopic ellipsometry using the XRR layer thickness as fixed input parameter. Parameter A is shown on the left scale, the literature value [79] is marked by the solid horizontal line. The right scale and the dashed line represent the corresponding values for parameter B. Parameter C did not improve the results and has been set to 0 as also proposed by Callahan et al. [79]. n is the refractive index determined by the Cauchy relation.

too small values for the surface roughness.

The surface roughness seems to be correlated to the deposition rate during the film preparation (see figure 5.6) as it is largest for sample 4 and decreases for sample 3 and 1, whereas the roughness for sample 2 is higher which allows the conclusion that the surface roughness is correlated stronger to the deposition rate than to the film thickness. The modelling of a surface or interface roughness in the ellipsometry data by the introduction of an effective medium top layer did not improve the results and has been discarded after several attempts.

According to the AFM images the film is free of pinholes larger than the AFM tip size which is very appreciable for electronic applications of parylene-C.

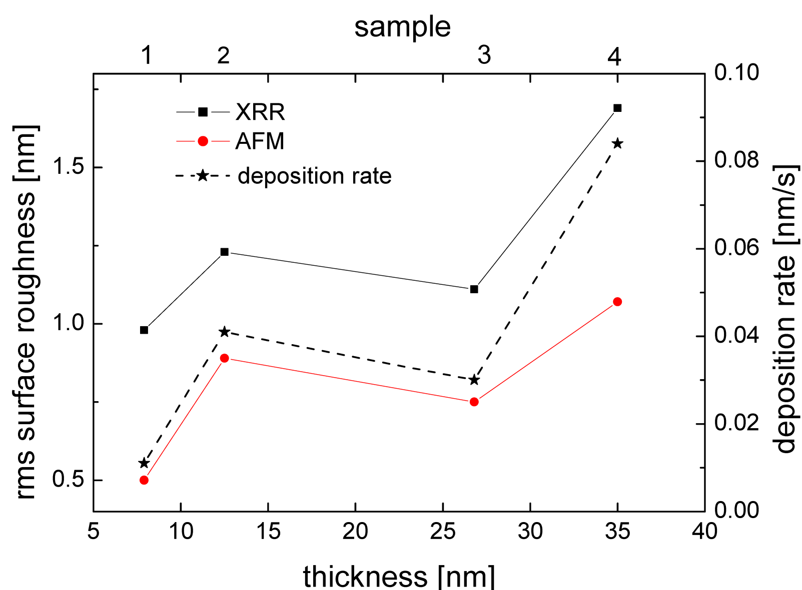

Figure 5.6.: Comparison of the surface rms roughness parameter determined by atomic force microscopy and by the simulations of the specular x-ray reflectivity data. The deposition rate during the film preparation is shown by thy dashed line.

5.4. Conclusions

For optimal characterisation of morphology and structure of thin films a combined investigation approach is recommended. X-ray reflectivity provides the most accurate results on the layer thickness and information on the layer homogeneity by the electron density profile. Relative changes in roughness can be determined whereas absolute surface roughness values should be evaluated also by atomic force microscopy as complementary method to evaluate the surface structure. The

disadvantages of XRR is that the illuminated area should be rather smooth and homogeneous and the experimental effort is relatively large and time consuming. Single wavelength ellipsometry however profits from fast data acquisition and can therefore also be used as quality control in high throughput production processes to control the layer thickness or layer homogeneity. As more precise method for film thickness dependent determination of the refractive index of any layer spectroscopic ellipsometry is recommended. However any ellipsometry configuration should be calibrated using an alternative method for film thickness determination such as XRR to avoid unphysical results due to highly correlated parameters as the refractive index and layer thickness are.

5.5. Material

The thin films of parylene-C have been prepared in Bratislava by chemical vapor deposition. Figure 5.7 in the upper left corner shows the structure of the deposited material. The precursor dimer is sublimated and then heated to 950K. It decomposes to the monomer para-xylylene and the film is then deposited at room temperature by cold deposition of the polymer poly(para-xylylene) called parylene-C. The advantage of this gaseous deposition is the ability to reach sharp tips and hidden corners as well as edges. Monitored by a quartz microblance this thin film preparation method is very reproducible and makes extremely homogeneous films as demonstrated by fixed angle single wavelength ellipsometry. Figure 5.7 shows the deposition chamber and the main steps of the thin film production process in the lower part and from right to left the route from the dimer to the polymer.

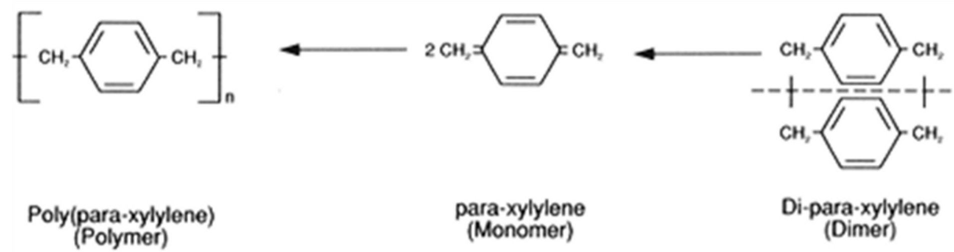

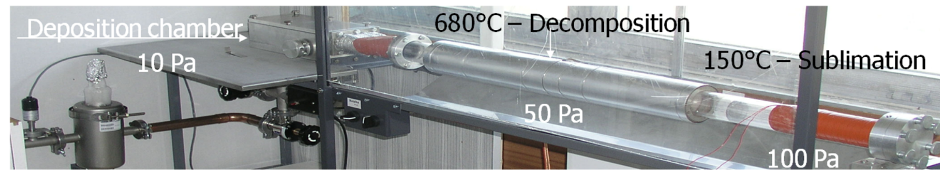

Figure 5.7.: The route from the precursor dimer to the parylene-C polymer through the chamber and temperatures and as structure formula in the upper section.

5.6. Spectroscopic Ellipsometry

Spectroscopic Ellipsometry [83] is another tool for thin film characterization like x-ray reflectivity is. The fundamentals of both techniques are not far from each other but the fundamental properties that are utilized lead to quite different applications and a meaningful combination of both has been reported in the literature [84, 74, 85, 86]. Both techniques use interference of an transversal electromagnetic wave within a layer of a homogeneous material. The difference is the wavelength and the properties of the light within a specific wavelength regime. The basics of ellipsometry will be explained in the next few pages and differences to XRR as well as overlaps will be pointed out. Equally to x-ray reflectivity, ellipsometry is sometimes considered to be more like an art than science because it is rather easy to measure but most of the time hard to interpret; but in fact everything is based on some equations and physical principles. This section summarizes the basic principles of ellipsometry based on the books of Azzam [87] and Tompkins [78].

5.6.1. Polarized light

Generally light is composed by a superposition of arbitrarily polarized parts of light which are statistically distributed. Light is called polarized if the electric field vector **E** observes certain rules concerning its direction along the propagation direction (z-direction) [87]. Three types are distinguished:

* linear polarized light: the electric field vector **E** stays within one plane and changes solely its sign and absolute value (fixed amplitude). The projection of the tip of the vector to the xy-plane describes a line. ($\Delta = 0$ or $\Delta = \pi$)

* circular polarization: the electric field vector **E** moves with constant angular velocity and absolute value around the wave vector. The projection of the tip of the vector to the xy-plane moves on a circle. ($\Delta = \pm\pi/2$ or $\psi = \pi/4$)

* elliptic polarization: the electric field vector **E** rotates around the wave vector and changes its absolute value periodically. The projection of the tip of the vector to the xy-plane shows an ellipsis.

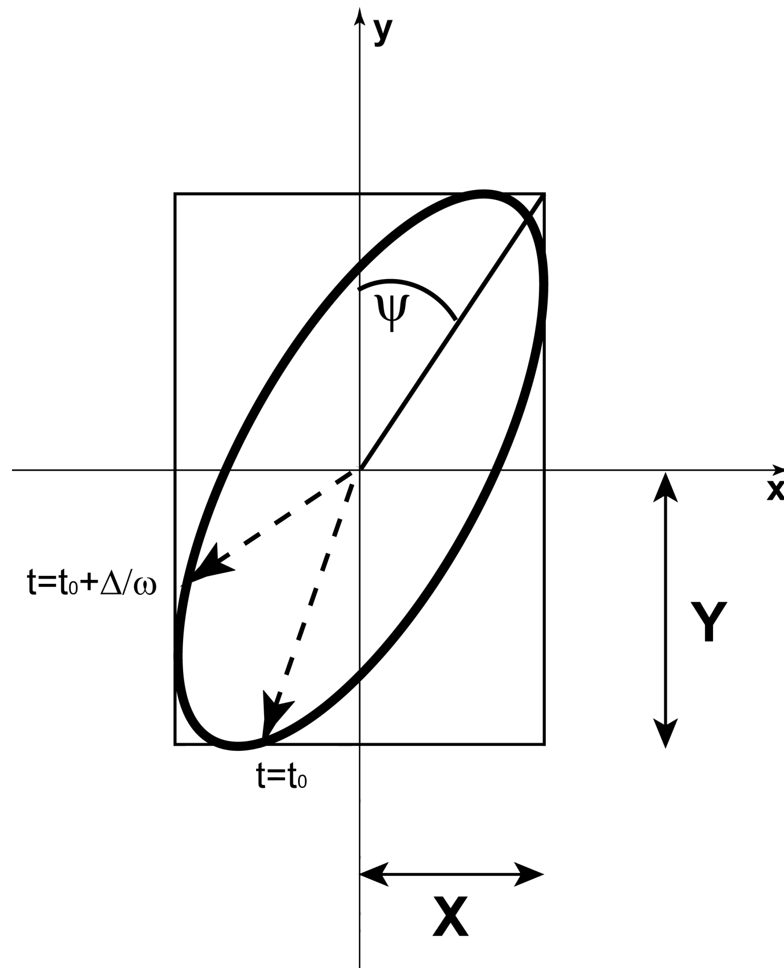

Figure 5.8.: Polarization ellipse of elliptic polarized light projected to the xy-plane. The wave vector points out of the drawing plane. The electric field vector moves clockwise on the ellipse. The ploarization state is described by Δ and ψ.

Elliptic polarization is the most general case which can be described as a superposition of the other two possibilities. Polarization can be described by three

quantities. The xy-plane mentioned above is the plane to which the wave vector is orthogonal. The first two quantities are the projection of the field vector to the this plane denoted by X and Y. For ellipsometry this is reduced to the relative amplitude $\tan\psi = X/Y$ (range: $0 \leq \tan\psi \leq \pi/2$). The third quantity is the relative phase Δ (takes values: $-\pi \leq \Delta \leq +\pi$) between two field vectors after a time step t. For positive values this is called clockwise or right-handed polarization (figure 5.8), correspondingly for negative values it is called counter-clockwise or left-handed polarization. Hence the electric field of the elliptic polarization at the time t in the plane $z = 0$ can be described by

$$\mathbf{E}(\mathbf{t}) = \begin{pmatrix} E_x(t) \\ E_y(t) \end{pmatrix} = \Re\left\{ \begin{pmatrix} Xe^{i\Delta} \\ Y \end{pmatrix} \mathbf{e}^{\mathbf{i}\omega(\mathbf{t}-\mathbf{t_0})} \right\} \tag{5.2}$$

Introducing the relative phase, and the relative amplitude this leads to the Jones vector for elliptic polarized light

$$\begin{pmatrix} \sin\psi e^{i\Delta} \\ \cos\psi \end{pmatrix} \tag{5.3}$$

This is a description of the polarization state by two real angles. These two angles are called the *ellipsometric quantities*.

5.6.2. Experimental setup

For the experiment you need in principle a setup where you can produce light of the desired wavelength (from IR to UV), a detector for that light and a goniometer to move light source and detector in specular condition - same as for XRR. Before and after your sample you mount a polarizer into the beam path to polarize the light and analyze the polarization after reflection from the sample (or after passing through the sample if sample and experimental setup allow a measurement in transmission mode). That is the basic setup for an experiment. For the x-ray

reflectivity one can neglect polarization but with ellipsometry this is the important quantity! A schematic view o of an ellipsometry setup is given in figure 5.9.

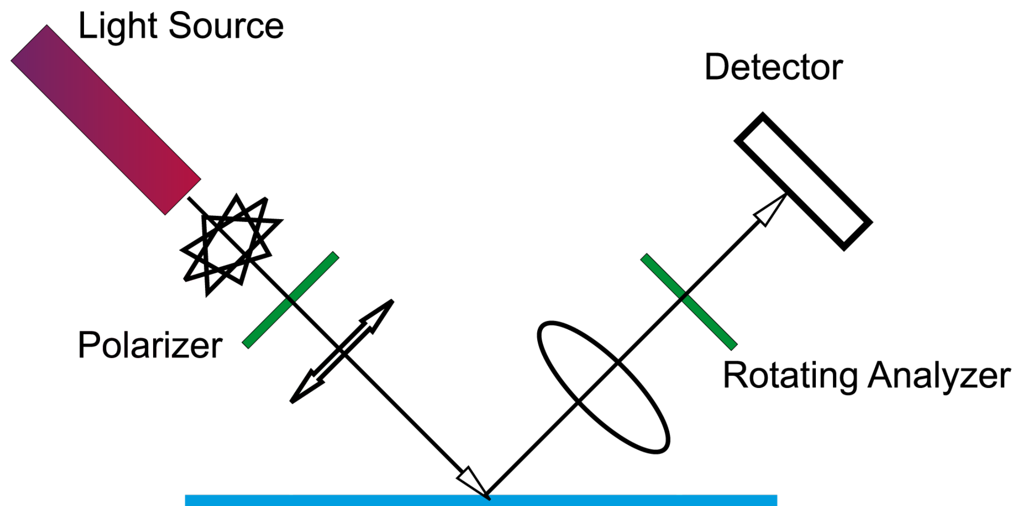

Figure 5.9.: Schematic view of the basic components of an ellipsometer.

Performing the experiment itself is divided into several steps.

* First of all the sample has to be aligned to be absolutely flat on the sample holder (same for XRR). This is achieved when the light is directly reflected into the light source again at normal incidence.

* Choose the wavelength range which depends on the device one uses and on the system one investigates.

* Choose under which angles light should be shining on the sample (same for XRR - but the range for XRR is usually located at very shallow angles).

* Choose how many different polarization states should be recorded at one angle.

There are two distinct ways to perform the experiment. One can scan the whole angular range at some selected wavelength and the more common one to scan the

whole spectrum at under some selected incidence angles. Bot types of measurements give different information. The first one gives better resolution and information on the layer thickness, the experiment is very similar to XRR. The second technique gives the thickness as well but might be misleading in tricky cases. This method is more useful if the optical properties (absorption and refraction index) are points of interest.
The detector of course does neither detect ψ nor Δ but the complex ratio ρ is connected to the ellipsometric quantities via the Fresnel reflection coefficients for parallel r_p and perpendicular r_s polarized light via:

$$\rho = \frac{r_p}{r_s} = \tan\psi \, e^{i\Delta} \tag{5.4}$$

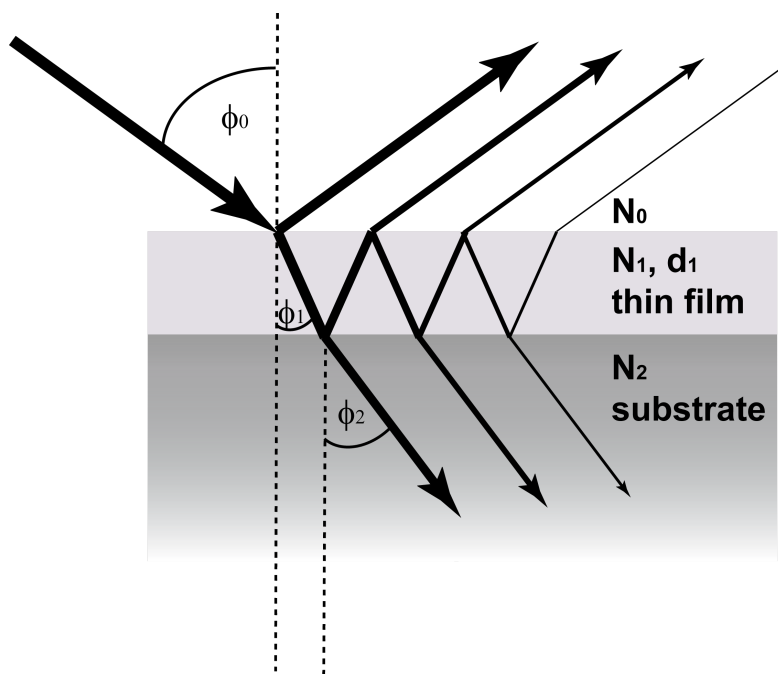

Figure 5.10.: One layer on a substrate model with light being multiple reflected at the interfaces 0-1 and 1-2.

For an interface between two layers (subscript 0 and 1, with distinct refractive

index) the reflection coefficients are connected to the complex refraction index $N = n - ik$ by:

$$r_{01p} = \frac{N_1 \cos\phi_0 - N_0 \cos\phi_1}{N_1 \cos\phi_0 + N_0 \cos\phi_1} \tag{5.5}$$

$$r_{01s} = \frac{N_0 \cos\phi_0 - N_1 \cos\phi_1}{N_0 \cos\phi_0 + N_1 \cos\phi_1} \tag{5.6}$$

Shifting the indices one gets the equivalent for the interface between layer 1 and 2. Evolution of that equation to a system with more than one interface, e. g. two interfaces (one-layer model) the equations for the total reflection R using the phase shift for interfering rays of light β reads:

$$R_p = \frac{r_{01p} + r_{12p\ e^{-2i\beta}}}{1 + r_{01p} r_{12p\ e^{-2i\beta}}} \tag{5.7}$$

$$R_s = \frac{r_{01s} + r_{12s\ e^{-2i\beta}}}{1 + r_{01s} r_{12s\ e^{-2i\beta}}} \tag{5.8}$$

$$\beta = 2\pi \frac{d_1}{\lambda} \sqrt{N_1^2 - N_0^2 \sin^2\phi_0} \tag{5.9}$$

d_1 is the desired layer thickness of layer one (see figure 5.10) and λ is the wavelength that is used. This formalism can recursively be extended to an arbitrary number of layers. The important point in these equations is that without knowledge of layer thickness or refractive index it is easy to fail in data evaluation. In this work the approach has been to use the layer thickness determined by x-ray reflectivity as an input parameter set for the ellipsometry data evaluation. This leads to better accuracy in the determination of the complex refractive index of the material under investigation. It has been shown that the refractive index is correlated to the film thickness in the thin film regime. Therefore tabulated values should be used with caution only. In that case the simplest model, the Cauchy model for the refractive

index can be used (which is frequently cut after at $N = 1$ or $N = 2$).

$$n(\lambda) = B_0 + \sum_{j=0}^{N} \frac{B_j}{\lambda^{2j}} \tag{5.10}$$

5.6.3. Data evaluation - Constructing the most physical model

An ellipsometer is a powerful tool and can tell you a lot of things about your sample and system, but one should always be suspicious when everything comes out of a single measurement. It's important to collect as much knowledge on the system as possible in advance. Some important parameters might be:

* substrate information, if available a measurement of a clean substrate should be done
* substrate roughness
* number of layers disposed on the substrate
* sharp or smooth interfaces
* interpenetration of the layers
* homogeneity within a single layer normal to the substrate surface
* lateral homogeneity

Of course not all of these questions can be answered before the measurement but as much as possible should be clarified. The final aim of an analysis is the determination of an unique result. There are however some points that can already be considered during the fitting process in order to distinguish between unique and non-unique results. Figure 5.11 shows a workflow diagram from data acquisition to the results. After the experiment a model using all information already available on the system is developed. Based on that model the ellipsometric parameters

of this theoretical experiment are calculated and in the next step compared to the experimental data. The mean square error (MSE) is calculated and based on that a decision has to be taken to improve the model or to be confident with the accuracy achieved. It is usefull to test the system with different models and look how the MSE changes. But not only the final MSE is important. During the fitting procedure large jumps in one parameter like the layer thickness without changes in the MSE indicate that there is no well defined minimum and hence the best-fit might no be unique. If the change in MSE is small for a large number of interations there are some parameters likely to be correlated strongly. The algorithm cannot decide which of the correlated parameters should be adjusted first and is stuck in a local minimum. Which parameters are correlated is found out by the correlation matrix. If off-diagnoal elements are close to ±1 there is strong correlation between these parameters. A short look at the confidence limits is helpful in deciding if the model is good or not. For example if a burried layer which does not absorb is included and gives a layer thickness with an error larger than the thickness itself the parameter should be fixed at a value determined in a separate experiment.

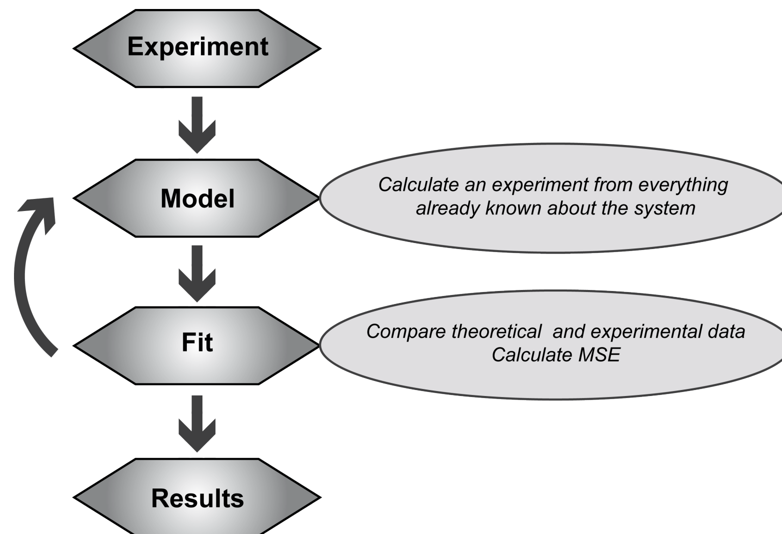

Figure 5.11.: Workflow chart for the data evaluation of an ellipsometry experiment.

If the rules above are followed a model is obtained on which one has to judge if it is good or better than another one. A first insight is obtained if the difference between experimental and theoretical data is randomly distributed around zero. There should not be large peaks and the not trends which indicate deficiencies in the model. In principle it is necessary to keep an eye not only on the results but also on the error estimates of the results and the goodness of fit. The MSE is a measure to compare different models, whether they are physically motivated or not.

5.6.4. Roughness

For all layer thickness determination methods the roughness of surfaces and interfaces is a crucial factor. The simplest way to include roughness into ellipsometry data calculation is the introduction of a so-called graded layer or interface layer. To explain that an effective medium approach is used. The width of the interface should be estimated to have a first guess for the thickness of the artificially introduced interface layer. In a first step three nodes are defined - one on top one at the bottom of the interface and the third half way in between. A function for the shape of the profile of the interface can be defined (steps, linear, etc.) and the refractive index of one layer is gradually changing to the neighboring refractive index. If nothing is known on the type of interface between two layers one should compare different models and profile functions to find out the best model. Surface roughness can be implemented in the same way by a profile with a top node of a refractive index of one.

6. Charge transport properties and microstructure of polythiophene / polyfluorene blends

In this study the structural properties of a polythiophene - polyfluorene blend have been studied in the context of solar cell characterization. The changes in the microstructure of the blend films have been induced by temperature treatment in-situ and ex-situ for x-ray investigations and ex-situ for device parameters. The system itself shows reasonable efficiency.
The work has been done in cooperation with Chris McNeill from the Cavendish Laboratories at the University of Cambridge who prepared the samples and is responsible for the characterization of the solar cell and the transport properties in the device. The x-ray studies have been performed in our group. Further investigations have been done by the group of Peter Müller-Buschbaum using grazing incidence small angle x-ray scattering (GISAXS) and have been published at the same time [88]. Figure 6.1 shows the head of the original publication to which this chapter is almost identical.

6.1. Introduction

Conjugated polymer blends are of interest for application in a variety of organic electronic devices including light-emitting diodes [89], field-effect transistors [90],

Organic Electronics 10 (2009) 1549–1555

ELSEVIER

Contents lists available at ScienceDirect

Organic Electronics

journal homepage: www.elsevier.com/locate/orgel

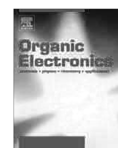

Charge transport properties and microstructure of polythiophene/polyfluorene blends

Heinz-Georg Flesch [a,1], Roland Resel [a,1], Christopher R. McNeill [b,*]

[a] Institute of Solid State Physics, Graz University of Technology, Petersgasse 16, 1 Stock, 8010 Graz, Austria
[b] Cavendish Laboratory, University of Cambridge, J J Thomson Ave., Cambridge CB3 0HE, UK

ARTICLE INFO

Article history:
Received 5 May 2009
Received in revised form 31 August 2009
Accepted 31 August 2009
Available online 4 September 2009

PACS:
61.25.hk
68.55.am
72.80.Le
73.50.Pz
73.61.Ph

Keywords:
Polymer blends
Charge transport
X-ray diffraction

ABSTRACT

We present a combined charge transport and X-ray diffraction study of blends based on regioregular poly(3-hexylthiophene) (P3HT) and the polyfluorene co-polymer poly((9,9-dioctylfluorene)-2,7-diyl-alt-[4,7-bis(3-hexylthien-5-yl)-2,1,3-benzothiadiazole]-2′,2″-diyl) (F8TBT) that are used in efficient all-polymer solar cells. Hole mobility is observed to increase by nearly two orders of magnitude from less than 10^{-7} cm^2 V^{-1} s^{-1} for as spin-coated blends to 6×10^{-6} cm^2 V^{-1} s^{-1} for blends annealed at 453 K at a field of 2.7×10^5 V/cm, but still significantly below the time-of-flight mobility of unblended P3HT of 1.7×10^{-4} cm^2 V^{-1} s^{-1}. The hole mobility of the blends also show a strong negative electric-field dependence, compared with a relatively flat electric-field dependence of unblended P3HT, suggestive of increased spatial disorder in the blends. X-ray diffraction measurements reveal that P3HT/F8TBT blends show a phase separation of the two components with a crystalline part attributed to P3HT and an amorphous part attributed to F8TBT. In as-spun and mildly annealed blends, the measured *d*-values and relative intensities of the 100, 200 and 300 P3HT peaks are noticeably different to unblended P3HT indicating an incorporation of F8TBT in P3HT crystallites that distorts the crystal structure. At higher anneal temperatures the blend *d*-values approach that of unblended P3HT suggesting a well separated blend with pure P3HT crystallites. P3HT crystallite size in the blend is also observed to increase with annealing from 3.3 to 6.1 nm, however similar changes in crystallite size are observed in unblended P3HT films with annealing. The lower mobility of P3HT/F8TBT blends is attributed not only to increased P3HT structural disorder in the blend, but also due to the blend morphology (increased spatial disorder). Changes in hole mobility with annealing are interpreted in terms of the need to form percolation networks of P3HT crystallites within an F8TBT matrix, with a possible contribution due to the intercalation of F8TBT in P3HT crystallites acting as defects in the as-prepared state.

© 2009 Elsevier B.V. All rights reserved.

Figure 6.1.: Copy of the head of the publication.

memories [91] and photovoltaic cells [92]. Polymer blends in particular have been used extensively in the development of organic photovoltaic devices due to the need to pair electron-donating and electron-accepting polymers to drive exciton dissociation and charge separation [93]. Due to the low exciton diffusion length (around 10 nm [94]) compared to the optical absorption length (a few hundred nm) a blended architecture is preferable to a bilayer structure in order to maximize charge generation. The optimum blend structure therefore has domain sizes of order 10 nm to promote efficient exciton dissociation at donor/acceptor interfaces yet with bicontinuous networks to facilitate charge collection. The most efficient polymer blend solar cells utilize blends of a conjugated polymer with a methanofullerene derivate (6,6)-phenyl-C61-butyric acid (PCBM) [95, 96]. The ability of P3HT to form highly ordered, nanocrystal domains in blends with PCBM is cited as one of the reasons for the high efficient of the P3HT/fullerene system [97, 98].The structure and charge transport properties of polymer/fullerene blends have been well-studied [99, 100, 101], demonstrating efficient ambipolar charge transport [102] and the ability to form bicontinuous phases [98]. However, there are fewer reports in the literature of combined structure-transport studies of blends of two conjugated polymers [103, 104, 105]. Such investigations are of interest not only from an academic point of view, since polymer/polymer blends represent a distinct materials class to polymer/fullerene blends, but also from a technological point of view with all-polymer solar cells having the potential to contribute to development of organic photovoltaic technology. In particular, compared to polymer/fullerene blends, the use of two conjugated polymers in a polymer blend solar cell offers greater flexibility in materials design. This flexibility allows for tuning of the electronic properties of the materials (affecting the optical band gap and open circuit voltage amongst others [106]) and tailoring of the physical properties of the blend such as interfaces and phase separation [107].

Recently, we have demonstrated efficient photovoltaic operation from a blend of poly(3-hexylthiophene) (P3HT) with the polyfluorene co-polymer poly((9,9 -

dioctylfluorene) - 2,7- diyl- alt- [4,7- bis(3- hexylthien- 5- yl)- 2,1,3- benzothiadiazole]- 2',2"- diyl) (F8TBT) [108]. Power conversion efficiencies of nearly 2% were demonstrated for this blend, one of the highest for all-polymer solar cells [92]. The successful utilization of the semi-crystalline high-mobility P3HT in efficient all-polymer solar cells also represents an important development [108]. Understanding of the structure of P3HT in blends with F8TBT and its influence on hole transport is therefore important in furthering the development of all-polymer solar cells. To this end, here we report a joint time-of-flight charge transport and x-ray diffraction study of P3HT/F8TBT blends.

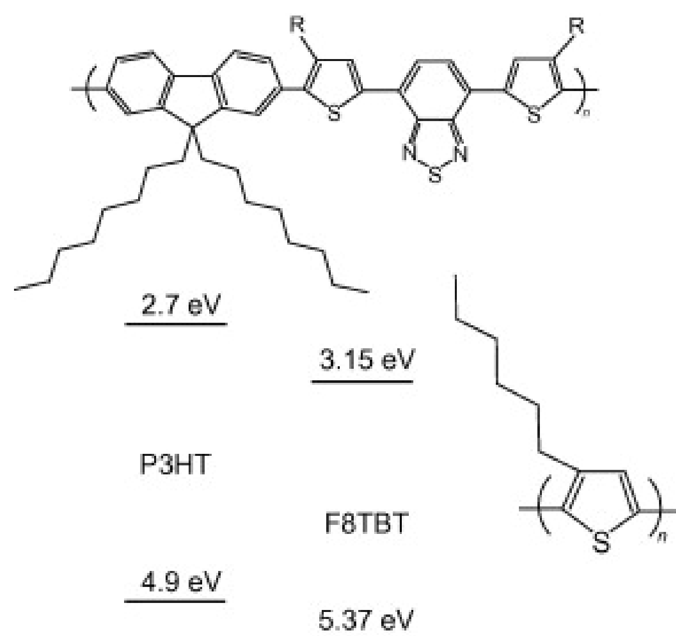

Figure 6.2.: Chemical structures and energy level diagram of F8TBT (R=C6H13) and P3HT.

6.2. Materials and methods

6.2.1. Materials, sample preparation and device fabrication

Regioregular P3HT was supplied by Merck with a molecular weight (Mw) of $52kgmol^{-1}$, polydispersity of 2.4 and a regioregularity of 95.6%. Regiorandom P3HT was supplied by Rieke Metals with a molecular weight of $90kgmol^{-1}$ and polydispersity of 2.4. F8TBT and was supplied by Cambridge Display Technology Ltd. with molecular weight of $54kgmol^{-1}$ and polydispersity of 2.4. The glass transition temperature of F8TBT is 360 to 370 K [109]. Films for both time-of-flight and x-ray diffraction studies were prepared at the same time from the same solutions, by dissolving in anhydrous chloroform at $80mgmL^{-1}$ and spin-coating in a nitrogen glovebox. Rotation speed was varied to obtain approximately the same film thickness. In particular, regioregular P3HT films were spin-coated at 1000 rpm to give a film thickness of $1.6 \pm 0.2\mu m$, regiorandom P3HT films were spin-coated at 1000 rpm to give a film thickness of $1.8 \pm 0.2\mu m$ and F8TBT films were spin-coated at 2000 rpm to give a film thickness of $1.4 \pm 0.1\mu m$. Blend films of regioregular P3HT and F8TBT were prepared by mixing equal volumes of $80mgmL$ P3HT and F8TBT solutions and spin-coating at 1500 rpm to give a film thickness of $1.4 \pm 0.1\mu m$. All film thicknesses were measured with a Dektak 6M surface profilometer. To avoid unnecessary and repetitive clarification, any reference to P3HT will henceforth refer to regioregular P3HT unless specified. Films were annealed either in the glovebox on a hotplate for 10 minutes at temperatures of 373 K, 413 K or 453 K with quenching to room temperature; or in-situ in the x-ray diffractometer (see below). Films for x-ray diffraction study were spin-coated onto cleaned silicon substrates with a $100nm$ thermally grown oxide. TOF devices were fabricated with an ITO/TiO2/P3HT:F8TBT/Au architecture. TiO2 (anatase) acts as a hole-blocking layer and was deposited by spray pyrolysis as follows. ITO-coated glass substrates were heated to 743 K and sprayed with the organic precursor di-iso-propoxy-titanium bis(acetylacetonate) (75 wt.% in isopropanol, Aldrich) from

ethanol (1:10 volume ratio). After 45 minutes drying on the hot plate, a thickness of 50nm of TiO2 was achieved. Au (20nm) was deposited through vacuum evaporation in a chamber inside the glovebox at a pressure of $10^{-6}mbar$. Devices were encapsulated in the glovebox before removal and testing.

6.2.2. Time-of-flight details

Time-of-flight (TOF) measurements were performed using a Nd:YVO4 Q-switched laser (AOT model YVO-25QSPX) with 500ps pulse duration and wavelength of 532nm near the absorption maximum of all polymers used [110]. Voltage was supplied by a battery array (9-72 V) with current recorded using a high speed current amplifier (Femto DHPCA-100) and an oscilloscope (Agilent DSO6052A). Pulse energies of less than 10$nJ/pulse$ were used, with the beam defocused to cover the active area of the device (4.5mm^2). To avoid possible space-charge or recombination effects, the laser intensity was limited such that the collected charge was less than 10% of the capacitor charge. Transit times were estimated from the intersection of asymptotes fitted to the pre- and post-knee regions on a log-log plot of current vs. time as is standard for analysis of dispersive current transients [111]. Due to the high extinction coefficient of both polymers, the majority of light is absorbed within the first 100nm of the film (details in section 6.7). Mobility was calculated as $\mu = d/(Et_{tr})$ where d is the thickness of the film, E is the electric field strength and t_{tr} the transit time.

6.2.3. x-ray diffraction details

X-ray diffraction (XRD) experiments have been performed on a Bruker D8 Discover diffractometer using radiation from a copper sealed tube. On the primary side polycapillary optics with a divergence of 0.3° and a 0.6mm slit were used. On the secondary side conventional slit optics in combination with a graphite monochromator were mounted in front of a scintillation counter. A domed heating

stage supplied by Anton Paar Ltd. [112] was used as a protective sample stage as well as for in situ annealing of samples in vacuo. Annealing in the diffractometer was performed with a ramp of 30 K/minute to the anneal temperature for 10 minutes followed by a slow cooling back to room temperature. The in-situ annealing was performed at temperatures up to 453 K. One sample of the blend material was annealed between 373 K and 453 K in subsequent steps of 20 K for 10 minutes each temperature. In a final step the blend sample was annealed at 453 K for one hour. As a reference, one pure P3HT film was annealed at 413 K and 453 K in subsequent steps as above. All XRD measurements were performed at room temperature using a graphite dome and vacuum to minimize degradation due to x-ray and UV radiation. Careful alignment of the sample has been performed in the primary beam to exclude misalignment errors in the experimental results.
The interplanar distances (d-values) were determined using Braggś formula taking the 2Θ-position of the experimentally observed diffraction peaks. In case of P3HT two different methods were applied (i) using the single 2Θ-position of the 100 reflection and (ii) using all three diffraction peaks and correcting them towards misalignment errors. No significant difference could be observed between these two methods. Therefore, the interplanar distances of the different samples were obtained by using only the 100 diffraction peaks in order to apply the same procedure also to the blend samples where the higher order peaks were weaker. Crystal size determination was performed by using the integral peak width of the individual 100 diffraction peaks by using the Scherrer equation.

6.3. Results

6.3.1. Time-of-flight measurements

Figure 6.3a presents representative time-of-flight transients of P3HT/F8TBT blends annealed at different temperatures compared with that of an unblended P3HT film (unannealed). The transients in figure 6.3a were measured at an electric field

strength of $2.7 \times 105 V cm^{-1}$ for blends and $2.4 \times 105 V cm^{-1}$ for the P3HT film. Figure 6.3a shows a systematic decrease in the transit time with increasing annealing temperature for the blend films. In particular, the transit time improves from not 5 ms (diamonds) to 100 μs (circles) when the as-spun film is annealed at 453 K. The transit for the highest annealing temperature still lags that of the unblended P3HT, 5 μs (squares). Figure 6.3b plots the calculated TOF mobility of blended and unblended films as a function of electric field strength. The change in transit time of 5 ms-100 μs corresponds to an increase in TOF mobility of nearly two orders of magnitude from 8×10^{-8} to $6 \times 10^{-6} cm^2 V^{-1} s^{-1}$. The TOF mobility of the 453 K annealed blend is still over an order of magnitude less than that of the unblended P3HT film that has a TOF mobility of $2 \times 10^{-4} cm^2 V^{-1} s^{-1}$, similar to values measured previously [111]. Examining the electric-field dependence of mobility, figure 6.3b, the blends in general exhibit a pronounced negative field dependence, compared to a relatively flat electric-field dependence of the hole mobility of unblended P3HT. The observation of a strong negative electric-field dependence in the blends compared to the unblended material may be attributed to the higher degree of spatial disorder in the blend [113]. For comparison, we also present the TOF mobilities measured on films of regiorandom P3HT (asterisks in figure 6.3b). Despite having an amorphous film structure, the regiorandom P3HT film has a time-of-flight mobility only an order of magnitude lower than that of the regioregular film, and significantly higher than that of the 453 K annealed P3HT:F8TBT blend. This demonstrates that the lower TOF mobilities of the blend compared to the pure P3HT are related to the film microstructure and not simply the result of P3HT disorder.

We have also investigated the influence of annealing on the unblended regioregular P3HT films, figure 6.4, taken at an electric field strength of $4.2 \times 10^{-5} cm^2 V^{-1} s^{-1}$. A systematic decrease in transit time is also seen with increasing annealing temperature, however the change in the TOF mobility is more modest, increasing from $2 \times 10^{-4} cm^2 V^{-1} s^{-1}$ for the unannelaed film to $3.5 \times 10^{-4} cm^2 V^{-1} s^{-1}$ for the 453

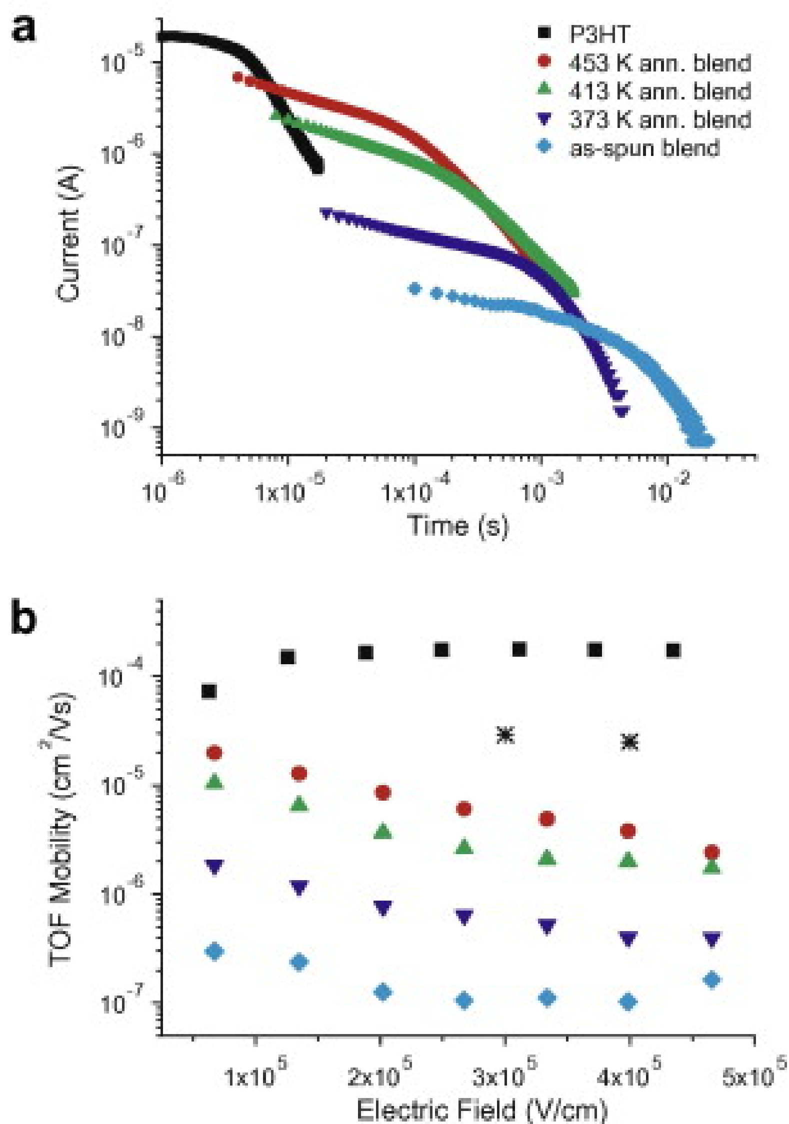

Figure 6.3.: Time-of-flight (TOF) hole transients in P3HT/F8TBT blends and unblended P3HT. Squares represent the unblended P3HT hole transient, while diamonds represent the as-spun blend film, inverted triangles the 373 K annealed blend, triangles the 413 K annealed blend and circles the 453 K annealed blend. (b) Electric field dependence of the TOF mobility for as-spun and annealed P3HT/F8TBT blends and unblended P3HT using the same symbol key as for part (a) Also included are TOF mobilities measured for regiorandom P3HT (asterisks).

K annealed film. Our observation of a large change in the P3HT hole mobility in the blend with annealing, but only a modest change in mobility in the pure P3HT film with annealing, is similar to previous observations for P3HT blended with the methanofullerene PCBM [97].

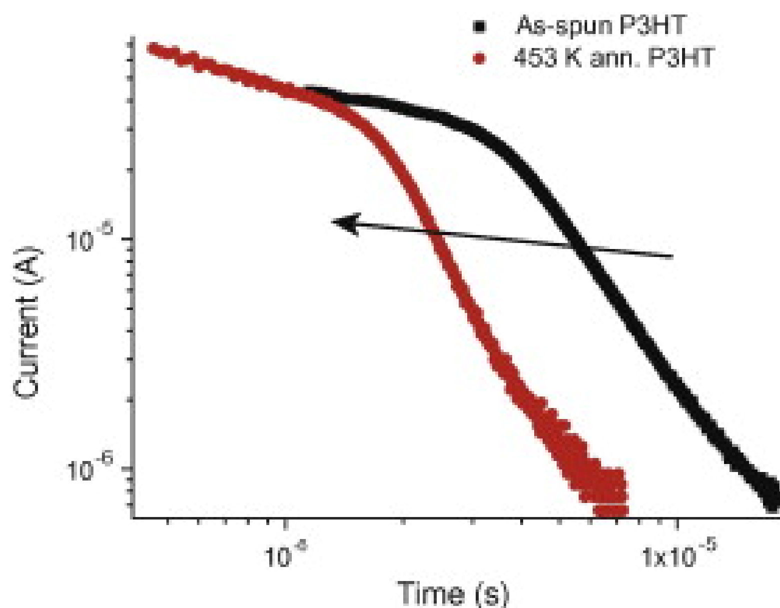

Figure 6.4.: Change in the dynamics of TOF hole transients of unblended P3HT with annealing.

6.3.2. x-ray diffraction results

Specular x-ray diffraction experiments on the as-spun P3HT film show well pronounced 100, 200 and 300 diffraction peaks of the crystalline state without observation of an amorphous scattering contribution (figure 6.5). Annealing of the P3HT film at 413K and at 453K induces an enhancement of the diffraction peaks in intensity together with peak narrowing. Additionally an increase in the interplanar distances is observed, consistent with previous observations [114, 115]. We obtain a shift in the d-value from 1.662nm for the as-prepared sample to 1.667nm

for the same sample after annealing at 453 K (circles in figure 6.6). We note that there is a large variation in the reported d-values of P3HT in the literature [116], but our observations are consistent with reports on similar molecular weight materials measured by Yang et al.[117] and Kline et al. [115]. The F8TBT diffraction pattern shows an amorphous halo at around $2\Theta = 21^{\circ}$ which does not change after annealing. For the blend, in the as-spun state only the 100 P3HT reflection is observed together with the amorphous diffraction feature characteristic of F8TBT with a possible contribution from disordered P3HT.

Annealing of the blend leads to a more pronounced 100 diffraction peak and the emergence of second and third order peaks. In general we find a larger d-spacing for P3HT in blends compared to that measured for pure films. Furthermore, with annealing we see a general trend of decreasing d-spacing with annealing, opposite to the trend observed for pure P3HT films. Specifically, for blend samples that were annealed separately in a nitrogen atmosphere at different temperatures, the P3HT d-spacing is observed to decrease from $1.677nm$ for the as-spun film to $1.668nm$ for the 453 K annealed film (triangles in figure 6.6). For the case of in-situ annealing of the same sample in the x-ray diffractometer, the d-spacing was observed to remain rather constant up to 453K (squares in figure 6.6), but further annealing at 453K (for one hour) resulted in a drastic decrease of the d-value to $1.673nm$, as indicated by an arrow in figure 6.6. The differences in the trends for the two blend sample sets likely arise from the different annealing procedures, with the in situ annealed samples gradually cooled to room temperature rather than quenched. It is interesting to note that in all cases, with annealing there appears to be a convergence of the d-spacing to a value of $\sim 1.668nm$.

For all samples, with annealing there is a significant narrowing of the 100 peak width consistent with an increase in P3HT crystallite size (top panel in figure 6.6). As calculated using the Scherrer equation, the mean P3HT crystallite size in the unblended film increases from $3.7nm$ in the as-spun state to $6.2nm$ in the sample annealed at 453 K. The crystallite size in the blend increases from $3.3nm$ in the

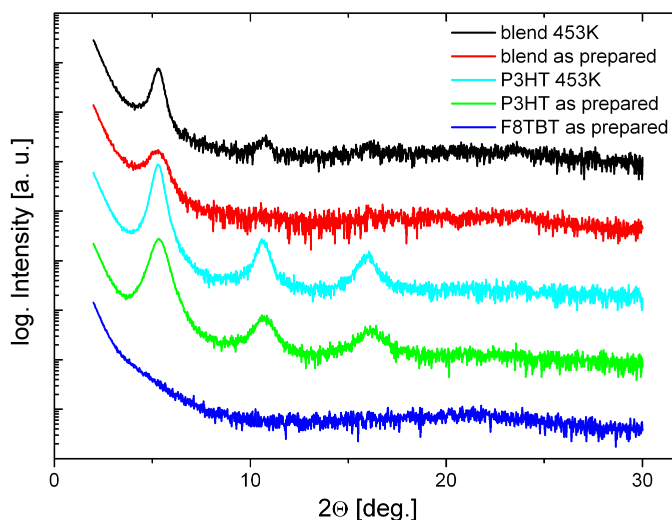

Figure 6.5.: Specular X-ray diffraction curves of 453 K annealed and as-spun P3HT/F8TBT films (top two curves), and P3HT films (next two curves) and of an as-spun F8TBT film (bottom curve). The curves have been shifted for clarity.

as-spun film, to 3.8nm with annealing at 373 K, to 5.0nm with annealing at 413 K (average of two samples) and to 6.0nm with annealing at 453 K, close to the value for 453 K annealed P3HT. The increase of the crystal size is slightly larger in case of the blends, which can be seen from the steeper negative slope of the integral breadth above 373 K (figure 6.6).

6.4. Discussion

The experimental results reveal that the 1:1 blends of P3HT and F8TBT show a phase separation in two components with a crystalline part and an amorphous part. Within the x-ray diffraction pattern of the as prepared sample the presence of a crystalline component is deduced from the presence of the diffraction peak at a d-value of 1.677nm, while the amorphous part is clearly evident from the amorphous halo at around $2\Theta = 21°$. Since the d-value of the crystalline part is close to the

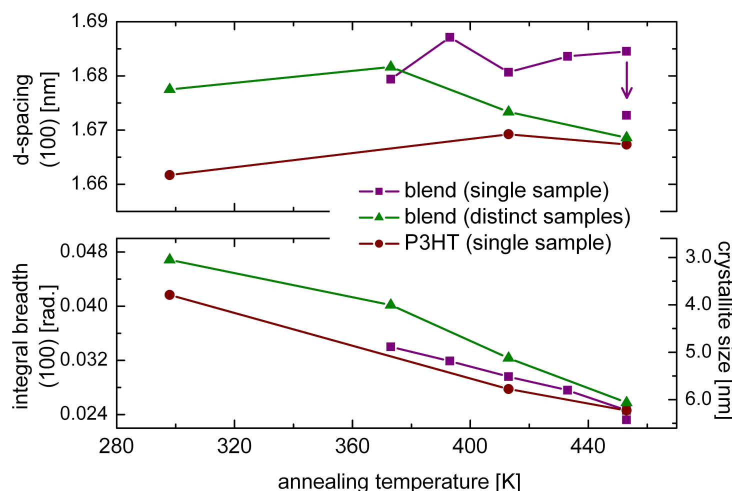

Figure 6.6.: The upper panel shows changes in the interplanar distances of the 100 plane with annealing for blends and unblended P3HT. The lower panel shows the effect of annealing on the integral breadth of the 100 reflection as a function of annealing temperature. The right hand axis in the lower panel displays the corresponding crystallite size calculated using the Scherrer equation.

P3HT value, it can be attributed to P3HT crystallites. However, this crystalline part cannot be formed only from pure P3HT, since the experimentally observed d-values as well as the relative intensities between the reflections are noticeably different. These two experimental observations reveal that the P3HT crystals in the blend are distorted. Since spin-coating is a non-equilibrium process, the packing of P3HT in the blend may be affected by solvent molecules or F8TBT molecules enclosed as impurities in the P3HT crystals. A recent report has also observed an increase in the d-spacing of the polythiophene poly(2,5-bis(3-tetradecylthiophen-2-yl)thieno[3,2-b]thiophene) (pBTTT) when blended with PCBM attributed to the intercalation of PCBM between the side-chains of pBTTT [118]. In contrast, blends of PCBM with P3HT show no change in the d-spacing of P3HT [96, 119] as the side-chains in P3HT are too dense to allow intercalation of the bulky PCBM

[118].

Annealing of the polymer blends leads to a gradual approach of the d-values of the crystalline part of the blend to that of pure P3HT. Since remaining solvent molecules within spin coated films are evaporated at annealing temperatures well below 373 K [120], it can be inferred that the P3HT crystallites are distorted by the presence of F8TBT polymer chains. This distortion could be either a direct incorporation of F8TBT polymer chains into P3HT crystals or the intermixing of the sidechains from both types of polymers. With increasing annealing temperature the two d-values of blend and pure P3HT come closer which reveals that the influence of F8TBT on P3HT packing decreases. The increasing crystallite size from $3.3nm$ in the as-prepared state to $6.2nm$ in the sample annealed at 453K is a clear marker that a major re-arrangement happens during the annealing process. Such a re-arrangement would allow a reduction in the influence of F8TBT impurities on the packing of crystalline P3HT, evolving to a packing comparable to pure P3HT. We conclude that the final state of the blend consists of separated regions of amorphous F8TBT and crystalline P3HT containing only a negligible amount of F8TBT molecules as impurities.

We now turn to explain the trends in the TOF data in terms of the observed microstructure. Curiously, both unblended P3HT and P3HT/F8TBT blend films were found to have similar crystallite sizes as a function of annealing temperature. Thus the large discrepancy in general between the TOF mobilities of blended and unblended P3HT cannot be explained by differences in the size of P3HT crystallites alone. Similarly, the vast improvement in the mobility of P3HT/F8TBT films (over two orders of magnitude) cannot be explained in terms of variations in P3HT crystallite size in annealed blends, as only a modest change in mobility is observed in unblended P3HT for a similar change in crystallite size. As discussed in section 6.3 where we noted the moderate TOF mobility of regiorandom P3HT films, differences in the overall degree of crystallinity of P3HT also cannot explain the orders of magnitude improvement in hole mobility in the blend with anneal-

ing. We therefore seek to explain the observed trends in terms of P3HT packing distortions and film morphology as follows.

Firstly from the X-ray diffraction measurements there is strong evidence for the presence of F8TBT chains in P3HT crystallites in as-spun and mildly annealed P3HT/F8TBT films. These F8TBT chains that are incorporated inside P3HT crystallites represent defects that may act as scattering or trapping sites for holes, impeding charge transport [121]. (We note however, that since F8TBT has a deeper HOMO, 5.37 eV, compared to P3HT, 4.9 eV, F8TBT is unlikely to act as a hole trap in itself.) Secondly, the physical structure of the blend will adversely affect hole transport particularly if P3HT crystallites are isolated due to an enclosing F8TBT phase. The observation of a strong negative electric-field dependence in the blends absent in pristine P3HT supports this assertion, with a negative electric-field dependence attributed to spatial disorder [113]. While we are unable to directly determine the crystallite content from the XRD measurements, recent photophysical studies estimate the crystallite content of unblended P3HT at 40-50% [122]. Thus in a blend with another polymer the crystallite content will be further diluted, with crystallite percolation pathways more likely in annealed films with larger crystallites than in unannealed films with smaller crystallites. Similar percolation thresholds have been observed for electron transport in blends of conjugated polymers with fullerene derivatives [102]. Given the amorphous nature of F8TBT and the propensity of P3HT to form isolated fibrils [101], it is indeed likely that the bulk morphology of the film will favour isolated P3HT domains surrounded by a continuous F8TBT phase, particularly at low anneal temperatures. Furthermore, the measured P3HT crystallite size does not necessarily represent the P3HT aggregate size, and films annealed at higher temperatures (and/or for longer times) will therefore have the opportunity for P3HT crystallites to move and aggregate. Figure 6.7 schematically presents the proposed structures of as-spun and annealed P3HT and P3HT/F8TBT films. For the case of unblended P3HT, annealing serves to increase the crystallite size, improving charge trans-

port through a reduction in the number of inter-domain hops. However, in both unannealed and annealed P3HT films there is relatively good interconnectivity between domains with only a modest increase in mobility. For the case of uannealed P3HT/F8TBT, it is proposed that the distorted P3HT crystallites are surrounded by a continuous F8TBT phase that inhibits inter-domain hops. Hole transport relies either on inefficient inter-domain hopping possibly mediated by disordered P3HT chains that may exist as a minority component in the F8TBT phase. In contrast, in annealed P3HT/F8TBT films the crystallites have a chance to aggregate as they grow establishing interconnected percolation pathways. It is this change from isolated to interconnected domains that then accounts for the order of magnitude increase in hole mobility in the blend with annealing.

These measurements also have implications for understand photovoltaic device performance. It is found that an annealing temperature of 413 K is required for optimum photovoltaic performance [110]. The results here show that at this annealing temperature the film is still in an intermediate state of phase separation and purity of P3HT crystallites. Furthermore, the charge transport mobility of the P3HT phase still lags that of 453 K annealed films that demonstrate inferior device performance [88]. Therefore it appears that it is not bulk charge transport that is primarily determining the efficiency of P3HT/F8TBT blends, but rather the intermediate state of phase-separation that exists in 413 K annealed films balances the two processes of charge generation (exciton diffusion and dissociation and donor/acceptor interfaces [88, 123]) and charge separation (separation of bound electron-hole pairs from the donor/acceptor interface [124]). Also of interest, particularly for photovoltaic operation, is the influence of film microstructure and morphology on electron transport. However, the transport of electrons in P3HT/F8TBT blends is adversely affected by trapping effects making the observation of clean TOF transients difficult [125] and beyond the scope of this study. Curiously the intercalation of F8TBT chains in P3HT crystallites may represent a microstructural origin for electron trapping in these blends and further research

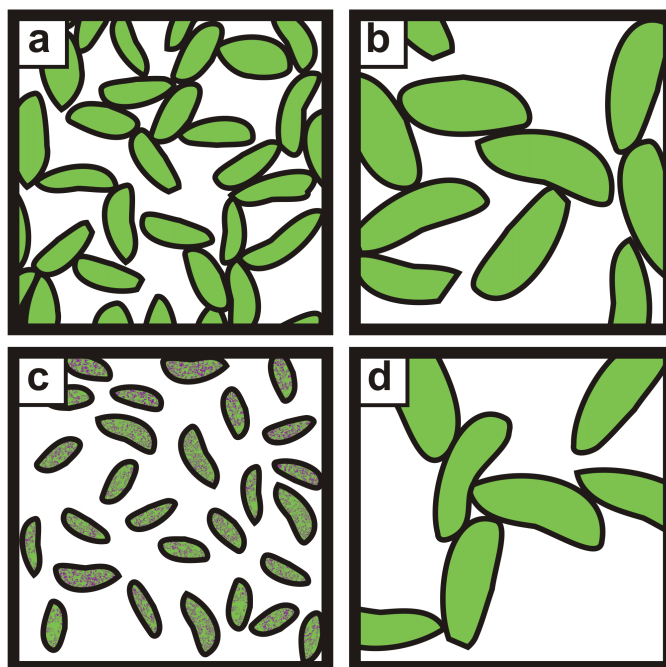

Figure 6.7.: Schematic diagram of the proposed structures of P3HT (a and b) and P3HT/F8TBT blends (c and d). (a) Presents the schematic structure of unannealed P3HT with smaller crystallite size and (b) the structure of annealed P3HT (453 K) with larger crystallite size. (c) Shows the proposed structure of unannealed P3HT/F8TBT with smaller, distorted P3HT crystals surrounded by an F8TBT matrix. (d) Shows the structure of annealed P3HT/F8TBT (453 K) with larger, pure P3HT crystallites with good interconnection.

is planned to investigate this.

6.5. Conclusions

We have measured the charge transport properties and microstructure of P3HT / F8TBT blends. The X-ray diffraction results reveal that P3HT/F8TBT blends show a phase separation of the two components with a crystalline part attributed to P3HT and an amorphous part attributed to F8TBT. In as-spun and mildly annealed blends, the measured d-values and relative intensities between the P3HT reflections are noticeably different to unblended P3HT indicating an incorporation of F8TBT in P3HT crystallites that distorts the crystal structure. At higher anneal temperatures the blend d-values approach that of unblended P3HT suggesting a well separated blend with almost pure P3HT crystallites. We explain the increase in hole mobility in the blend with annealing in terms of an increase in the P3HT crystallite purity and the aggregation of P3HT crystals to form percolation pathways.

6.6. Acknowledgements

This work was supported in Cambridge by the Engineering and Physical Sciences Research Council (EP/E051804/1) and in Graz by the Austrian Research Promotion Agency (FFG) within the RPC ISOTEC. C.R.M. acknowledges Cambridge Display Technology Ltd. for the provision of F8TBT, and assistance from Dr. D. Kabra with the deposition of TiO2.

6.7. supplementary information

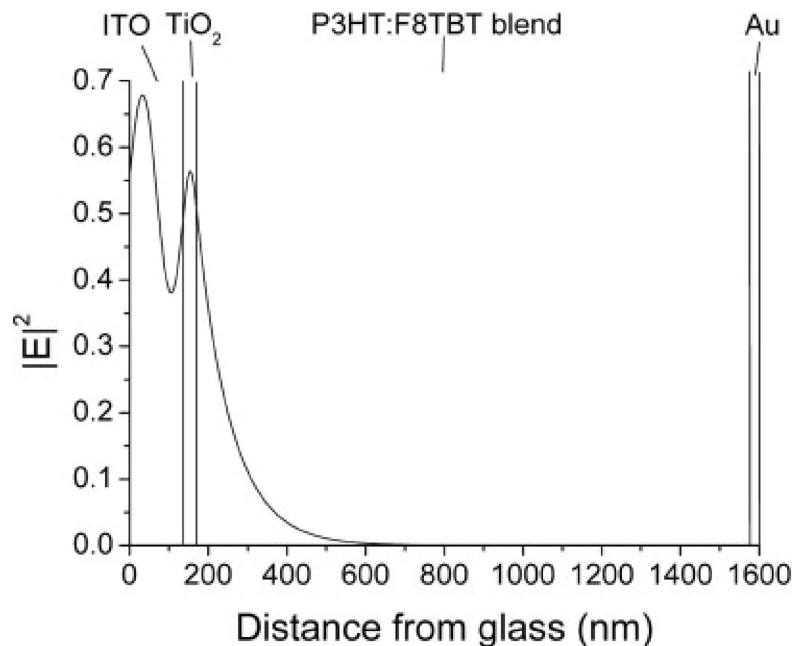

Figure 6.8.: Optical electric field profile inside the glass/ITO/TiO2/P3HT:PCBM/Au structure for an incident wavelength of 532 nm. The generation rate of excitons is proportional to $|E|^2$. This profile was calculated using the transfer matrix method using optical constants acquired using spectroscopic ellipsometry and from the literature [88]. $|E|^2$ drops to 1/e of its initial value 90 nm into the P3HT/F8TBT film and drops to 10% of its initial value 200 nm into the P3HT/F8TBT film.

Appendix

A. Supplementary investigations on quinquethiophene self-assembled monolayers

A.1. Passivated molecules

Additionally to the SAM formation and experiments on the self-assembled monolayers, experiments using a solution of passivated molecules solely have been performed. Passivated refers in that case to the same molecule as used for the SAM formation but without the Si group at one end (C2-5T-C11). The molecules have been dissolved in toluene and transferred to silicon dioxide substrates by drop casting. This procedure did not yield homogeneous films as one could judge just by eye. The layer is obviously full of precipitation but the rather slow evaporation process of drop casting allows the material to crystallize.
At room temperature XRR measurements have been performed presenting no Kiessig fringes as expected from an inhomogeneous layer (figure A.1). Bragg peaks are found at positions $q_z = 0.187\mathring{A}^{-1}$ and $q_z = 0.375\mathring{A}^{-1}$ which have been indexed as 001 and 002 respectively giving a d-spacing in the specular direction of approximately $d_{001} = 33.54\mathring{A}$. After a temperature treatment of 550K the crystallographic structure parallel to the substrate surface is lost and there remains a smoothened layer of a thickness of approximately $148\mathring{A}$. As already seen for the SAM the layer of drop casted material is also more stable concerning temperature treatment than

its crystallographic out-of plane order (the crystallographic in-plane order is lost as well before layer desorption as will be shown below).

Grazing incidence in-plane x-ray diffraction experiments show that the layer is quite well ordered and consists of two types of structure. One type is not well seen in figure A.1 but corresponds to the phase of upright standing molecules with Bragg peak directly at the sample horizon (same as seen for pristine quinquethiophene SAM samples). The other phase correspond to a structure of tilted molecules. In the figure the Bragg peaks have been indexed in a first attempt. This results in a unit cell of $a = 5.53Å$, $b = 8.45Å$, $c = 33.54Å$, $\alpha = 112.5°$, and $\beta = \gamma = 90°$. The Debye Scherrer rings have been plotted as well to show that the arc-like Bragg rods are not only rings in a sense of powder rings. The arc-like shape is due to the distribution of α-angles that can be assumed within the crystal structure. The solution is not unique and to every α a slightly different unit cell has to be built. This stands for a large number of slightly differing unit cells, each with a slightly different tilt of the molecules. The arc-like shape of the Bragg peaks is addressed to that fact.

Figure A.2 presents a temperature annealing study of the spin coated layers. When heated the presence of two distinct phases becomes more obvious. A clear separation of the two peak series can be observed already at 400K.

Up to 520K the peak stemming from the tilted molecules gets more and more straight in a sense that the arc-like shape disappears. This would correspond to a narrowing of the distribution of different unit cells within the crystallographic structure. The data can be interpreted as a smectic phase presenting well separated layers which explains the specular Bragg peak and the possible indexation using *hk0* for all in-plane peaks. Within one of these layers the tilt is uniform but each layer shows a different tilt angle of the molecules. Upon temperature treatment the molecules are forced to align into their energetically favorable packing. Due to drop casting the molecules are not able to align immediately in their optimum packing.

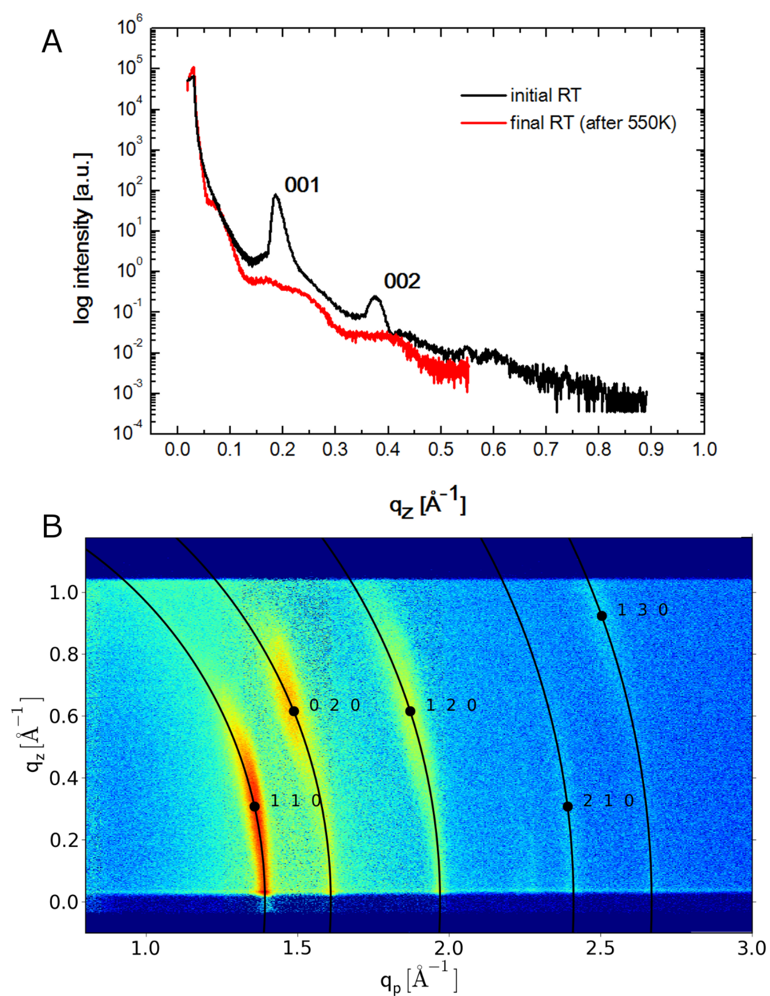

Figure A.1.: Specular scans of the drop casted layer before and after heating to 550K (A) and reciprocal space map of the same film before temperature treatment with a first indexation of the Bragg peaks.

At this point it is emphasized that the straight Bragg rods like at 460K and at 520K correspond to a uniform alignment of the molecules as expected for perfectly aligned monolayers.
As the peaks show a trend to smaller q_z in the reciprocal space maps for higher temperatures the molecules tend to stand up due to temperature treatment. Starting from $\alpha = 112.5°$ the angle decreases to a value of $\alpha = 107.6°$ at 520K.
The trend of standing up is seen in correspondence to the SAMs where at elevated temperatures only fully upright standing molecules are found. The phase of tilted molecules in this investigation is understood in terms of a bulk phase. This phase gets lost above 520K where only the phase of upright standing molecules remains. This is seen as a surface induced thin film phase that is stable up to 540K.
Above 540K the crystallographic in-plane structure is irreversibly lost, the out-of-plane structure has not been followed in detail, but is also lost after heating to 550K.

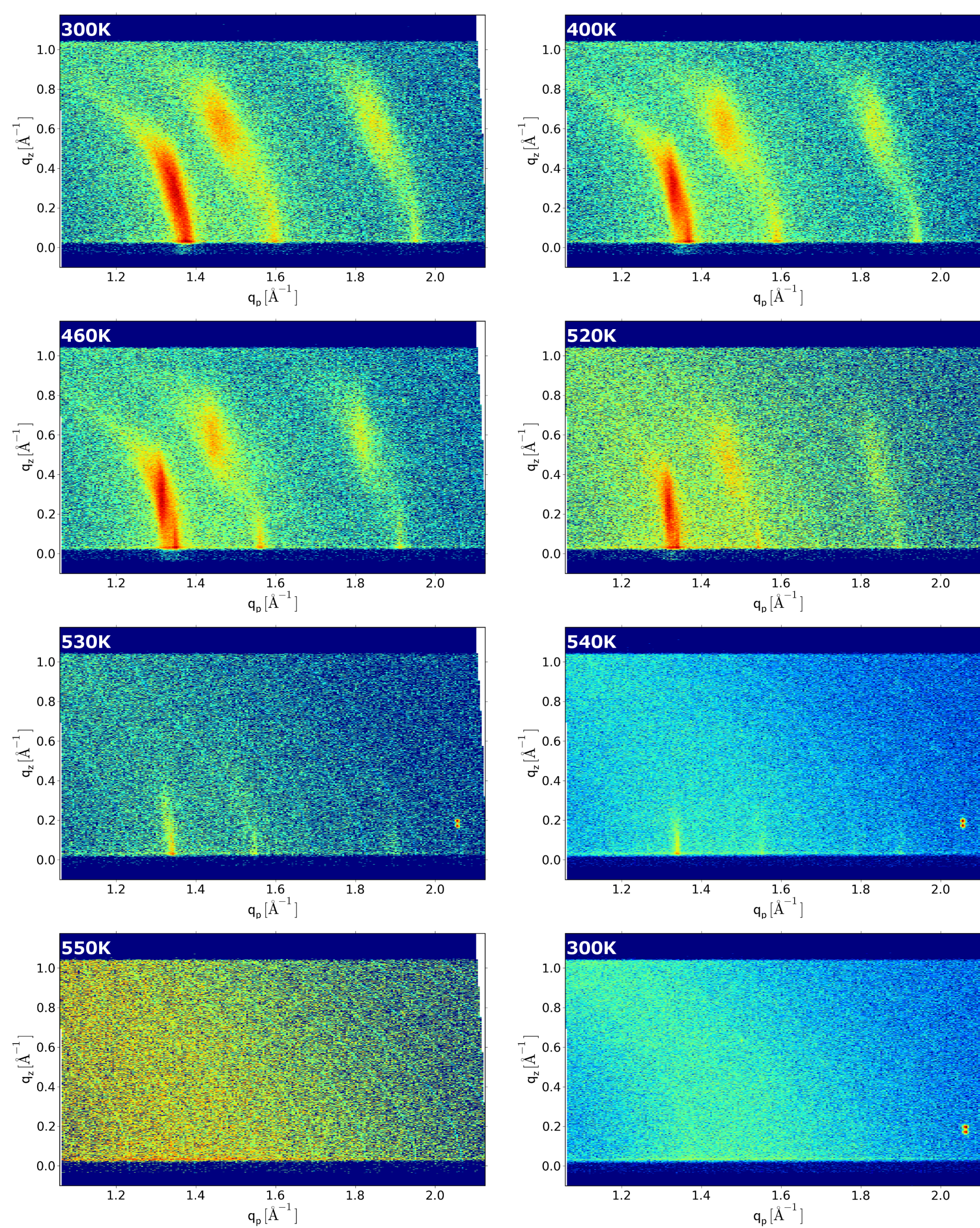

Figure A.2.: Reciprocal space maps of drop casted passive 5T-SAM molecules. The sample is being heated up above the melting point of the quinquethiophene.

A.2. Stability of self-assembled monolayers

A big issue in organic electronics is the air stability of the materials. Of additional interest in structural research is the stability of the material under the x-ray beam. Both factors are shortly addressed within the next sections.

A.2.1. Long term stability of a 5T-SAM

The question of long term stability and stability of the layer thickness after temperature treatment has been followed for one sample. Since there have not been changes in the crystallographic order after one and two years of storage under ambient conditions the question is about stability of the layer thickness. For that purpose a sample has been heated up to 500K at the ESRF and been measured there. Afterwards the thickness has been measured on a Bruker D8 Discover machine using copper radiation and again on a Panalytical Multipurpose Diffractometer using copper radiation as well (compare figure A.3 for all measurements). The comparison of the fast oscillating Kiessig fringes of the silicon oxide by Fourier Transform confirms that there is no difference between the measurements and experimental setups. The oxide layer has a layer thickness of $d = (224.5 \pm 0.4)nm$ for all setups.
There is some decreasing layer thickness visible by the shift of the Kiessig fringes towards larger scattering vectors. At this point the reason for that is not clear. The effect is probably connected to the heating of the sample and the drying of the SAM. But there is no complete understanding of this behavior up to now.

A.2.2. Degradation of a 5T-SAM under the x-ray beam

Thin layers of organic materials that are exposed to light might already change their morphology or surface properties. Irradiation of such sensitive layers using x-rays deposits energy in the film and therefore degradation under the x-ray beam is always an issue in thin film characterization of organic materials.

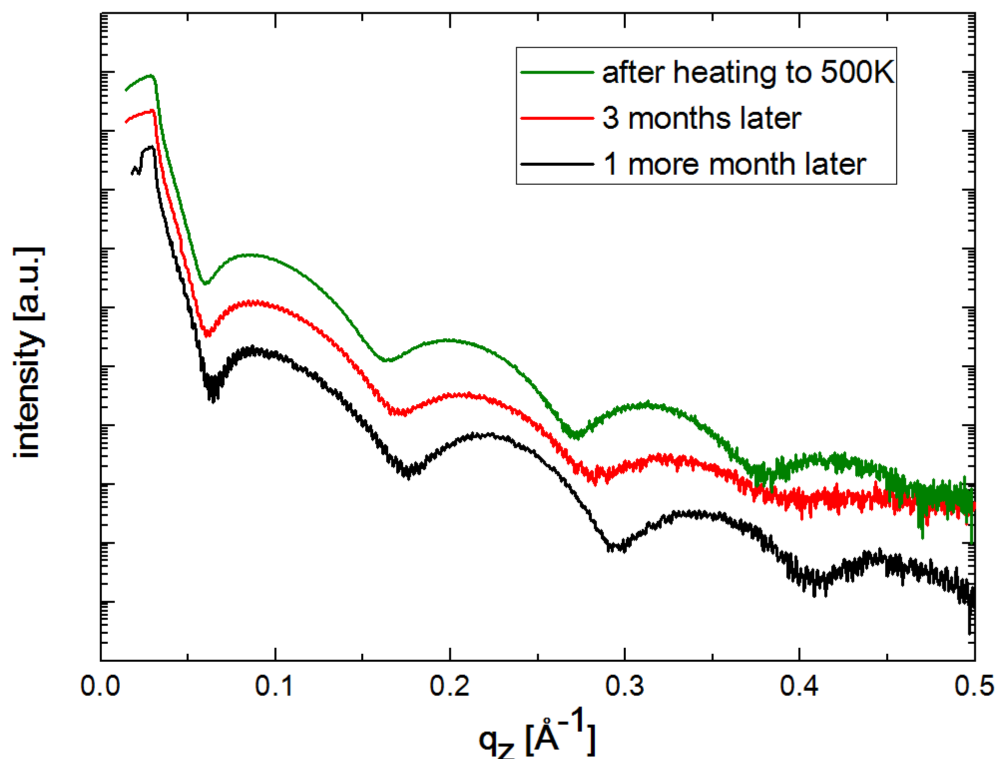

Figure A.3.: XRR measurements directly after heating to 500K, 3months later and again one months later. The curves are shifted for clarity.

Additional risk of damaging the material arises in the combination of x-ray irradiation and temperature treatment. It has been observed that the SAMs are stable under the x-ray beam at room temperature. At least the degradation is negligible in terms of the crystallographic order of the system. There may be other effects in the material induced by x-rays but the crystallographic order remains stable at room temperature.

The introduction of temperature to the system however changes the situation dramatically. The intensity of the peaks decreases steadily with increasing temperature. There are several possibilities to face that problem. As the synchrotron beam is rather narrow it is possible to move the sample laterally and irradiate

always a new position (that has not been irradiated before) on the sample. A second possibility is to stay at one position until the signal gets too noisy and change then to a different position on the sample.

Depending on the aim of the investigation the decision has to be taken. By several measurements it has been proven that the change of the unit cell parameters (the position of the Bragg rods in q_p and q_z) is temperature induced and not influenced by the beam. The influence of the beam only weakens the signal *i. e.* worsens the peak to noise ratio.

This leads to the approach of staying at one point and heating the sample until the peak to noise ratio gets bad and switch then to a new position. It has been found that even when the crystallographic structure seemed lost it has been there at a pristine position on the sample. This makes the in-situ investigations tedious and data evaluation has to be done carefully. Figure A.4 shows a selection of reciprocal space maps during the temperature treatment. The scalebar for the intensity is equal for all maps.

Obviously the crystallographic structure is not necessarily destroyed if the Bragg rods disappear. Scanning a different spot of the sample is of importance. A final scan after cooling to room temperature has usually been performed as well at a pristine position to prove that the long-range order has been destroyed by temperature and not by the x-ray beam.

The reason for the degradation is addressed to the additional energy that is introduced to the system by the beam or by temperature. If only one energy source is applied the sample is stable for a longer time.

A.3. Intensive AFM and TSM investigations

Additionally to the already presented AFM and TSM data further measurements have been performed on not x-ray illuminated samples as well as on already heated and x-ray irradiated samples of SAMs.

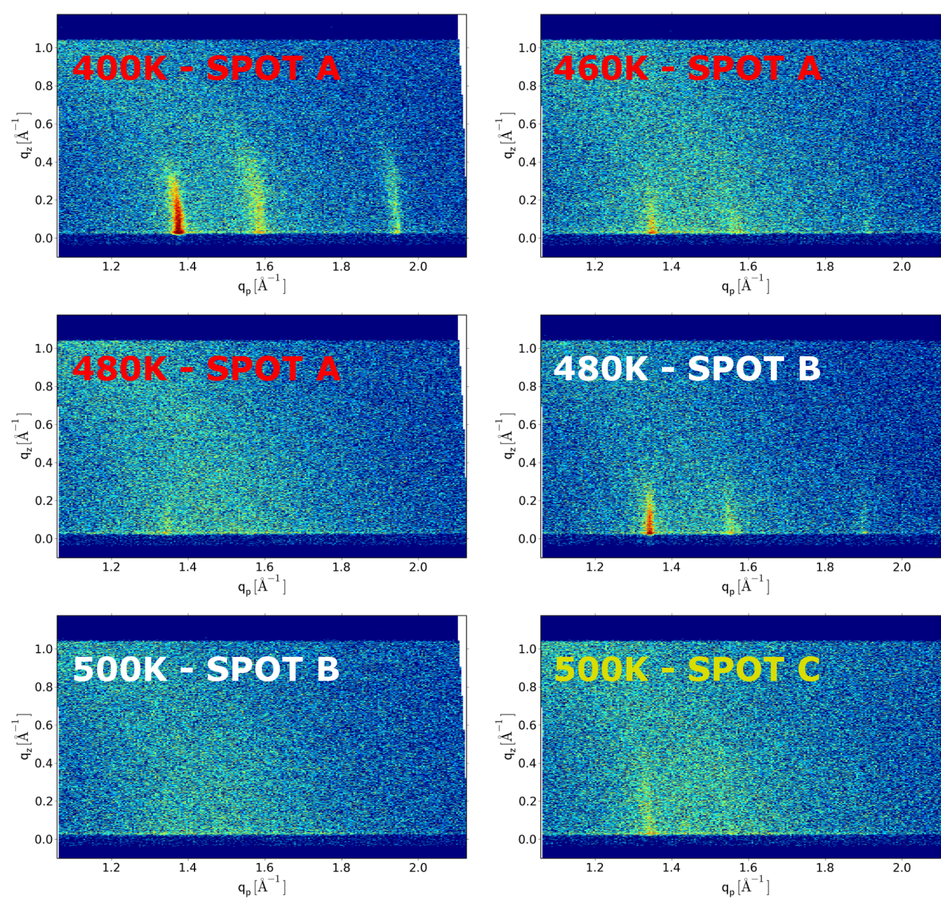

Figure A.4.: Reciprocal space maps of a SAM on three different positions on the sample. Intensities are scaled equally for all maps.

The findings of these investigations are not fully understood and comments on the data are speculative at the moment.

A.3.1. A submonolayer

A sample that has been immersed into the solution for 2.5 hours shows a clear submonolayer state of the SAM. The specific SAM has been annealed at 400K and then been characterized using an AFM in tapping and contact mode. TSM images have not been recorded as no domain boundaries are expected in this early stage of layer growth. The recorded images of topography and phase are presented in figure A.5.

The topography of the sample is presented in part A, which is zoomed in and shown in more detail in parts C, F and G. This early stage of layer formation already shows some second layer growth marked by the red circle. An image of another spot (B) shows the same initial state of a second layer. The cross sections of both images (A,B) present the island type of layer formation of the SAM whereas the lower cross section shows a nucleation center of the second layer being again approximately $3nm$ in height.

This type of precipitation and initial growth from nucleation centers is also found directly on the substrate when looking at the images C and G. The crystalline domains start to grow from an initial needle which are homogeneously spread over the surface. Hence it can be speculated that the domain size (presented in 3.27) depends rather on the number of nucleations centers than on post layer formation treatment. The reason for a larger or lower number of such centers is not clear but is suggested to be connected to the cleaning and preparation of the substrate. The topography in D and the corresponding phase image E allow further speculation on the spots of initial growth all over the substrate - as expected for isotropic surfaces. The needles are the centers for spontaneous layer formation which are randomly distributed over the area. The phase image of the SAM surface itself is smooth again.

The edges of the growing self-assembled monolayer look like a fractal boundary of growing needles which are getting interconnected after some time and form the layer. It is shown in image C and F that the layer does not grow with sharp edges. On the other hand there are sharp steps found in image B and D respectively between SAM and substrate. From that series a judgment on how the layer actually forms is difficult.

A.3.2. A closed monolayer

After approximately one day in the solution the full coverage of the SAM is reached. Two samples, both have been in the solution for 22 hours are investigated by AFM. One of the samples has been annealed at 400K (C-F) and not been measured by x-rays (there is some impact on the layers as shown in the section before) and the other one heated up to 500K and investigated at the synchrotron (A, B). The morphology is presented in figure A.6 in the left column, corresponding TSM images are shown in the right column.

The images do not show the smooth and expected morphology as earlier series of the SAMs did. The nucleation centers seen in figure A.5 are still visible in the closed layer. Very pronounced spots can be found in the not irradiated sample at two distinct spots on the sample (C-F). Nucleation centers seen in the morphology are also visible in the TSM mode but the domain areas around them are much more dominant in the morphology.

The situation is vice versa for the sample that has been exposed to 500K and the x-ray beam. In that case there are some areas visible in the morphology image (A) and clear domains around each nucleation center in the TSM image (B). Additionally there is some free space left over between the domains in the TSM image. It is speculated that this separation of the domains is caused by the temperature treatment, because image C show the same features but less pronounced due to a lower maximum temperature.

There might be speculated about partial desorption of of the SAM and lateral ex-

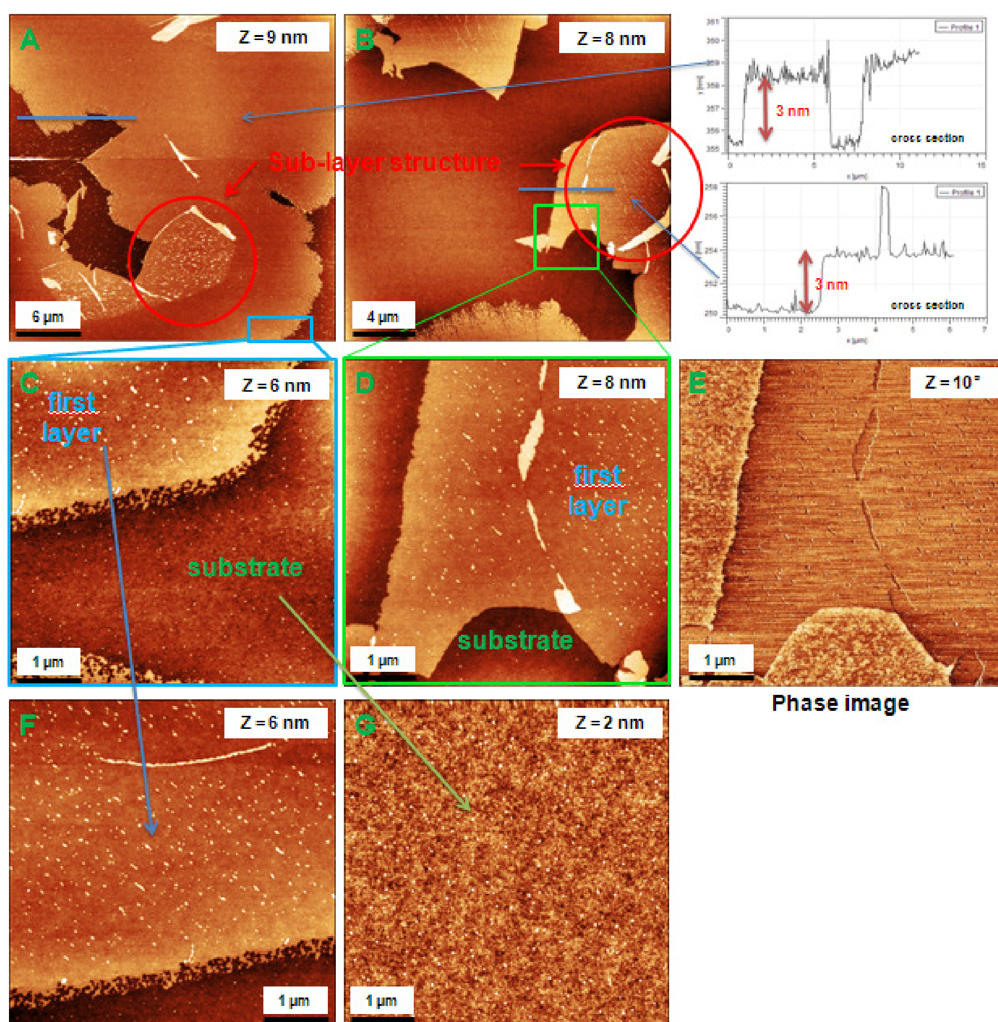

Figure A.5.: Submonolayer AFM of a sample submerged in the solution for 2.5hours. The topographical image A has been zoomed in corresponding to the blue rectangle area (A → C → F, G) and the image B correspondingly at the green rectangle area (B → D). The cross sections have been recorded corresponding to their blue lines in A and B. Image E shows the phase contrast of D.

pansion and contraction of the layer due to temperature treatment but by means of the actual measurements it is not possible to clarify that. The speculation on desorption and expansion is supported by the changes in the unit cell parameters and layer thickness that have been presented in chapter 3. Perhaps in-situ temperature dependent AFM can reveal that.
Figure A.7 shows morphology and corresponding TSM image of a sample that has been in the solution for 100 hours and annealed at 400K afterwards. In that case both images are rather smooth - presenting no nucleation centers. Indications of domain boundaries are seen in case of the TSM image which correspond to the data of chapter 3.
The difference to chapter 3 is that the series presented here has been fabricated on hand cut Si-wafers the other series from batches of machine cut Si-wafers. There might always remain some dust from cutting the wafer which cannot be cleaned fully. Si-dust provides a higher nucleation center density which could explain the different behavior of this sample series.

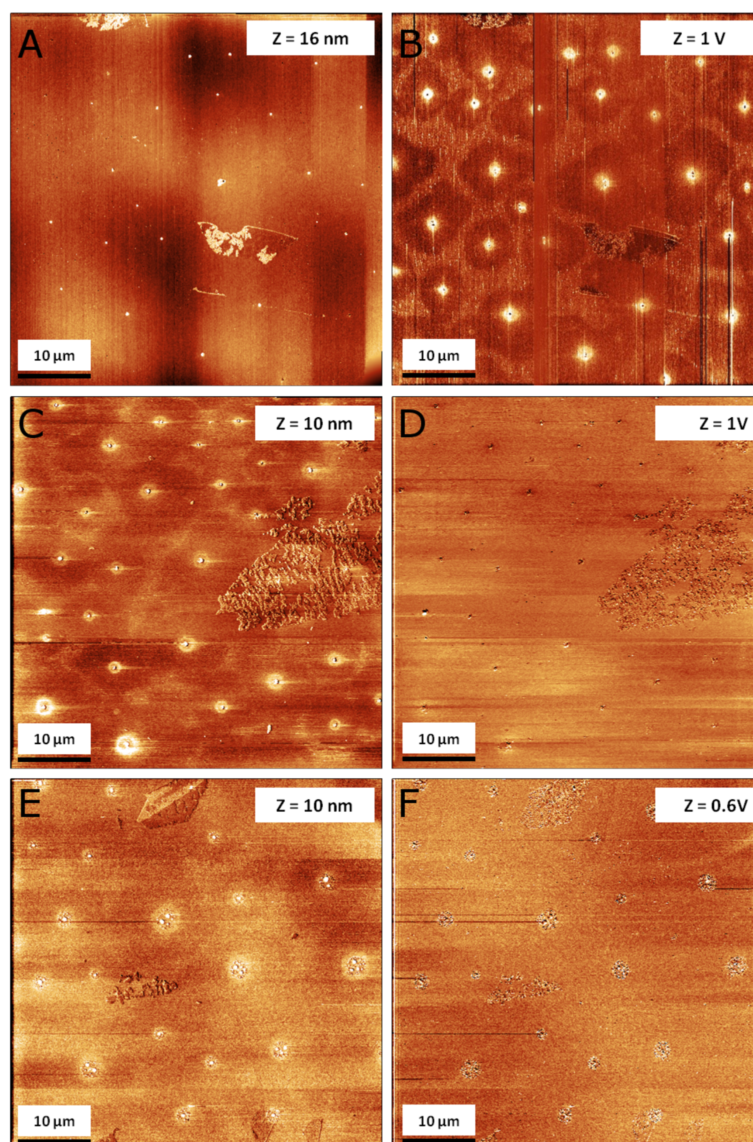

Figure A.6.: The right column shows TSM images the left column the corresponding topography data of a closed monolayer after 22 hours in the solution. A and B have been taken after x-ray irradiation and heating at 500K; C-F have been taken after annealing at 400K.

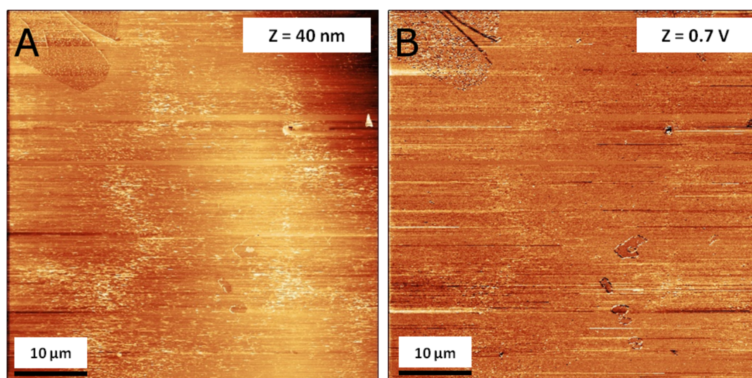

Figure A.7.: A shows the topography data of a closed monolayer after 100 hours in the solution and B the corresponding TSM image. The sample has been annealed at 400K.

B. Curriculum vitæ

Personal Data

name	Heinz-Georg FLESCH
date of birth	April 15th 1981
place of birth	Voitsberg, Austria
nationality	Austrian
languages	German (mother tongue)
	English (fluently)
	Italian (basic knowledge)
	Latin (basic translations)

Education

since 2007	Institute of Solid State Physics, TU Graz; Working on structure and morphology of thin organic films using x-rays, ellipsometry and AFM
11|05 – 12|06	Diploma Thesis: GW-Calculation of the Self-Energy of Electrons in Simple and Transition Metals (supervisor: Heinrich Sormann)
10|00 – 12|06	Diploma in Physics; Graz University of Technology (TU Graz), Austria, Specialization: Quantum Mechanics, Computational Physics, Numerical Methods, Mathematical Methods, Theoretical Solid State Physics
10|99 – 09|00	Civil Service, Austrian Red Cross, Voitsberg, Austria
09|91 – 06|99	Grammar School, BG/BRG Köflach (A levels with distinction)
09|87 – 06|91	Primary School, Voitsberg, Austria

Grants and Awards

2002	Styrian Competition in Paramedical Aid; in second place; Gröbming, Austria
2000	Austrian Competition in Paramedical Aid; in second place; Hollerbrunn, Austria
1999	Jugend Übersetzt, Italian; in first place; Graz, Austria
1998	Jugend Übersetzt, Italian; in second place; Graz, Austria

Teaching activities

10|09 – 03|10	Assistant Lecturer; Advanced Laboratory Exercises, x-ray diffraction, Institute of Solid State Physics, TU Graz
10|08 – 03|10	Lecturer; Physics and Introduction to Biomechanics, Physiotherapy, FH Joanneum
10|08 – 03|09	Assistant Lecturer; Lab Course Macromolecular Chemistry and Technologies, Institute of Chemistry and Technology of Materials, TU Graz
10|03 – 01|07	Assistant Lecturer; Physics Laboratory Practical for Chemists, Institute of Experimental Physics, TU Graz
10|03 – 06|06	Assistant Lecturer; Basic Practical for Physicists 1, Institute of Experimental Physics, TU Graz

Computer skills

OS	Linux, Windows
Desktop	MS Office (Word, Excel, Powerpoint)
Scientific Tools	Matlab, Mathematica, Origin
Tools	Photoshop, Illustrator, Dreamweaver, CorelDRAW
Programming	Fortran 90, C
Typography	LaTeX, emacs

Interests

Sports (running, swimming, cycling, cross country skiing)

Photography (Sports, People, Animals)

Reading (crime stories)

Non Scientific Activities

04|10 – 06|10	Coach; University Sports Center, Marathon course, Graz, Austria
1995 – 2008	Unsalaried Paramedic; Austrian Red Cross, Voitsberg, Austria

C. Scientific activities

C.1. Publications

* **Phase behavior and stability of a quinquethiophene based self assembled monolayer as a function of temperature**, H.-G. Flesch, A. Moser, A. Neuhold, J. Novak, S. G.J. Mathijssen, F. Gholamrezaie, S. A. Ponomarenko, G. Hlawacek, Qu. Shen, Ch. Teichert, P. Puschnig, C. Ambrosch-Draxl, R. Resel, and D. M. de Leeuw, *in preparation*

* **Epitaxially grown films of standing and lying pentacene molecules on Cu(110) surfaces**, T. Djuric, Th. Ules, H.-G. Flesch, H. Plank, Qu. Shen, Ch. Teichert, R. Resel, and M. G. Ramsey, *submitted*

* **Organic Heterostructure Photodiodes - Structure and Morphology of the Multilayer Device**, A. Neuhold, S. Fladischer, S. Mitsche, H.-G. Flesch, A. Moser, J. Novak, D.-M. Smilgies, E. Kraker, A. Haase, W. Grogger, and R. Resel, *submitted*

* **Ordered Semiconducting Self-Assembled Monolayers on Polymeric Surfaces Utilized in Organic Integrated Circuits**, F. Gholamrezaie, S.G.J. Mathijssen, E.C.P. Smits, T.C.T. Geuns, P.A. van Hal, S.A. Ponomarenko, H.-G. Flesch, R. Resel, E. Cantatore, P.W.M. Blom, and D.M. de Leeuw, Nano Letters 6, 1998-2002 (2010)

* **Photoreactive molecular layers containing aryl ester units: Prepa-**

ration, UV patterning and post-exposure modification, T. Höfler, A. M. Track, P. Pacher, Q. Shen, H.-G. Flesch, G. Hlawacek, G. Koller, M. G. Ramsey, R. Schennach, R. Resel, C. Teichert, W. Kern, G. Trimmel, and T. Griesser, Materials Chemistry and Physics 119, 287-293 (2010)

* **Charge transport properties and microstructure of polythiophene / polyfluorene blends**, H.-G. Flesch, R. Resel, and Ch. R. McNeill, Organic Electronics 10, 1549-1555 (2009)

* **A combined X-ray, ellipsometry and atomic force microscopy study on thin parylene-C films**, H.-G. Flesch, O. Werzer, M. Weis, J. Jakabovič, J. Kováč, D. Haško, G. Jakopič, H. J. Wondergem, and R. Resel, Physica Status Solidi (a) 206, 1727-1730 (2009)

* **X-ray studies of sub-mono-layer organic thin films**, O. Werzer, B. Stadlober, A. Haase, H.-G. Flesch, and R. Resel, Europhysics news 40, 16 (2009)

* **Evaluation of organic sub-monolayers by X-ray based measurements under gracing incident conditions**, O. Werzer, B. Stadlober, A. Haase, H.-G. Flesch, and R. Resel, The European Physical Journal Applied Physics 46, 5 pages (2009)

* **Structural Properties of Rubrene Thin Films Grown on Mica Surfaces**, T. Djuric, H.-G. Flesch, M. Koini, S. Abd Al-Baqi, H. Sitter, and R. Resel, Interface Controlled Organic Thin Films, Springer Proceedings in Physics 129, 49-53 (2009)

* **Temperature induced structural evolution of a fluorene-thiophene copolymer on rubbed surfaces**, O. Werzer, H.-G. Flesch, D. Smilgies, and R. Resel, Journal of Polymer Science Part B: Polymer Physics 47, 1599-1604 (2009)

* **Crystal structure determination from two-dimensional powders: A combined experimental and theoretical approach**, A. Moser, O. Werzer, H.-G. Flesch, M. Koini, D. Smilgies, D. Nabok, P. Puschnig, C. Ambrosch-Draxl, M. Schiek, H. Rubahn, and R. Resel, The European Physical Journal - Special Topics 167, 59-65 (2009)

* **GW-Calculations of the Self-Energy of Electrons: Numerical Investigations on Simple and Transition Metals**, H.-G. Flesch, Verlag Dr. Müller (2008)

C.2. Talks

* **Microstructure and phase behavior of a quinquethiophene based self-assembled monolayer**, Solid State Seminar, Graz, Austria, 2010

* **Crystallographic Structure and Morphology of Quinquethiophene Based Self Assembled Monolayers**, WINTERSCHOOL ON ORGANIC ELECTRONICS Fundamental Properties of Devices - Sensors, Transistors, and Solar Cells, Planneralm, Austria, 2010

* **Quinquethiophene based self assembled monolayers - a structural and morphological study**, European Conference on Molecular Electronics (ECME), Copenhagen, Denmark, 2009

* **In-Plane Structure, Temperature Annealing and Thermal Stability of Quinquethiophene SAMs**, SAMFET Meeting, Eindhoven, The Netherlands, 2009

* **Structural Changes and Charge Transport Properties of Annealed P3HT/F8TBT solar cells**, GISAS Conference, Hamburg, Germany, 2009

* **Structure and morphology of quinquethiophene based self assembled monolayers**, Materials Day 2009, Graz, Austria, 2009

* **X-ray Reflectivity and Ellipsometry - a Combined Approach for Polymer Thin Film Characterization**, 7th Autumn School on X-ray scattering from surfaces and thin layers, Smolenice, Slovakia, 2007

* **X-ray Reflectivity, Atomic Force Microscopy and Ellipsometry - a Combined Approach for Polymer Thin Film Characterization**, Solid State Seminar, Graz, Austria, 2007

* **GW-Näherung. Motivation, Anwendungen, Erfolg und Grenzen, Seminar on Theoretical Physics**, Graz, Austria, 2006

Bibliography

[1] Frank Schreiber. Structure and growth of self-assembling monolayers. *Progress in Surface Science*, 65(5-8):151–257, November 2000.

[2] Abraham Ulman. Formation and structure of Self-Assembled monolayers. *Chemical Reviews*, 96(4):1533–1554, January 1996.

[3] Nolan Tillman, Abraham Ulman, and Thomas L. Penner. Formation of multilayers by self-assembly. *Langmuir*, 5(1):101–111, January 1989.

[4] G. E. Poirier. Coverage-Dependent phases and phase stability of decanethiol on au(111). *Langmuir*, 15(4):1167–1175, February 1999.

[5] F. Schreiber, A. Eberhardt, T. Y. B. Leung, P. Schwartz, S. M. Wetterer, D. J. Lavrich, L. Berman, P. Fenter, P. Eisenberger, and G. Scoles. Adsorption mechanisms, structures, and growth regimes of an archetypal self-assembling system: Decanethiol on au(111). *Physical Review B*, 57(19):12476, May 1998.

[6] Ralph G. Nuzzo and David L. Allara. Adsorption of bifunctional organic disulfides on gold surfaces. *Journal of the American Chemical Society*, 105(13):4481–4483, June 1983.

[7] Ronald Powell, Maurice H. Francombe, and Abraham Ulman. *Self-Assembled Monolayers of Thiols, Volume 24*. Academic Press, April 1998.

[8] Jacob Sagiv. Organized monolayers by adsorption. 1. formation and structure of oleophobic mixed monolayers on solid surfaces. *Journal of the American Chemical Society*, 102(1):92–98, January 1980.

[9] X. Q. Zhang, W. Y. Yang, X. Z. You, and Y. Wei. Preparation and characterization of self-assembly organic multilayer films on silica surface. *Applied Surface Science*, 84(3):267–271, March 1995.

[10] Steffen Onclin, Bart Jan Ravoo, and David N. Reinhoudt. Engineering silicon oxide surfaces using Self-Assembled monolayers. *Angewandte Chemie International Edition*, 44(39):6282–6304, 2005.

[11] Colin D. Bain, Hans A. Biebuyck, and George M. Whitesides. Comparison of self-assembled monolayers on gold: coadsorption of thiols and disulfides. *Langmuir*, 5(3):723–727, May 1989.

[12] Gabriele Nelles, Holger Schönherr, Manfred Jaschke, Heiko Wolf, Matthias Schaub, Jörg Kü ther, Wolfgang Tremel, Ernst Bamberg, Helmut Ringsdorf, and Hans-Jürgen Butt. Two-Dimensional structure of disulfides and thiols on gold(111). *Langmuir*, 14(4):808–815, February 1998.

[13] K. Tamada, J. Nagasawa, F. Nakanishi, K. Abe, M. Hara, W. Knoll, T. Ishida, H. Fukushima, S. Miyashita, T. Usui, T. Koini, and T. R. Lee. Structure of SAMs generated from functionalized thiols on gold. *Thin Solid Films*, 327-329:150–155, August 1998.

[14] P. Silberzan, L. Leger, D. Ausserre, and J. J. Benattar. Silanation of silica surfaces. a new method of constructing pure or mixed monolayers. *Langmuir*, 7(8):1647–1651, 1991.

[15] Fatemeh Gholamrezaie, Simon G. J. Mathijssen, Edsger C. P. Smits, Tom C. T. Geuns, Paul A. van Hal, Sergei A. Ponomarenko, Heinz-Georg Flesch, Roland Resel, Eugenio Cantatore, Paul W. M. Blom, and Dago M. de Leeuw.

Ordered semiconducting Self-Assembled monolayers on polymeric surfaces utilized in organic integrated circuits. *Nano Letters*, 10(6):1998–2002, June 2010.

[16] P. Fontaine, M. Goldmann, and F. Rondelez. Influence of headgroup Cross-Linking on chain packing in langmuir monolayers of n-Alkyltrialkoxysilanes. *Langmuir*, 15(4):1348–1352, February 1999.

[17] Edsger C. P. Smits, Simon G. J. Mathijssen, Paul A. van Hal, Sepas Setayesh, Thomas C. T. Geuns, Kees A. H. A. Mutsaers, Eugenio Cantatore, Harry J. Wondergem, Oliver Werzer, Roland Resel, Martijn Kemerink, Stephan Kirchmeyer, Aziz M. Muzafarov, Sergei A. Ponomarenko, Bert de Boer, Paul W. M. Blom, and Dago M. de Leeuw. Bottom-up organic integrated circuits. *Nature*, 455(7215):956–959, October 2008.

[18] Simon G. J. Mathijssen, Edsger C. P. Smits, Paul A. van Hal, Harry J. Wondergem, Sergei A. Ponomarenko, Armin Moser, Roland Resel, Peter A. Bobbert, Martijn Kemerink, Rene A. J. Janssen, and Dago M. de Leeuw. Monolayer coverage and channel length set the mobility in self-assembled monolayer field-effect transistors. *Nat Nano*, 4(10):674–680, October 2009.

[19] L. T. Zhuravlev. Concentration of hydroxyl groups on the surface of amorphous silicas. *Langmuir*, 3(3):316–318, May 1987.

[20] Yuliang Wang and Marya Lieberman. Growth of ultrasmooth octadecyltrichlorosilane Self-Assembled monolayers on SiO2. *Langmuir*, 19(4):1159–1167, February 2003.

[21] K. Bierbaum, M. Grunze, A. A. Baski, L. F. Chi, W. Schrepp, and H. Fuchs. Growth of Self-Assembled n-Alkyltrichlorosilane films on si(100) investigated by atomic force microscopy. *Langmuir*, 11(6):2143–2150, June 1995.

[22] Reena Banga, Jack Yarwood, Anthony M. Morgan, Brian Evans, and Jaqueline Kells. FTIR and AFM studies of the kinetics and Self-Assembly of alkyltrichlorosilanes and (Perfluoroalkyl)trichlorosilanes onto glass and silicon. *Langmuir*, 11(11):4393–4399, November 1995.

[23] Sidney R. Cohen, Ron Naaman, and Jacob Sagiv. Thermally induced disorder in organized organic monolayers on solid substrates. *The Journal of Physical Chemistry*, 90(14):3054–3056, July 1986.

[24] I. M. Tidswell, B. M. Ocko, P. S. Pershan, S. R. Wasserman, G. M. Whitesides, and J. D. Axe. X-ray specular reflection studies of silicon coated by organic monolayers (alkylsiloxanes). *Physical Review B*, 41(2):1111, January 1990.

[25] Stephen R. Wasserman, George M. Whitesides, Ian M. Tidswell, Ben M. Ocko, Peter S. Pershan, and John D. Axe. The structure of self-assembled monolayers of alkylsiloxanes on silicon: a comparison of results from ellipsometry and low-angle x-ray reflectivity. *Journal of the American Chemical Society*, 111(15):5852–5861, July 1989.

[26] Carlo Carraro, Oranna W. Yauw, Myung M. Sung, and Roya Maboudian. Observation of three growth mechanisms in Self-Assembled monolayers. *The Journal of Physical Chemistry B*, 102(23):4441–4445, June 1998.

[27] Myung M. Sung, Carlo Carraro, Oranna W. Yauw, Yunsoo Kim, and Roya Maboudian. Reversible liquid - liquid transitions in the early stages of monolayer Self-Assembly. *The Journal of Physical Chemistry B*, 104(7):1556–1559, February 2000.

[28] Stefan K. Possanner, Karin Zojer, Peter Pacher, Egbert Zojer, and Ferdinand SchÃ¼rrer. Threshold voltage shifts in organic Thin-Film transistors due to Self-Assembled monolayers at the dielectric surface. *Advanced Functional Materials*, 19(6):958–967, 2009.

[29] Georg Heimel, Ferdinand Rissner, and Egbert Zojer. Modeling the electronic properties of pi-Conjugated Self-Assembled monolayers. *Advanced Materials*, 9999(9999):NA, 2010.

[30] S. Scheinert and G. Paasch. Fabrication and analysis of polymer field-effect transistors. *physica status solidi (a)*, 201(6):1263–1301, 2004.

[31] Hwa Sung Lee, Do Hwan Kim, Jeong Ho Cho, Minkyu Hwang, Yunseok Jang, and Kilwon Cho. Effect of the phase states of Self-Assembled monolayers on pentacene growth and Thin-Film transistor characteristics. *Journal of the American Chemical Society*, 130(32):10556–10564, 2008.

[32] Fengqiu Fan, Charles Maldarelli, and Alexander Couzis. Fabrication of surfaces with nanoislands of chemical functionality by the phase separation of Self-Assembling monolayers on silicon. *Langmuir*, 19(8):3254–3265, April 2003.

[33] Alexander Y. Fadeev and Thomas J. McCarthy. Binary monolayer mixtures: Modification of nanopores in Silicon-Supported tris(trimethylsiloxy)silyl monolayers. *Langmuir*, 15(21):7238–7243, October 1999.

[34] Chi Ming Yam, Aurelie Mayeux, Alexandra Milenkovic, and Chengzhi Cai. Wettabilities of organosiloxane thin films derived from SiCl3-Terminated carbosilane dendrons on mica. *Langmuir*, 18(26):10274–10278, December 2002.

[35] S P Fodor, J L Read, M C Pirrung, L Stryer, A T Lu, and D Solas. Light-directed, spatially addressable parallel chemical synthesis. *Science (New York, N.Y.)*, 251(4995):767–773, February 1991. PMID: 1990438.

[36] Hiroyuki Sugimura, Kazuya Ushiyama, Atsushi Hozumi, and Osamu Takai. Micropatterning of alkyl- and fluoroalkylsilane Self-Assembled monolayers using vacuum ultraviolet light. *Langmuir*, 16(3):885–888, February 2000.

[37] Thomas Höfler, Anna M. Track, Peter Pacher, Quan Shen, Heinz-Georg Flesch, Gregor Hlawacek, Georg Koller, Michael G. Ramsey, Robert Schennach, Roland Resel, Christian Teichert, Wolfgang Kern, Gregor Trimmel, and Thomas Griesser. Photoreactive molecular layers containing aryl ester units: Preparation, UV patterning and post-exposure modification. *Materials Chemistry and Physics*, 119(1-2):287–293, January 2010.

[38] Arieh Aviram and Mark A. Ratner. Molecular rectifiers. *Chemical Physics Letters*, 29(2):277–283, November 1974.

[39] Franco Dinelli, Mauro Murgia, Pablo Levy, Massimiliano Cavallini, Fabio Biscarini, and Dago M. de Leeuw. Spatially correlated charge transport in organic thin film transistors. *Physical Review Letters*, 92(11):116802, March 2004.

[40] M. Mottaghi, P. Lang, F. Rodriguez, A. Rumyantseva, A. Yassar, G. Horowitz, S. Lenfant, D. Tondelier, and D. Vuillaume. Low-Operating-Voltage organic transistors made of bifunctional Self-Assembled monolayers. *Advanced Functional Materials*, 17(4):597–604, 2007.

[41] George S. Tulevski, Qian Miao, Masafumi Fukuto, Rebecca Abram, Benjamin Ocko, Ronald Pindak, Michael L. Steigerwald, Cherie R. Kagan, and Colin Nuckolls. Attaching organic semiconductors to gate oxides: In situ assembly of monolayer field effect transistors. *Journal of the American Chemical Society*, 126(46):15048–15050, November 2004.

[42] Stefan C. B. Mannsfeld, Ajay Virkar, Colin Reese, Michael F. Toney, and Zhenan Bao. Precise structure of pentacene monolayers on amorphous silicon oxide and relation to charge transport. *Advanced Materials*, 21(22):2294–2298, 2009.

[43] Geetha R Dholakia, M. Meyyappan, Antonio Facchetti, and Tobin J. Marks. Monolayer to multilayer nanostructural growth transition in N-Type olig-

othiophenes on au(111) and implications for organic Field-Effect transistor performance. *Nano Letters*, 6(11):2447–2455, November 2006.

[44] Sergei A. Ponomarenko, Elena A. Tatarinova, Aziz M. Muzafarov, Stephan Kirchmeyer, Lutz Brassat, Ahmed Mourran, Martin Moeller, Sepas Setayesh, and Dago de Leeuw. Star-Shaped oligothiophenes for Solution-Processible organic electronics: Flexible aliphatic spacers approach. *Chemistry of Materials*, 18(17):4101–4108, 2006.

[45] Sergei A. Ponomarenko, O. V. Borshchev, T. Meyer-Friedrichsen, A.P. Pleshkova, Sepas Setayesh, E.C.P. Smits, S.G.J. Mathijssen, Dago de Leeuw, Stephan Kirchmeyer, and Aziz M. Muzafarov. *Organometallics*. submitted to *Organometallics*.

[46] Mohammad Mottaghi and Gilles Horowitz. Field-induced mobility degradation in pentacene thin-film transistors. *Organic Electronics*, 7(6):528–536, December 2006.

[47] L. G. Parratt. Surface studies of solids by total reflection of X-Rays. *Physical Review*, 95(2):359, July 1954. Copyright (C) 2008 The American Physical Society; Please report any problems to prola@aps.org.

[48] L. Nevot and P. Croce. Caractérisation des surfaces par réflexion rasante de rayons x. application á l étude du polissage de quelques verres silicates. *Revue de Physique Appliquée*, 15(3):19 pages, 1980.

[49] D. E. Nowak, D. R. Blasini, A. M. Vodnick, B. Blank, M. W. Tate, A. Deyhim, D.-M. Smilgies, H. Abru na, S. M. Gruner, and S. P. Baker. Six-circle diffractometer with atmosphere- and temperature-controlled sample stage and area and line detectors for use in the g2 experimental station at CHESS. *Review of Scientific Instruments*, 77(11):113301, 2006.

[50] D. -M Smilgies, D. R Blasini, S. Hotta, and H. Yanagi. Reciprocal space mapping and single-crystal scattering rods, November 2005.

[51] Detlef-M. Smilgies, Nathalie Boudet, Bernd Struth, and Oleg Konovalov. Troika II: a versatile beamline for the study of liquid and solid interfaces. *Journal of Synchrotron Radiation*, 12(3):329–339, 2005.

[52] Jens Als-Nielsen, Didier Jacquemain, Kristian Kjaer, Franck Leveiller, Meir Lahav, and Leslie Leiserowitz. Principles and applications of grazing incidence x-ray and neutron scattering from ordered molecular monolayers at the air-water interface. *Physics Reports*, 246(5):251–313, October 1994.

[53] George Vineyard. Grazing-incidence diffraction and the distorted-wave approximation for the study of surfaces. *Physical Review B*, 26(8):4146–4159, 1982.

[54] Y. Yoneda. Anomalous surface reflection of x rays. *Physical Review*, 131(5):2010, 1963.

[55] Kristian Kjaer. Some simple ideas on x-ray reflection and grazing-incidence diffraction from thin surfactant films. *Physica B: Condensed Matter*, 198(1-3):100–109, April 1994.

[56] L P Cavalcanti, O Konovalov, and I L Torriani. Lipid model membranes for drug interaction study. *European Biophysics Journal: EBJ*, 35(5):431–438, May 2006. PMID: 16598469.

[57] V. M. Kaganer, I. R. Peterson, R. M. Kenn, M. C. Shih, M. Durbin, and P. Dutta. Tilted phases of fatty acid monolayers. *The Journal of Chemical Physics*, 102(23):9412–9422, June 1995.

[58] Vladimir M. Kaganer, Helmuth Mühwald, and Pulak Dutta. Structure and phase transitions in langmuir monolayers. *Reviews of Modern Physics*,

71(3):779, April 1999. Copyright (C) 2009 The American Physical Society; Please report any problems to prola@aps.org.

[59] Denis Fichou. *Handbook of Oligo- and Polythiophenes*. Wiley-VCH, January 1999.

[60] Shuichi Nagamatsu, Keiichi Kaneto, Reiko Azumi, Mutsuyoshi Matsumoto, Yuji Yoshida, and Kiyoshi Yase. Correlation of the number of thiophene units with structural order and carrier mobility in unsubstituted even- and Odd-Numbered α-Oligothiophene films. *The Journal of Physical Chemistry B*, 109(19):9374–9378, May 2005.

[61] Marcus Halik, Hagen Klauk, Ute Zschieschang, Gunter Schmid, Christine Dehm, Markus Schutz, Steffen Maisch, Franz Effenberger, Markus Brunnbauer, and Francesco Stellacci. Low-voltage organic transistors with an amorphous molecular gate dielectric. *Nature*, 431(7011):963–966, October 2004.

[62] G. Kresse and J. Furthmüller. Efficient iterative schemes for ab initio total-energy calculations using a plane-wave basis set. *Physical Review B*, 54(16):11169, October 1996.

[63] G. Kresse and J. Furthmüller. Efficiency of ab-initio total energy calculations for metals and semiconductors using a plane-wave basis set. *Computational Materials Science*, 6(1):15–50, July 1996.

[64] Pascal Wolfer, Christian MÃ$\frac{1}{4}$ller, Paul Smith, Mohammed A. Baklar, and Natalie Stingelin-Stutzmann. [alpha]-Quaterthiophene-polyethylene blends: Phase behaviour and electronic properties. *Synthetic Metals*, 157(21):827–833, October 2007.

[65] K. Puntambekar, J. Dong, G. Haugstad, and C. D. Frisbie. Structural and

electrostatic complexity at a Pentacene/Insulator interface. *Advanced Functional Materials*, 16(7):879–884, 2006.

[66] Jian Zhang, Jürgen P. Rabe, and Norbert Koch. Grain-Boundary evolution in a pentacene monolayer. *Advanced Materials*, 20(17):3254–3257, 2008.

[67] Hoichang Yang, Tae Joo Shin, Mang-Mang Ling, Kilwon Cho, Chang Y. Ryu, and Zhenan Bao. Conducting AFM and 2D GIXD studies on pentacene thin films. *Journal of the American Chemical Society*, 127(33):11542–11543, 2005.

[68] Ajay Virkar, Stefan Mannsfeld, Joon Hak Oh, Michael F. Toney, Yih Horng Tan, Gang yu Liu, J. Campbell Scott, Robert Miller, and Zhenan Bao. The role of OTS density on pentacene and C60 nucleation, thin film growth, and transistor performance. *Advanced Functional Materials*, 19(12):1962–1970, 2009.

[69] Peter Pacher, Alexandra Lex, Veronika Proschek, Oliver Werzer, Paul Frank, Susanne Temmel, Wolfgang Kern, Roland Resel, Adolf Winkler, Christian Slugovc, Robert Schennach, Gregor Trimmel, and Egbert Zojer. Characterizing chemically reactive thin layers: Surface reaction of [2-[4-(Chlorosulfonyl)phenyl]ethyl]trichlorosilane with ammonia. *The Journal of Physical Chemistry C*, 111(33):12407–12413, 2007.

[70] Peter Pacher, Alexandra Lex, Veronika Proschek, Harald Etschmaier, Elena Tchernychova, Meltem Sezen, Ullrich Scherf, Werner Grogger, Gregor Trimmel, Christian Slugovc, and Egbert Zojer. Chemical control of local doping in organic Thin-Film transistors: From depletion to enhancement. *Advanced Materials*, 20(16):3143–3148, 2008.

[71] Harald Etschmaier, Peter Pacher, Alexandra Lex, Gregor Trimmel, Christian Slugovc, and Egbert Zojer. Continuous tuning of the threshold voltage of

organic thin-film transistors by a chemically reactive interfacial layer. *Applied Physics A: Materials Science & Processing*, 95(1):43–48, April 2009.

[72] M. Bjorck and G. Andersson. GenX: an extensible x-ray reflectivity refinement program utilizing differential evolution. http://journals.iucr.org/j/issues/2007/06/00/aj5091/aj5091hdr.html, December 2007. GenX is a versatile program using the differential evolution algorithm for fitting X-ray and neutron reflectivity data. It utilizes the Parratt recursion formula for simulating specular reflectivity. The program is easily extensible, allowing users to incorporate their own models into the program. This can be useful for fitting data from other scattering experiments, or for any other minimization problem which has a large number of input parameters and/or contains many local minima, where the differential evolution algorithm is suitable. In addition, GenX manages to fit an arbitrary number of data sets simultaneously. The program is released under the GNU General Public License.

[73] Ricardo Ruiz, Devashish Choudhary, Bert Nickel, Tullio Toccoli, Kee-Chul Chang, Alex C. Mayer, Paulette Clancy, Jack M. Blakely, Randall L. Headrick, Salvatore Iannotta, and George G. Malliaras. Pentacene thin film growth. *Chemistry of Materials*, 16(23):4497–4508, November 2004.

[74] Heinz-Georg Flesch, Oliver Werzer, Martin Weis, Ján Jakabovič;, Jaroslav Kováč;, Daniel Haško, Georg Jakopič;, Harry J. Wondergem, and Roland Resel. A combined x-ray, ellipsometry and atomic force microscopy study on thin parylene-C films. *physica status solidi (a)*, 206(8):1727–1730, 2009.

[75] Xuesong Hu, Kwanwoo Shin, Miriam Rafailovich, Jonathan Sokolov, Richard Stein, Yee Chan, Kurt Williams Wlwu, W L Wu, and Rainer Kolb. Anomalies in the optical index of refraction of spun cast polystyrene thin films. *High Performance Polymers*, 12(4):621–629, December 2000.

[76] Tomoaki Onoue, Ichiro Nakamura, Yukio Sakabe, Takeshi Yasuda, and Tetsuo Tsutsui. Low-Operating-Voltage organic Field-Effect transistors with Poly-p-Xylylene/High-k polymer bilayer gate dielectric. *Japanese Journal of Applied Physics*, 45:L770–L772, 2006.

[77] Qingsong Yu, Joan Deffeyes, and Hirotsugu Yasuda. Engineering the surface and interface of parylene c coatings by low-temperature plasmas. *Progress in Organic Coatings*, 41(4):247–253, May 2001.

[78] Harland G. Tompkins. *A User's Guide to Ellipsometry*. Academic Press, 1st edition, October 1992.

[79] Russell R. A. Callahan, Kristin G. Pruden, Gregory B. Raupp, and Stephen P. Beaudoin. Downstream oxygen etching characteristics of polymers from the parylene family. *Journal of Vacuum Science & Technology B: Microelectronics and Nanometer Structures*, 21(4):1496–1500, July 2003.

[80] A. Khabari and F.K. Urban III. Partially ionized beam deposition of parylene. *Journal of Non-Crystalline Solids*, 351(43-45):3536–3541, November 2005.

[81] Heinz Kiessig. Interferenz von röntgenstrahlen an dünnen schichten. *Annalen der Physik*, 402(7):769–788, 1931.

[82] Ullrich Pietsch, Vaclav Holy, and Tilo Baumbach. *High-Resolution X-Ray Scattering: From Thin Films to Lateral Nanostructures*. Springer, 2nd edition, August 2004.

[83] R. M. A. Azzam. *Selected Papers on Ellipsometry*. SPIE Society of Photo-Optical Instrumentation Engi, illustrated edition edition, January 1991.

[84] Harland G. Tompkins and W. A. McGahan. *Spectroscopic Ellipsometry and Reflectometry*. Wiley, 1st edition, 1999.

[85] S. Logothetidis and G. Stergioudis. Studies of density and surface roughness of ultrathin amorphous carbon films with regards to thickness with x-ray reflectometry and spectroscopic ellipsometry. *Applied Physics Letters*, 71(17):2463, 1997.

[86] Markus Krämer, Katy Roodenko, Beatrix Pollakowski, Karsten Hinrichs, Jörg Rappich, Norbert Esser, Alex von Bohlen, and Roland Hergenröder. Combined ellipsometry and x-ray related techniques for studies of ultrathin organic nanocomposite films. *Thin Solid Films*, 518(19):5509–5514, July 2010.

[87] R. M. Azzam and N. M. Bashara. *Ellipsometry and Polarized Light*. Elsevier Science Ltd, reprint edition, May 1987.

[88] Christopher R. McNeill, Agnese Abrusci, Inchan Hwang, Matthias A. Ruderer, Peter Müller-Buschbaum, and Neil C. Greenham. Photophysics and photocurrent generation in Polythiophene/Polyfluorene copolymer blends. *Advanced Functional Materials*, 19(19):3103–3111, 2009.

[89] A.C. Morteani, A.S. Dhoot, J.-S. Kim, C. Silva, N.C. Greenham, C. Murphy, E. Moons, S. CinÃ¡, J.H. Burroughes, and R.H. Friend. Barrier-Free Electron-Hole capture in polymer blend heterojunction Light-Emitting diodes. *Advanced Materials*, 15(20):1708–1712, 2003.

[90] S. Goffri, C. Müller, N. Stingelin-Stutzmann, D.W. Breiby, C.P. Radano, J.W. Andreasen, R. Thompson, R.A.J. Janssen, M.M. Nielsen, P. Smith, and H. Sirringhaus. Multicomponent semiconducting polymer systems with low crystallization- induced percolation threshold. *Nature Materials*, 5(12):950–956, 2006.

[91] Kamal Asadi, Dago M. de Leeuw, Bert de Boer, and Paul W. M. Blom. Organic non-volatile memories from ferroelectric phase-separated blends. *Nat Mater*, 7(7):547–550, July 2008.

[92] Sjoerd C. Veenstra, Joachim Loos, and Jan M. Kroon. Nanoscale structure of solar cells based on pure conjugated polymer blends. *Progress in Photovoltaics: Research and Applications*, 15(8):727–740, 2007.

[93] P. W. M. Blom, V. D. Mihailetchi, L. J. A. Koster, and D. E. Markov. Device physics of Polymer:Fullerene bulk heterojunction solar cells. *Advanced Materials*, 19(12):1551–1566, 2007.

[94] Denis E. Markov, Emiel Amsterdam, Paul W. M. Blom, Alexander B. Sieval, and Jan C. Hummelen. Accurate measurement of the exciton diffusion length in a conjugated polymer using a heterostructure with a Side-Chain Cross-Linked fullerene layer. *The Journal of Physical Chemistry A*, 109(24):5266–5274, June 2005.

[95] Jin Young Kim, Kwanghee Lee, Nelson E. Coates, Daniel Moses, Thuc-Quyen Nguyen, Mark Dante, and Alan J. Heeger. Efficient tandem polymer solar cells fabricated by All-Solution processing. *Science*, 317(5835):222–225, July 2007.

[96] W. Ma, C. Yang, X. Gong, K. Lee, and A. J. Heeger. Thermally stable, efficient polymer solar cells with nanoscale control of the interpenetrating network morphology. *Advanced Functional Materials*, 15(10):1617–1622, 2005.

[97] V. D. Mihailetchi, H. X. Xie, B. de Boer, L. J. A. Koster, and P. W. M. Blom. Charge transport and photocurrent generation in poly(3-hexylthiophene): Methanofullerene Bulk-Heterojunction solar cells. *Advanced Functional Materials*, 16(5):699–708, 2006.

[98] S.S. Van Bavel, E. Sourty, G. De With, and J. Loos. Three-dimensional nanoscale organization of bulk heterojunction polymer solar cells. *Nano Letters*, 9(2):507–513, 2009.

[99] A. Pivrikas, N. S. Sariciftci, G. Juscaronka, and R. Österbacka. A review of charge transport and recombination in polymer/fullerene organic solar cells. *Progress in Photovoltaics: Research and Applications*, 15(8):677–696, 2007.

[100] Mao-Yuan Chiu, U-Ser Jeng, Chiu-Hun Su, Keng S. Liang, and Kung-Hwa Wei. Simultaneous use of small- and Wide-Angle x-ray techniques to analyze nanometerscale phase separation in polymer heterojunction solar cells. *Advanced Materials*, 20(13):2573–2578, 2008.

[101] Xiaoniu Yang, Joachim Loos, Sjoerd C. Veenstra, Wiljan J. H. Verhees, Martijn M. Wienk, Jan M. Kroon, Matthias A. J. Michels, and René A. J. Janssen. Nanoscale morphology of High-Performance polymer solar cells. *Nano Letters*, 5(4):579–583, April 2005.

[102] S. M. Tuladhar, D. Poplavskyy, S. A. Choulis, J. R. Durrant, D. D. C. Bradley, and J. Nelson. Ambipolar charge transport in films of methanofullerene and Poly(phenylenevinylene)/Methanofullerene blends. *Advanced Functional Materials*, 15(7):1171–1182, 2005.

[103] M. Magdalena Mandoc, Welmoed Veurman, L. Jan Anton Koster, Marc M. Koetse, Jorgen Sweelssen, Bert de Boer, and Paul W. M. Blom. Charge transport in MDMO-PPV:PCNEPV all-polymer solar cells. *Journal of Applied Physics*, 101(10):104512, 2007.

[104] Chunhong Yin, Marcel Schubert, Sebastian Bange, Burkhard Stiller, Mauro Castellani, Dieter Neher, Michael Kumke, and Hans-Heinrich HoÌˆrhold. Tuning of the Excited-State properties and photovoltaic performance in PPV-Based polymer blends. *The Journal of Physical Chemistry C*, 112(37):14607–14617, 2008.

[105] A. Babel, Y. Zhu, K.-F. Cheng, W.-C. Chen, and S. A. Jenekhe. High electron mobility and ambipolar charge transport in binary blends of donor and

acceptor conjugated polymers. *Advanced Functional Materials*, 17(14):2542–2549, 2007.

[106] Eva Bundgaard and Frederik C. Krebs. Low band gap polymers for organic photovoltaics. *Solar Energy Materials and Solar Cells*, 91(11):954–985, July 2007.

[107] Michele Sferrazza and Clara Carelli. Interfaces and fluctuations in confined polymeric liquid mixtures: from immiscible to near critical systems. *Journal of Physics: Condensed Matter*, 19(7):073102, 2007.

[108] Christopher R. McNeill, Agnese Abrusci, Jana Zaumseil, Richard Wilson, Mary J. McKiernan, Jeremy H. Burroughes, Jonathan J. M. Halls, Neil C. Greenham, and Richard H. Friend. Dual electron donor/electron acceptor character of a conjugated polymer in efficient photovoltaic diodes. *Applied Physics Letters*, 90(19):193506, 2007.

[109] Christopher R. McNeill and Gregory L. Whiting. unpublished results.

[110] Christopher R. McNeill, Jonathan J. M. Halls, Richard Wilson, Gregory L. Whiting, Stephen Berkebile, Michael G. Ramsey, Richard H. Friend, and Neil C. Greenham. Efficient Polythiophene/Polyfluorene copolymer bulk heterojunction photovoltaic devices: Device physics and annealing effects. *Advanced Functional Materials*, 18(16):2309–2321, 2008.

[111] S. A. Choulis, Y. Kim, J. Nelson, D. D. C. Bradley, M. Giles, M. Shkunov, and I. McCulloch. High ambipolar and balanced carrier mobility in regioregular poly(3-hexylthiophene). *Applied Physics Letters*, 85(17):3890, 2004.

[112] DHS1100: a new high-temperature attachment for materials science in the whole orientation space. *Journal of Applied Crystallography*, 40(1):202–202, 2007.

[113] Attila J. Mozer and Niyazi Serdar Sariciftci. Negative electric field dependence of charge carrier drift mobility in conjugated, semiconducting polymers. *Chemical Physics Letters*, 389(4-6):438–442, May 2004.

[114] S. Joshi, S. Grigorian, and U. Pietsch. X-ray structural and crystallinity studies of low and high molecular weight poly(3-hexylthiophene). *physica status solidi (a)*, 205(3):488–496, 2008.

[115] R. Joseph Kline, Michael D. McGehee, Ekaterina N. Kadnikova, Jinsong Liu, Jean M. J. Frechet, and Michael F. Toney. Dependence of regioregular poly(3-hexylthiophene) film morphology and Field-Effect mobility on molecular weight. *Macromolecules*, 38(8):3312–3319, April 2005.

[116] Hari Singh Nalwa and Nalwa. *Handbook of Organic Conductive Molecules and Polymers, Conductive Polymers: Spectroscopy and Physical Properties: 003*. John Wiley & Sons Ltd, August 1996.

[117] Cheng Yang, Francesco P. Orfino, and Steven Holdcroft. A phenomenological model for predicting thermochromism of regioregular and nonregioregular poly(3-alkylthiophenes). *Macromolecules*, 29(20):6510–6517, 1996.

[118] A. C. Mayer, Michael F. Toney, Shawn R. Scully, Jonathan Rivnay, Christoph J. Brabec, Marcus Scharber, Marcus Koppe, Martin Heeney, Iain McCulloch, and Michael D. McGehee. Bimolecular crystals of fullerenes in conjugated polymers and the implications of molecular mixing for solar cells. *Advanced Functional Materials*, 19(8):1173–1179, 2009.

[119] Youngkyoo Kim, Steffan Cook, Sachetan M. Tuladhar, Stelios A. Choulis, Jenny Nelson, James R. Durrant, Donal D. C. Bradley, Mark Giles, Iain McCulloch, Chang-Sik Ha, and Moonhor Ree. A strong regioregularity effect in self-organizing conjugated polymer films and high-efficiency polythiophene:fullerene solar cells. *Nat Mater*, 5(3):197–203, March 2006.

[120] Oliver Werzer, Kurt Matoy, Peter Strohriegl, and Roland Resel. Temperature treatment of semiconducting polymers: An x-ray reflectivity study. *Thin Solid Films*, 515(14):5601–5605, May 2007.

[121] Stijn Verlaak and Paul Heremans. Molecular microelectrostatic view on electronic states near pentacene grain boundaries. *Physical Review B*, 75(11):115127, March 2007.

[122] Jenny Clark, Jui-Fen Chang, Frank C. Spano, Richard H. Friend, and Carlos Silva. Determining exciton bandwidth and film microstructure in polythiophene films using linear absorption spectroscopy. *Applied Physics Letters*, 94(16):163306, 2009.

[123] Christopher R. McNeill, Sebastian Westenhoff, Chris Groves, Richard H. Friend, and Neil C. Greenham. Influence of nanoscale phase separation on the charge generation dynamics and photovoltaic performance of conjugated polymer blends: Balancing charge generation and separation. *The Journal of Physical Chemistry C*, 111(51):19153–19160, December 2007.

[124] V. D. Mihailetchi, L. J. A. Koster, J. C. Hummelen, and P. W. M. Blom. Photocurrent generation in Polymer-Fullerene bulk heterojunctions. *Physical Review Letters*, 93(21):216601, November 2004.

[125] Christopher R. McNeill and Neil C. Greenham. Charge transport dynamics of polymer solar cells under operating conditions: Influence of trap filling. *Applied Physics Letters*, 93(20):203310, 2008.